University of Tennessee, Knoxville

TRACE: Tennessee Research and Creative Exchange

Doctoral Dissertations

Graduate School

12-2006

# Single-Molecule Detection with Active Transport

David Allan Ball
*University of Tennessee - Knoxville*

Follow this and additional works at: https://trace.tennessee.edu/utk_graddiss

 Part of the Physics Commons

## Recommended Citation

Ball, David Allan, "Single-Molecule Detection with Active Transport. " PhD diss., University of Tennessee, 2006.
https://trace.tennessee.edu/utk_graddiss/1919

This Dissertation is brought to you for free and open access by the Graduate School at TRACE: Tennessee Research and Creative Exchange. It has been accepted for inclusion in Doctoral Dissertations by an authorized administrator of TRACE: Tennessee Research and Creative Exchange. For more information, please contact trace@utk.edu.

To the Graduate Council:

I am submitting herewith a dissertation written by David Allan Ball entitled "Single-Molecule Detection with Active Transport." I have examined the final electronic copy of this dissertation for form and content and recommend that it be accepted in partial fulfillment of the requirements for the degree of Doctor of Philosophy, with a major in Physics.

Lloyd M. Davis, Major Professor

We have read this dissertation and recommend its acceptance:

Christian G. Parigger, Horace W. Crater, James W. Lewis, Ying-Ling Chen, Basil N. Antar, Robert N. Compton

Accepted for the Council:

Carolyn R. Hodges

Vice Provost and Dean of the Graduate School

(Original signatures are on file with official student records.)

To the Graduate Council:

I am submitting herewith a dissertation written by David Allan Ball entitled "Single-Molecule Detection with Active Transport." I have examined the final electronic copy of this dissertation for form and content and recommend that it be accepted in partial fulfillment of requirements for the degree of Doctor of Philosophy, with a major in Physics.

Lloyd M. Davis
Major Professor

We have read this dissertation
and recommend its acceptance:

Christian G. Parigger

Horace W. Crater

James W. L. Lewis

Ying-Ling Chen

Basil N. Antar

Robert N. Compton

Accepted for the Council:

Anne Mayhew
Vice Chancellor and Dean of
Graduate Studies

(Original signatures on file with official student records.)

# Single-Molecule Detection with Active Transport

A Dissertation

Presented for the

Doctor of Philosophy

Degree

The University of Tennessee, Knoxville

**David Allan Ball**

**December 2006**

# Dedication

This dissertation is dedicated to

my parents

Nancy and Allan Ball

# Acknowledgements

I would like to take this opportunity to thank all those who made this dissertation possible. First, thanks to Dr. Lloyd M. Davis for his guidance and patience in the laboratory. I would also like to express my appreciation to my committee members, Dr. Christian G. Parigger, Dr. Horace W. Crater, Dr. James W. L. Lewis, Dr. Ying-Ling Chen, Dr. Robert N. Compton, and Dr. Basil N. Antar for their careful reviewing of this dissertation. Thanks to Newton Wright for his technical support. I am grateful for the help provided by Dr. GuoQing Shen in many aspects of this work. Also, I would like to thank all my family and friends for their moral support through the years. Without them, I don't think I could have continued in the demanding, yet rewarding, field of Physics. Finally, I acknowledge financial support, provision of equipment, and travel support for my research from the University of Tennessee Space Institute; the Center for Laser Applications; The University of Tennessee Chemical Physics Center; Abbott Laboratories, North Chicago, Illinois; LI-COR, Inc., Lincoln, Nebraska; Perkin Elmer, Optoelectronics Division, Vaudreuil, Canada; and the National Science Foundation.

# Abstract

A glass capillary is used near the focal region of a custom-built confocal microscope to investigate the use of active transport for single-molecule detection in solution, with both one and two-photon laser excitation. The capillary tip has a diameter of several microns and is carefully aligned nearby to the sub-micron laser beam waist, collinear to the optical axis, so that a negative pressure-difference causes molecules to be drawn into the capillary, along the laser beam axis. The flow of solution, which is characterized by fluorescence correlation spectroscopy (FCS), can increase the single-molecule detection rate for slowly diffusing proteins by over a factor of 100, while the mean rate of photons during each burst is similar to that for random diffusional transport. Also, the flow is along the longest axis of the ellipsoidally-shaped confocal volume, which results in more collected photons per molecule than that for transverse flow at the same speed. When transport is dominated by flow, FCS can no longer distinguish molecules with differing translational diffusion, and hence a fluorescence fluctuation spectroscopy method based on differences in fluorescence brightness is investigated as a means for assaying different solution components, for applications in pharmaceutical drug discovery. Multi-channel fluctuation spectroscopy techniques can also be used for assays with the flow system and hence this dissertation also reports the characterization of a prototype 4-channel single-photon detector with a two-wavelength polarization-resolved optical set-up.

# Contents

**1 Introduction ..... 1**

1.1. Signal and Background for Single-Molecule Fluorescence Detection ..... 2

1.2. Prior Single-Molecule Detection Experiments ..... 4

1.3. Application to Pharmaceutical Drug Discovery ..... 7

1.4. Objectives and Research Developments ..... 10

**2 Two-Photon Excitation ..... 12**

2.1. Advantages and Disadvantages of Two-Photon Excitation ..... 12

2.2. Dependence of Saturation on the Type of Excitation ..... 14

**3 Data Reduction Methods ..... 19**

3.1. Fluorescence Correlation Spectroscopy ..... 20

3.2. Polarization Anisotropy ..... 27

3.3. Photon Counting Histogram ..... 28

3.4. Fluorescence Intensity Distribution Analysis ..... 30

3.5. Successive Photon Intensity Distribution Analysis ..... 32

3.6. Scanning Fluorescence Fluctuation Spectroscopy ..... 32

**4 Flow System ..... 36**

4.1. Description of Flow System and Alignment Procedure ..... 36

4.2. Comparison of Techniques for Inducing Flow ..... 41

4.3. Estimate of Minimum Flow Velocity ..... 44

**5 Experimental Setup ..... 46**

5.1. Confocal Epi-Illumination ..... 46
5.2. Laser Systems ..... 50
5.3. Data Acquisition and Analysis ..... 54
**6 Prototype Four-Channel Photon Detector ..... 58**
6.1. Experimental Setup for Evaluation ..... 59
6.2. Comparison with Single Channel Detector ..... 62
6.3. Timing Shift with Increasing Count Rate ..... 66
6.4. Summary of Characteristics ..... 70
**7 Results of Single-Molecule Detection with Flow ..... 71**
7.1. Background Characterization ..... 71
7.2. One-Photon Excitation with Flow ..... 75
7.3. Two-component Fluorescence Brightness Assay with Flow ..... 78
7.4. Two-Photon Excitation ..... 87
7.4.1. TPE without Flow ..... 89
7.4.2. TPE with Flow ..... 92
7.5. Conclusions ..... 96
7.6. Suggestions for Future Work ..... 97
**References ..... 99**
**Appendices ..... 111**
**A Fluorescence and Competing Processes ..... 112**
**B Simplified Treatment of Two-Photon Excitation ..... 115**
**Vita ..... 120**

# Tables

Table 6.1: Comparison of the manufacturers specifications for the 4-channel SPAD (SPCM-AQ4C) and single channel SPAD (SPCM-AQR). ..... 67

# Figures

Figure 1.1: Raman scattering wavelength ..... 5

Figure 1.2: Pharmaceutical drug screening experiment ..... 8

Figure 2.1: Expected fluorescence behavior for different types of excitation ..... 16

Figure 2.2: Measured fluorescence behavior for different types of excitation ..... 18

Figure 3.1: Example of normalized autocorrelation function ..... 21

Figure 3.2: Three-dimensional Gaussian-ellipsoid volume ..... 22

Figure 3.3: The effect of flow on normalized autocorrelation function ..... 26

Figure 3.4: Molecular brightness calculated with S-FFS ..... 35

Figure 4.1: Photograph of flow system ..... 37

Figure 4.2: Schematic representation of the capillary used for inducing a flow in the sample ..... 39

Figure 4.3: CCD image of 10 mm capillary during alignment procedure ..... 40

Figure 5.1: Photograph of the custom-built fluorescence microscope ..... 48

Figure 5.2: Schematic diagram of the custom-built fluorescence microscope ..... 49

Figure 5.3: Available laser systems ..... 51

Figure 5.4: Photon burst graph from the LabView data collection program ..... 55

Figure 6.1: Photograph of the Perkin-Elmer SPCM-AQ4C ..... 60

Figure 6.2: Schematic diagram of the setup used for testing of the Perkin-Elmer SPCM-AQ4C ..... 61

Figure 6.3: Example data from the Perkin-Elmer SPCM-AQ4C ..... 63

Figure 6.4: Normalized ACF of water ..... 65

Figure 6.5: Fluorescence lifetime measurement for Channel 0 with increasing count rate ..... 68
Figure 6.6: Fluorescence lifetime measurement for Channel 1 with increasing count rate ..... 69
Figure 7.1: Background signal from water at various distances from the capillary ..... 73
Figure 7.2: Time-resolved count rate with water and capillary at various distances ..... 74
Figure 7.3: Characterization of the flow with FCS by use of OPE ..... 76
Figure 7.4: Plot of count rate vs. time with flow ..... 79
Figure 7.5: Effect of detergent on the ACF amplitude ..... 80
Figure 7.6: S-FFS mean burst amplitude data for OPE ..... 82
Figure 7.7: S-FFS rate of photon bursts data for OPE ..... 83
Figure 7.8: Spectra of several organic dyes ..... 85
Figure 7.9: Comparison of burst heights without flow ..... 86
Figure 7.10: S-FFS data for a titration of fluorophores with different brightness ..... 88
Figure 7.11: Results of preliminary studies of Rhodamine B by use of TPE ..... 90
Figure 7.12: Results of preliminary studies of Qdot 585-Streptavidin conjugate by use of TPE ..... 91
Figure 7.13: Time-resolved count rate with TPE ..... 93
Figure 7.14: Characterization of flow with FCS by use of TPE ..... 94
Figure 7.15: Calculated flow velocities at the distances shown in Figure 7.14 ..... 95
Figure A.1: Jablonski diagram for an organic dye molecule ..... 113
Figure B.1: Simplified level diagram illustrating TPE ..... 117

# Abbreviations

| | |
|---|---|
| ACF | autocorrelation function |
| BBO | beta barium borate ($\beta$-$BaB_2O_4$) |
| CFD | constant fraction discriminator |
| cw | continuous wave |
| DMA | direct memory access |
| FCS | fluorescence correlation spectroscopy |
| FFS | fluorescence fluctuation spectroscopy |
| FIDA | fluorescence intensity distribution analysis |
| FIFO | first in first out |
| FWHM | full-width at half-maximum |
| FRET | Förster resonance energy transfer |
| LIF | laser-induced fluorescence |
| OMA | optical mutichannel analyzer |
| OPE | one-photon excitation |
| PAID | photon arrival-time interval distribution |
| PCH | photon counting histogram |
| S-FFS | scanning fluorescence fluctuation spectroscopy |
| SLIK | super low K |
| SMD | single-molecule detection |
| SMS | single-molecule spectroscopy |
| SPAD | single-photon avalanche diode |

| | |
|---|---|
| SPIDA | successive photon interval distribution analysis |
| TCSPC | time-correlated single-photon counting |
| TDC | time to digital converter |
| TIR | total internal reflection |
| TOA | time of arrival |
| TPE | two-photon excitation |
| TTTR | time-tagged time-resolved |

# Chapter 1

# Introduction

Over the past decade, single-molecule detection (SMD) and fluorescence correlation spectroscopy (FCS) have come to play an important role in biological studies [1-4]. For example, the use of fluorescent labels for single-molecule spectroscopy (SMS) has enabled several groups to investigate molecular motors [5,6], and cell-signaling pathways [1], and could possibly allow rapid and efficient DNA sequencing [7,8]. FCS and other techniques based on fluorescence fluctuations from single molecules, known collectively as fluorescence fluctuation spectroscopy (FFS), also offer complimentary methods to measure the binding of drug-like compounds to proteins for use in pharmaceutical drug discovery [9].

Procedures, or assays, for pharmaceutical drug discovery based on SMD techniques have advantages over bulk measurements, as SMD allows the study of molecular properties that may not be apparent in inhomogeneous distributions of an ensemble. The increased information content obtained from investigations of individual molecules compared to bulk measurements reduces the number of independent measurements that are required.

This dissertation reports on a novel geometry for a capillary flow system, and the use of a new FFS technique based on fluorescence brightness. A brief history of SMD in solution, as well as the objective and motivation for the current work is given in Chapter 1. Chapter 2 explains the advantages and shortcomings of SMD by use of two-photon excitation (TPE), which was first demonstrated by Webb, *et al*. [10], and also discusses saturation behavior for different forms of excitation. Chapter 3 describes several data reduction methods used in FCS and SMD. The apparatus developed in this research for the implementation of flow within a microliter sample in a confocal microscope is presented in Chapter 4. Chapter 5 describes the optical system, lasers, and detection electronics that were configured for SMD experiments. In Chapter 6, the characterization of a prototype four-channel single-photon detector for multichannel SMS and FCS is described. Representative SMD and FCS experimental results, obtained with an applied flow, and suggestions for future work, are presented in Chapter 7.

## 1.1. Signal and Background for Single-Molecule Fluorescence Detection

The most common method used for the study of single molecules in solution is laser-induced fluorescence (LIF). In this technique, laser light is used to repeatedly excite an organic dye molecule from its ground state to an excited singlet state and therein to cause the emission of a burst of fluorescence. The possible photophysical processes that may occur during molecular fluorescence are discussed in detail in Ref. [11] and are briefly reviewed in Appendix A.

In order to detect single molecules with high efficiency, it is necessary to eliminate as much of the background as possible. The sources of this background include detector dark noise, autofluorescence of optical components and objects close to the laser focus, and scattered laser light. Dark noise is an intrinsic feature of the specific detector, and is the result of thermal electrons, rather than light. Typical dark count rates for the detectors discussed here are of the order of 25 to 500 $s^{-1}$. Substrate autofluorescence can be reduced by use of longer excitation and emission wavelengths, or by use of fused silica in place of glass. Scattered light is mostly specular scattering from components nearby to the focus and Rayleigh scattering from solvent molecules. Typical cross-sections for Rayleigh scattering are on the order of $10^{-27}$ $cm^2$ for each solvent molecule. In either case, the scattered light is at the same wavelength as the incident radiation. However, dye-molecule fluorescence is red-shifted with respect to the excitation wavelength, and hence Rayleigh and specular scattering can be almost completely eliminated by the use of a spectral filter in the optical collection path. However, the laser beam often contains incoherent light at other wavelengths, which can elastically scatter and pass through the spectral filter. In order to reduce this source of background, the laser beam is passed through a narrow-band spectral filter before it enters the microscope.

Once elastically scattered light is effectively blocked, the major source of background is Raman scattering from solvent molecules. The Raman scattering cross-section for a typical solvent molecule is on the order of $10^{-29}$ $cm^2$ and there are approximately $3 \times 10^7$ water molecules in a one femtoliter probe volume. Raman scattering is an inelastic process, which results in scattered light at frequencies $\nu' = \nu_0 \pm \nu_M$, where $\nu_0$ is the frequency of the incident radiation. The frequency shifts, $\nu_M$,

are due to vibrational and rotational transitions. The major Raman transitions for water result from the O-H stretch ($\lambda_v^{-1}$ = 3430 cm$^{-1}$), and bend modes ($\lambda_v^{-1}$ = 1640 cm$^{-1}$) [12]. The dependence of the scattered light wavelength, $\lambda_s$ on the excitation wavelength, $\lambda_e$ is given by $\lambda_s = (\lambda_e^{-1} - \lambda_v^{-1})^{-1}$, and for convenience is shown in Figure 1.1. Not that because the Stokes shifted bands for water typically overlap the fluorescence band of the dye molecule, a spectral filter cannot be used to remove this source of background without compromising the fluorescence signal. However, Raman scattering occurs effectively instantaneously, whereas fluorescence photons are delayed with respect to an excitation pulse by a time with a mean equal to the fluorescence lifetime, and so time-gated photon detection can be used to reduce this form of background.

## 1.2. Prior Single-Molecule Detection Experiments

Hirschfeld first accomplished the detection of single molecules by laser-induced fluorescence (LIF) in 1976 [13]. In these early experiments, however, the target was an immobilized polyethyleneimine molecule labeled with between 80 and 100 molecules of fluoresceine dye. The number of fluorophores necessary for detection was reduced by increase of the light detection efficiency in a flow-cytometer configuration, in which a hydrodynamically-focused sample stream forces molecules to pass through the focused laser beam [14,15]. The detection limit was reduced to the single-molecule level by use of time-gating to eliminate Raman scatter [16]. These early studies used low quantum efficiency (~0.15) photo-multiplier tubes (PMT), and the introduction of single-photon avalanche diodes (SPAD) [17,18], which have a quantum efficiency of ~0.65, allowed

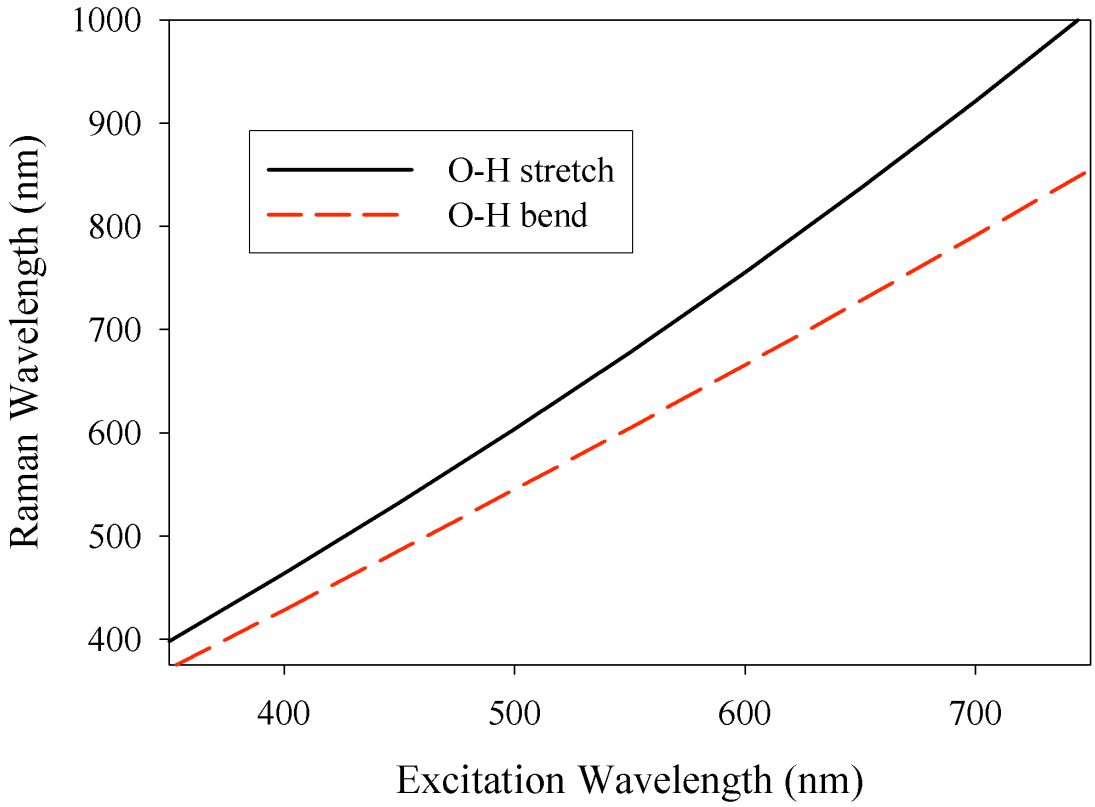


Figure 1.1: Raman scattering wavelength. The dependence of Raman wavelength on excitation wavelength for water.

the first high efficiency SMD experiments with flow [19,20], and has since resulted in commercial systems for routine SMD and FCS studies. More recently, groups have turned to the applications of SMD, mostly for biological investigations. These experiments include the study of molecular motors [5,6], and pharmaceutical drug discovery [9].

SMD with flow in a microfluidic lab-on-a-chip device with the use of electrophoretic separation of different molecule types was first achieved in 1998 [21]. Identification of different fluorescent species in a flowing sample by comparison of fluorescence lifetimes was also demonstrated with the use of flow within a micron-sized capillary [22,23]. SMD with flow has been extended for use in the counting and identification of labeled DNA molecules [24-26] and amino acids [27], the binding of quantum dots to organic dyes [28], and the use of two-photon excitation [29,30]. There has also been work done to improve the techniques of flow-cell fabrication [31-37], the instrumentation used for SMD with flow [23], and flow characterization by use of both FCS [38] and photo-activated fluorophores [39]. For a more comprehensive summary of the application of SMD for a flowing sample, the reader is directed to two review articles [40,41].

Today, there are several commercially available fluorescence microscopes that can be used for the detection of single molecules. This was not the case even just a few years ago, and so a custom apparatus, which provides greater flexibility, was built for this purpose [42]. The custom-built microscope is a versatile system, and has been used for imaging experiments by utilization of total-internal reflection (TIR) excitation [43,44], as well as several investigations that use FCS [45-50], and was used for the work described

herein. During the course of this dissertation research, two major rebuilds of the microscope were performed. The first rebuild was to relocate the experiment to a larger optical table that held several laser systems, including an Argon ion laser and femtosecond Ti-Sapphire laser for two-photon excitation. The experiments reported in Chapter 7 were performed with this instrument. Some other preliminary experiments were performed with a capillary flow device retrofitted to a Zeiss Confocor 2 microscope during a 2-day visit to Abbott Laboratories. The UTSI microscope was recently rebuilt again to incorporate a clean hood (for future research with nanofluidic devices) and optics for multi-wavelength excitation and emission.

## 1.3. Application to Pharmaceutical Drug Discovery

SMD and FFS techniques have become important in the industry of pharmaceutical drug discovery. A high-throughput screening campaign will screen up to one million library compounds in homogeneous solution to determine which will bind to a particular target protein. The measurements are multiplexed in that each sample contains the target and multiple compounds (typically ~10), with each compound present in at least two samples, so that correlated "hits" can identify the potent compound. These measurements rely on the ability to determine the binding of the possible drug-like compounds to the target, and typical results are shown in Figure 1.2a. High-throughput screening is an inexact science. Systematic errors due to aggregation, surface adsorption, photobleaching, interactions between library compounds, and unwanted fluorescence of reagents can cause the

(a)

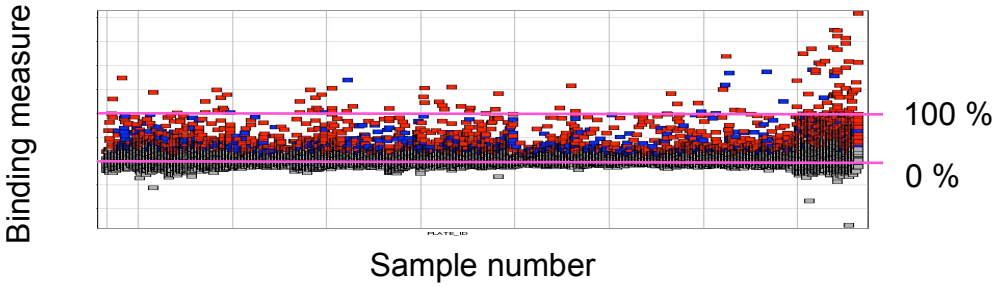


(b)

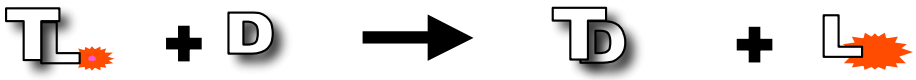


Figure 1.2: Pharmaceutical drug screening experiment. (a) Example data, and (b) Competitive binding assay: Drug compound, D, displaces the fluorescently-labeled ligand, L, from the target bio-molecule, T, and may thereby cause a change in the fluorescent properties. Taken from Ref. [48].

binding measure to be less than 0% or greater than 100%, but consistent "hits" will guide chemists in the development of improved compounds [48]. In order to determine the binding of a possible drug-like compound to the target bio-molecule, a competitive binding assay is typically used, in which a fluorescently labeled ligand binds to the unlabeled target, but is displaced with the binding of the drug, as depicted in Figure 1.2b. The translational and rotational diffusion of the fluorescently-labeled ligand will change when it becomes displaced. Also, the fluorescence may be quenched due to energy transfer from the fluorophore to the target, but when an effective drug displaces the ligand, as shown in Figure 1.2b, the fluorescence brightness may increases. The fraction of free and bound ligands can be determined by several fluorescence techniques, which can either be performed on a bulk sample or at the single-molecule level.

A single bulk-fluorescence-measurement can determine the abundance of one sample component, but for a multi-component sample, an additional independent measurement must be performed to quantify each additional species. For example, a solution that contains three species would require three independent measurements to yield enough information to calculate the concentration of each species. Multi-channel spectroscopy methods, such as time or spectrally resolved fluorescence detection, can yield sufficient information for multi-component assays. FFS methods, which essentially measure the time sequence of fluorescence from individual molecules, can also be used to perform multi-component assays, but only one detection channel is necessary, because the temporal behavior of the fluorescence is recorded. FFS methods that use multiple

detection channels can capture even greater information content for multi-component assays.

The most commonly used technique for drug-binding measurements is fluorescence polarization anisotropy of an ensemble of molecules, while techniques based on FFS include FCS, fluorescence intensity distribution analysis (FIDA), and the photon counting histogram (PCH). These techniques, along with several others, will be discussed further in Chapter 3.

## 1.4. Objectives and Research Developments

The broad goal of this work is to research methods for increasing the throughput of single-molecule based drug-binding assays, by the use of a flowing sample. The research has required the development and characterization of a capillary flow system that can be retrofitted to a confocal microscope for SMD, with both one-photon excitation (OPE), and TPE. One version of this capillary flow system was installed on a Zeiss Confocor 2 microscope and FCS system at Abbott Laboratories, Chicago, and another was used with the custom-built microscope in our lab in Tullahoma. Although FCS can be used to characterize the flow system, it can no longer be used to distinguish free and protein-bound molecules with differing translational diffusion when transport is dominated by the applied flow. Therefore it was necessary to investigate other methods for assaying the free and protein-bound fluorescent sample components, such as multi-channel fluctuation spectroscopy methods, which allow measurements at several wavelengths to be performed simultaneously.

The initially built apparatus was to use two polarization channels, which would allow the fluorescence polarization anisotropy to be measured, and hence the rotational diffusion, which is unaffected by the application of flow, would be used to determine the abundance of the bound and free sample constituents. This scheme with two detectors had been successively used in previous work without flow [42]. Unfortunately, during the development of the flow system, one of the two detectors failed and it was not possible to repair it.

At that time, a prototype four-channel detector (SPCM-AQ4C) was provided on loan for evaluation by Perkin-Elmer (Vaudreuil, Canada Optoelectronics division). As described in Chapter 6, this was set up with two polarization channels, as well as two wavelength channels. However, the background, afterpulsing, and timing performance of the prototype four-channel detector was found to be poor compared to the single channel detector, and due to this inferior performance and limited funds, it was not purchased. Therefore, only a single working detector was available for the research.

The use of only one detector limits the methods that can be used for drug-binding assays with flow. An FFS method based on differences in fluorescence brightness was investigated, as the single-particle brightness can be affected by binding. Results are presented in Chapter 7. Fluorescence quenching can cause the change in brightness, as shown schematically in Figure 1.2b. Other assays can be performed in which the drug-like compound and the target are both fluorescently labeled, which causes the brightness to double when the two are bound.

# Chapter 2

# Two-Photon Excitation

In the previous chapter, laser-induced fluorescence was discussed in which a single photon had the proper energy to excite a molecule. Here, the case where the photons have only half of the energy required for excitation is described.

TPE was first predicted in the 1930's by Maria Göppert-Mayer [51], but it wasn't until the 1960's, with the aid of a laser, that TPE was actually observed in $Eu^{2+}$ in $CaF_2$ crystals by Kaiser and Garrett [52]. Recently, TPE has been used for fluorescence imaging [53-55], FCS [56], and SMD with an applied flow [29,30], because of some advantages that it has over the more conventional one-photon excitation [57]. The principles of TPE and advantages and disadvantages are discussed in Section 2.1. The dependence of fluorescence saturation on the type of excitation contributes to a disadvantage of TPE and is described in Section 2.2.

## 2.1. Advantages and Disadvantages of Two-Photon Excitation

TPE requires that a molecule absorb two photons simultaneously (within $\sim 10^{-16}$ s). The rate at which this occurs naturally is extremely low. For example in bright sunlight a molecule that is a good two-photon absorber would be excited by a two-photon

interaction once every 10 million years, compared to about once a second for a good one-photon absorber excited by a single photon [55]. This is the reason why it took thirty years and the development of the laser between the prediction and observation of this phenomenon. As discussed in Appendix B, if saturation effects are negligible, fluorescence from TPE is proportional to the square of the laser irradiance. This fact leads to several advantages over OPE, especially for *in vivo* studies. However, there are disadvantages as well, mainly due to the lower signal available for SMD.

The dependence of TPE on the square of the laser intensity causes the volume where excitation occurs to be confined to the focal region, whereas excitation occurs along the entire beam path volume with OPE. This results in reduced photodamage to the sample, which is especially important for living cells in order to avoid damage to vital cell components, and it also reduces the amount of heating caused by the laser that could kill the cell. The small excitation volume also leads to an inherent optical sectioning, which reduces background caused by out-of-focus fluorescence, and eliminates the need for a pinhole in the confocal fluorescence microscope. This inherent optical sectioning is especially advantageous when a capillary is positioned near the laser focus, because only fluorophores at the focus are excited, while fluorophores that are adsorbed on the capillary or autofluorescence from the capillary will not be excited.

Other benefits arise with TPE from the use of infrared wavelengths. The use of infrared excitation causes elastic Rayleigh and inelastic Raman scattering from solvent molecules, each of which is proportional to $\sim\lambda^{-4}$, to be greatly reduced. Furthermore, the scattered light can be almost completely spectrally filtered from the detector, because it is far from the fluorescence emission band. The longer wavelengths are also advantageous

for *in vivo* studies because biological matter typically exhibits much lower one-photon absorption in this regime, which allows deeper laser penetration.

Although the background is reduced with TPE, the fluorescence signal is also greatly reduced, due in part to the different saturation behavior for TPE, as described below in Section 2.2. This leads to a lower signal for SMD, which inhibits FFS assays based on fluorescence brightness that will be described in Chapter 3.

## 2.2. Dependence of Saturation on the Type of Excitation

One major disadvantage of TPE is that for pulsed excitation, the maximum fluorescence count rate, which occurs at saturation, is less than that obtained with cw OPE. Rate equation models have been used to derive the dependence of the fluorescence count rate, $F$, on laser irradiance for cw, sub-nanosecond pulses, and sub-picosecond pulses. As shown in [29], the fluorescence count rate may be expressed as a Taylor expansion

$$F = \sum_{n=1}^{\infty} \alpha_n \left( \langle I \rangle / I_S \right)^n, \tag{2.1}$$

where $\langle I \rangle$ is the average laser irradiance, and

$$I_S = E_\gamma / \left( \sigma_a \tau_F (1 + Q) \right) \tag{2.2}$$

is the saturation irradiance, where $E_\gamma = hc / \lambda_0$ is the laser photon energy, in which $h$ is Planck's constant, $c$ is the speed of light and $\lambda_0$ is the vacuum wavelength of the laser. Here, $\sigma_a$ is the absorption cross section, $\tau_F$ is the fluorescence lifetime, and

$$Q = R \frac{\tau_P}{\tau_F}, \qquad \text{for cw excitation, or} \tag{2.3}$$

$$Q \approx R\frac{\tau_P}{T}, \qquad \text{for pulsed excitation with } \tau_F << T << \tau_P, \tag{2.4}$$

where $R$ is the triplet crossing yield, $\tau_P$ is the phosphorescence lifetime and $T$ is the time between laser pulses. The $\alpha_n$'s in Eqn. 2.1 are given by

$$\alpha_n = \frac{-k_{decay}(-1)^n}{1+Q}, \qquad \text{for cw excitation with } \langle I \rangle < I_S, \tag{2.5}$$

$$\alpha_n = -k_{decay}\left(\frac{\tau_F}{T}\right)\frac{(-1)^n}{n!}, \qquad \text{for sub-ns excitation with } Q = 0, \tag{2.6}$$

$$\alpha_n = -k_{decay}\left(\frac{\tau_F}{2T}\right)\frac{(-2)^n}{n!}, \qquad \text{for sub-picosecond excitation with } Q = 0. \tag{2.7}$$

Here, $k_{decay}$ is the decay rate from the excited state to the ground state, and $\tau_F$ is the fluorescence lifetime.

Figure 2.1 illustrates the difference between the three types of laser excitation. As TPE requires the use of femtosecond pulses, Eqn. 2.7 is used, but with $\langle I \rangle$ replaced by $\langle I^2 \rangle = \int_0^T I^2(t)\mathrm{d}t/T$, and $I_S$ replaced by

$$I_S' = \frac{E_\gamma^2}{\sigma_{TPE}T}, \tag{2.8}$$

where $\sigma_{TPE}$ is the two-photon absorption cross-section, which has dimensions of $\mathrm{cm}^4\mathrm{s}$. Figure 2.1 and Eqn 2.1 predict that the fluorescence rate as saturation is approached is greatest for cw excitation, less for one-photon pulsed excitation (because a molecule must wait for the next laser pulse before re-excitation), and less still for femtosecond pulsed excitation, as used with TPE (because the molecule excited state manifold does not have time to thermalize during the laser pulse, so stimulated emission plays a role in the saturation behavior).

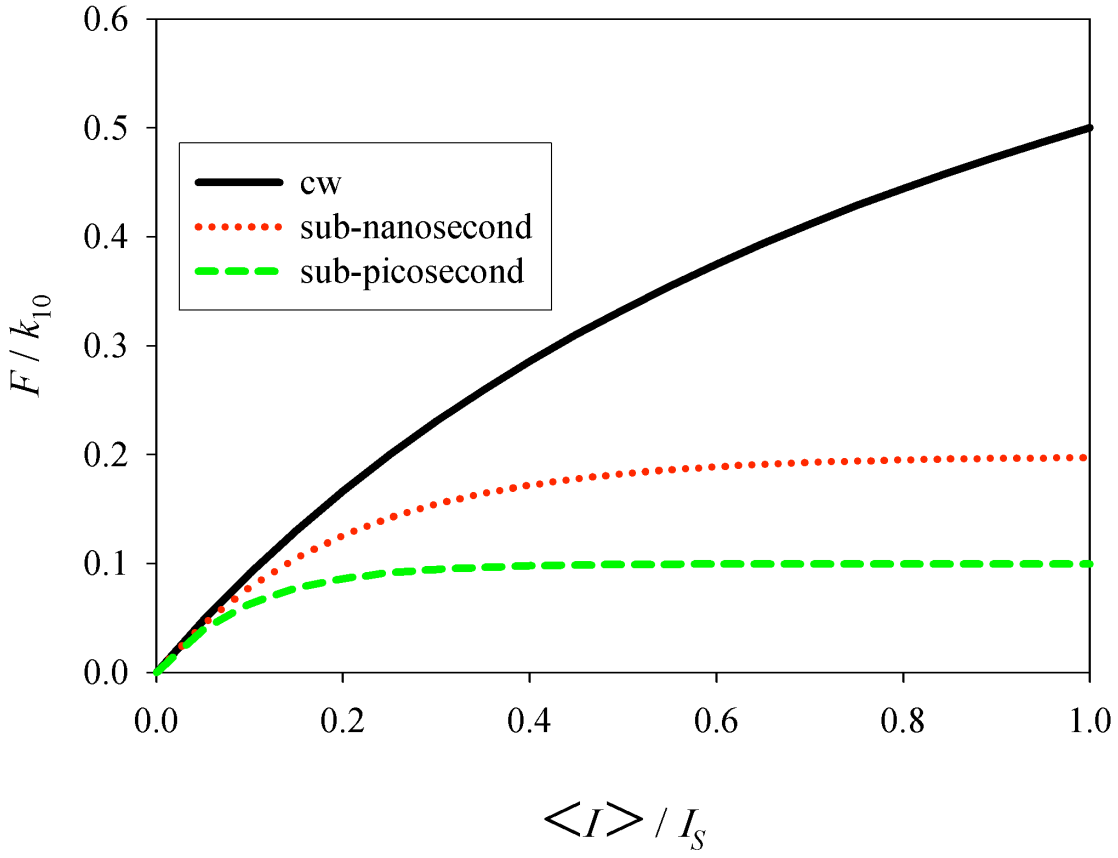


Figure 2.1: Expected fluorescence behavior for different types of excitation. Values of $F / k_{10}$ are calculated by use of Eqns. 2.1, 2.5 (black, top), 2.6 (red, middle), and 2.7 (green, bottom), with $Q = 0$.

To check the dependence of the saturation behavior on the type of excitation experimentally, the fluorescence count rate was measured with increasing laser power for 1.14 nM samples of Rhodamine B, by the use of OPE with both cw, and sub-nanosecond pulsed excitation, the results of which are shown in Figure 2.2. The laser power in Figure 2.2 is normalized by the absorptivity at each wavelength, because the wavelengths used were 514 nm for cw excitation, and 532 nm for the 76 MHz/ 70 ps pulsed excitation.

Although it proved possible to obtain FCS and SMD data with the use of TPE, the photon bursts from single molecules excited by TPE were smaller than those obtained with OPE, possibly because of the saturation behavior discussed above. A doubling of the repetition rate of the laser, as was done in Ref. [10], could possibly improve the photon burst size.

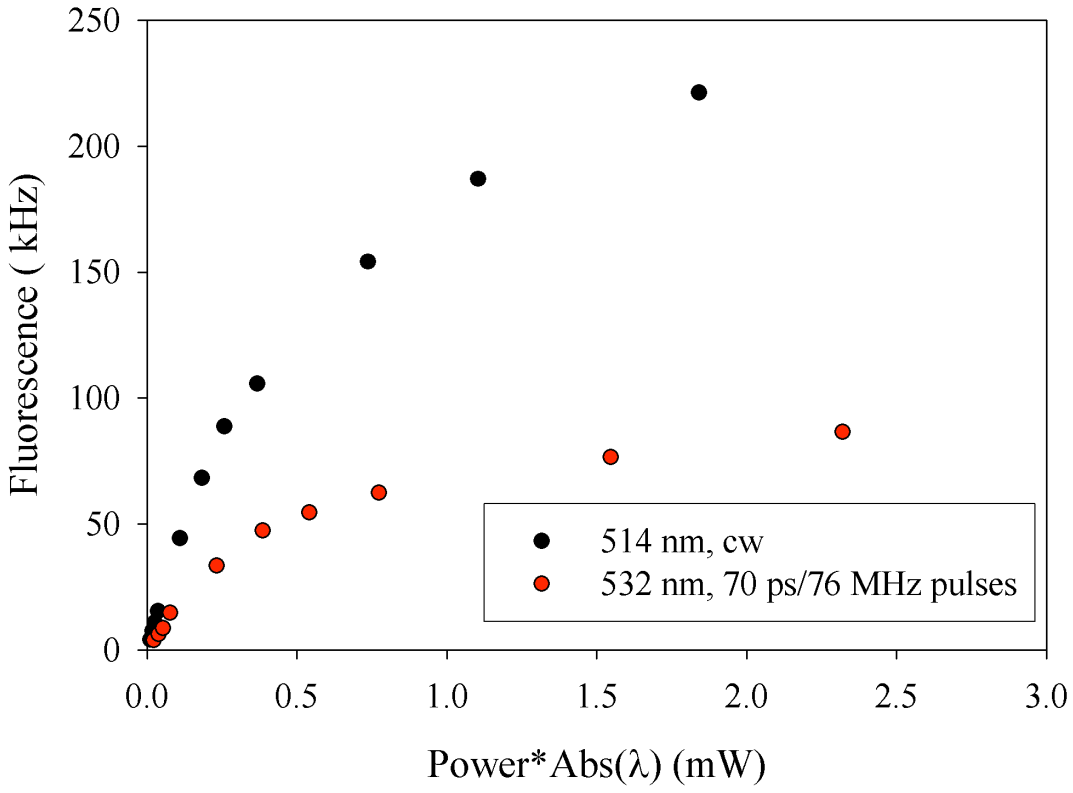


Figure 2.2: Measured fluorescence behavior for different types of excitation. The count rate was obtained with Rhodamine B at a concentration of 1.14 nM with both cw ($\lambda$ = 514 nm), and pulsed excitation ($\lambda$ = 532 nm).

# Chapter 3

# Data Reduction Methods

In this Chapter several methods will be described that allow the data obtained in SMD and FFS experiments to be interpreted. All of these techniques have the ability to determine the fraction of free and bound fluorophores, by analysis of the diffusional motion, either translation or rotation, or fluorescence brightness of the chromophore. For applications in pharmaceutical drug discovery, no single method is considered superior to the others, but rather they are all viewed as complementary, as they are advantageous under different conditions and can often be implemented simultaneously for improved global analysis.

In Sections 3.1 and 3.2, analysis techniques that concentrate on diffusional motion will be discussed, namely FCS, which can extract translational diffusion constants, and fluorescence polarization anisotropy, which can assay species with different rotational diffusion constants. The remaining sections will describe methods that use fluorescence brightness as a means for distinguishing different molecular species; these include the photon counting histogram (Section 3.3), fluorescence intensity distribution analysis (Section 3.4), successive photon interval distribution analysis (Section 3.5), and scanning fluorescence fluctuation spectroscopy (Section 3.6).

## 3.1. Fluorescence Correlation Spectroscopy

FCS has become an increasingly popular method to distinguish solution components with different masses. FCS accomplishes this by use of the normalized autocorrelation function (ACF) of the stream of fluorescence photons. The ACF is then fit to extract parameters such as the molecular concentration and mean diffusional residence time, $\tau_D$. An example of a normalized ACF is shown in Figure 3.1.

The major assumption made for FCS is that the shape of the probe volume formed by the focused laser and the collection efficiency profile of the confocal pinhole is well approximated by a three-dimensional Gaussian ellipsoid. The mean fluorescence count rate from a molecule located at $x$, $y$, $z$ is then given by

$$R(x,y,z) = R_0 \exp\left[-\frac{2(x^2+y^2)}{\omega_0^2} - \frac{2z^2}{z_0^2}\right], \tag{3.1}$$

where $R_0$ is the mean fluorescence count rate for a molecule located at the origin, and $\omega_0$, and $z_0$ are the $1 / e^2$ radii in the $x$-$y$ plane, and the $z$-direction, respectively. A sketch of the confocal probe volume is shown in Figure 3.2.

For a fluctuating fluorescence signal, $F(t)$, the normalized ACF, $G(\tau)$, is given by

$$G(\tau) = \frac{\langle F(t)F(t+\tau)\rangle}{\langle F(t)\rangle\langle F(t+\tau\rangle}, \tag{3.2}$$

where the angular brackets indicate an average over all times, such that

$$\langle F(t)\rangle = \lim_{T\to\infty}\frac{1}{2T}\int_{-T}^{T} F(t')dt'. \tag{3.3}$$

For a multi-species sample with diffusion as the dominant mode of transport

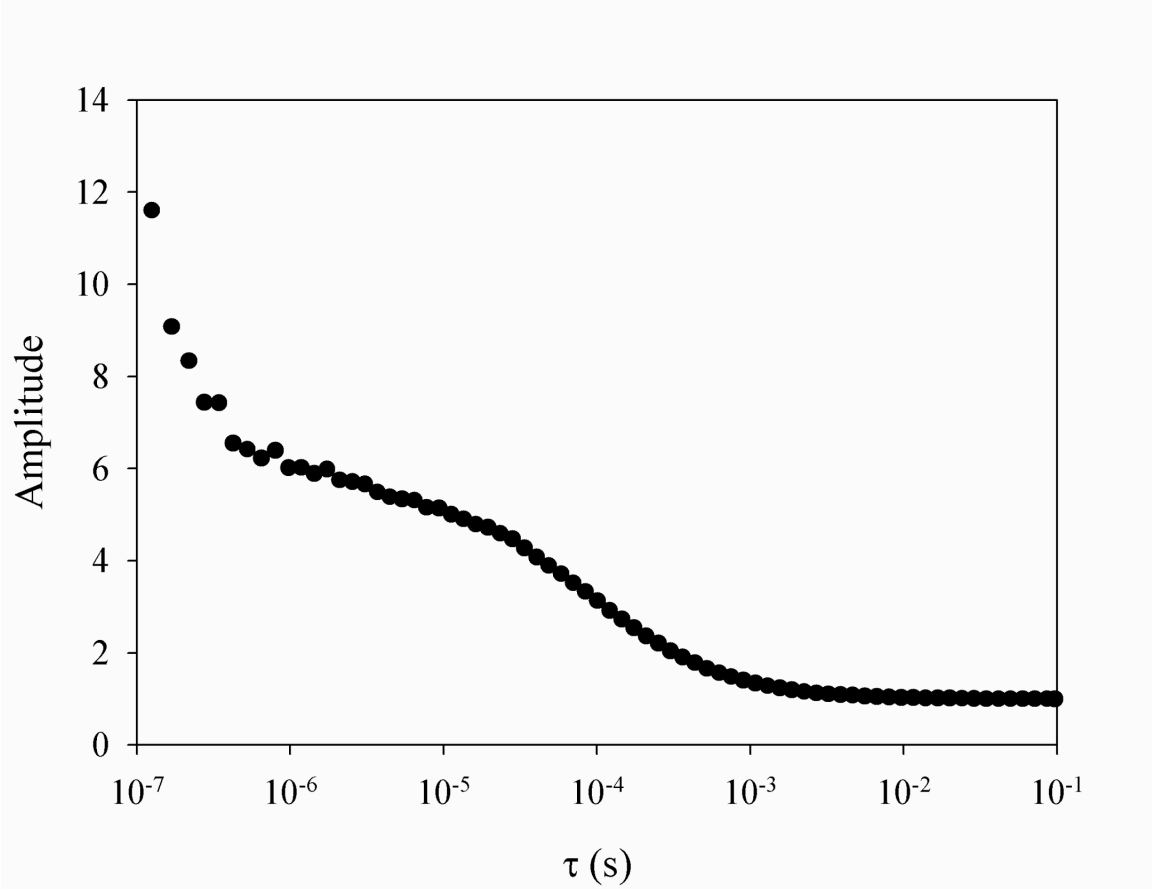


Figure 3.1: Example of normalized autocorrelation function. The ACF is obtained from Alexa Fluor 594 at a concentration of 25 pM, with a laser power of 30 μW at λ = 585 nm.

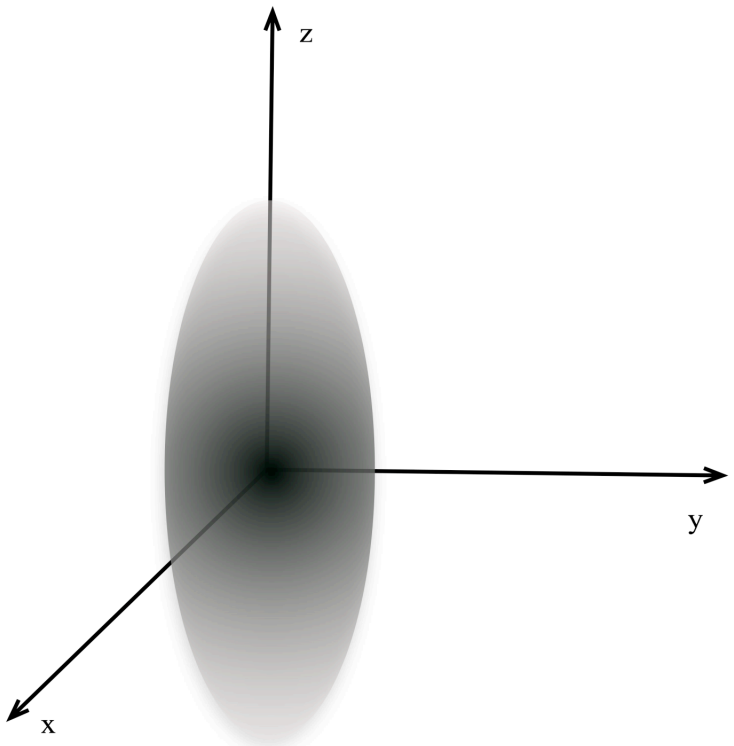


Figure 3.2: Three-dimensional Gaussian-ellipsoid volume.

through the sample volume, as is typically the case for FCS, the fitting function for the ACF is then given by [59,60],

$$G(\tau) = 1 + \frac{\zeta_j(\tau)}{N_{tot}}\left(1 - \frac{I_B}{I_{tot}}\right)^2 \sum_j \phi_j \left(1 + \frac{\tau}{\tau_j}\right)^{-1} \left(1 + \chi \frac{\tau}{\tau_j}\right)^{-1/2}. \tag{3.4}$$

Here, for each of the *j* species,

$$\zeta_j(\tau) = 1 + \left(\frac{\overline{T}_j}{1 - \overline{T}_j}\right) \exp\left[-\left(\overline{k}_T\right)_j \tau\right] \tag{3.5}$$

is a semi-empirical correction term for triplet kinetics [61], where $\left(\overline{k}_T\right)_j$ is the mean effective rate at which molecules are driven into the non-fluorescent triplet state, and $\overline{T}_j$ is the mean effective fraction of fluorophore *j* in the probe volume that is in the triplet state. Also, $I_{tot}$ is the total mean count rate

$$I_{tot} = \sum_j I_j + I_B, \tag{3.6}$$

which consists of the mean count rates from each species, $I_j$, and the uncorrelated background $I_B$. The factor $\phi_j$ is the weighting for the *j*-th species, given by

$$\phi_j = \frac{\Phi_j N_j / N_{tot}}{\left(\sum_j \Phi_j N_j / N_{tot}\right)^2}, \tag{3.7}$$

where $\Phi_j$ is the fluorescence brightness of the *j*-th species, $N_j$ is the mean number of molecules of the *j*-th species in the excitation volume, with $N_{tot} = \sum_j N_j$, and $\tau_j$ is the mean diffusional residence time for the *j*-th species, which is given by

$$\tau_j = \omega_0^2 / 4D_j, \tag{3.8}$$

where $D_j$ is the translational diffusion coefficient of the *j*-th species. Finally, in Eqn. 3.4 $\chi$ is the confocal parameter defined as

$$\chi = \left(\frac{\omega_0}{z_0}\right)^2. \tag{3.9}$$

For two species with similar fluorescence brightnesses and triplet kinetics, Eqn. 3.4 has the form

$$G(\tau) = 1 + \left(1 + ae^{-b\tau}\right)\left[\left(\frac{c_1}{c_1 + c_2}\right)\left(1 + \frac{\tau}{\tau_1}\right)^{-1}\left(1 + \chi\frac{\tau}{\tau_1}\right)^{-1/2} + \left(\frac{c_2}{c_1 + c_2}\right)\left(1 + \frac{\tau}{\tau_2}\right)^{-1}\left(1 + \chi\frac{\tau}{\tau_2}\right)^{-1/2}\right], \tag{3.10}$$

where, $c_1$ and $c_2$ are the contributions from each of the two species [61].

Before curve fitting of the ACF for the mixture is performed, calibration experiments with a fluorescent species that has a known diffusion coefficient, *D*, are performed to determine the confocal parameter, $\chi$, which can be held fixed in subsequent measurements. This calibration measurement can also be used to determine the confocal volume radius, as $\omega_0 = \sqrt{4D\tau_D}$, where $\tau_D$ is the mean diffusional residence time obtained from curve-fitting. Each species may also be investigated individually to obtain $\tau_j$. Then, the experimental ACF of the mixture is fit by varying *a*, *b*, $c_1$, and $c_2$.

If, in addition to diffusion, there is also an applied flow then the fitting function is altered by extra, Gaussian terms, and the ACF for a single species is given by [62]

$$G_{flow}(\tau) = 1 + \left(1 + ae^{-b\tau}\right)\left[\left(1 + \frac{\tau}{\tau_1}\right)^{-1}\left(1 + \chi\frac{\tau}{\tau_1}\right)^{-1/2}\right]\times$$
$$\exp\left[-\frac{(\tau/\tau_F^{(x)})^2}{1+\tau/\tau_1}\right]\exp\left[-\frac{(\tau/\tau_F^{(y)})^2}{1+\tau/\tau_1}\right]\exp\left[-\frac{(\tau/\tau_F^{(z)})^2}{1+\chi\tau/\tau_1}\right], \tag{3.11}$$

where $\tau^{(x)}_F$, $\tau^{(y)}_F$, and $\tau^{(z)}_F$ are respectively the x-, y-, and z-components of the flow, defined in terms of the flow velocities, $v_F^{(x)}$, $v_F^{(y)}$, and $v_F^{(z)}$ as

$$\begin{aligned}\tau_F^{(x)} &= \omega_0 / v_F^{(x)},\\ \tau_F^{(y)} &= \omega_0 / v_F^{(y)},\\ \tau_F^{(z)} &= z_0 / v_F^{(z)}.\end{aligned} \tag{3.12}$$

In the work discussed here, all flow is directed along the z-direction, which reduces Eqn. 3.11 to

$$G_{flow}(\tau) = 1 + \left(1 + ae^{-b\tau}\right)\left[\left(1 + \frac{\tau}{\tau_1}\right)^{-1}\left(1 + \left(\frac{\omega_0}{z_0}\right)^2\frac{\tau}{\tau_1}\right)^{-1/2}\right]\exp\left[-\frac{(\tau/\tau_F^{(z)})^2}{1+\chi\tau/\tau_1}\right]. \tag{3.13}$$

Figure 3.3 demonstrates the effect of an applied flow to the ACF.

Inspection of Eqn. 3.4 reveals that the amplitude of the normalized ACF, $G(0)$, is inversely proportional to the mean number of molecules in the probe volume. Therefore FCS is ideal for the examination of samples with low, i.e. picomolar to nanomolar, concentrations. For higher concentrations, it may prove advantageous to use other methods of data reduction.

It should be noted that the initial peak near the origin in the normalized ACF of Figure 3.1, with a decay time of ~200 ns, is caused by detector afterpulsing. This artifact can be corrected for, as described in [63], by the use of a calibration experiment of the ACF of clean water. Prior to the subtraction the ACF of water is scaled by the ratio of the

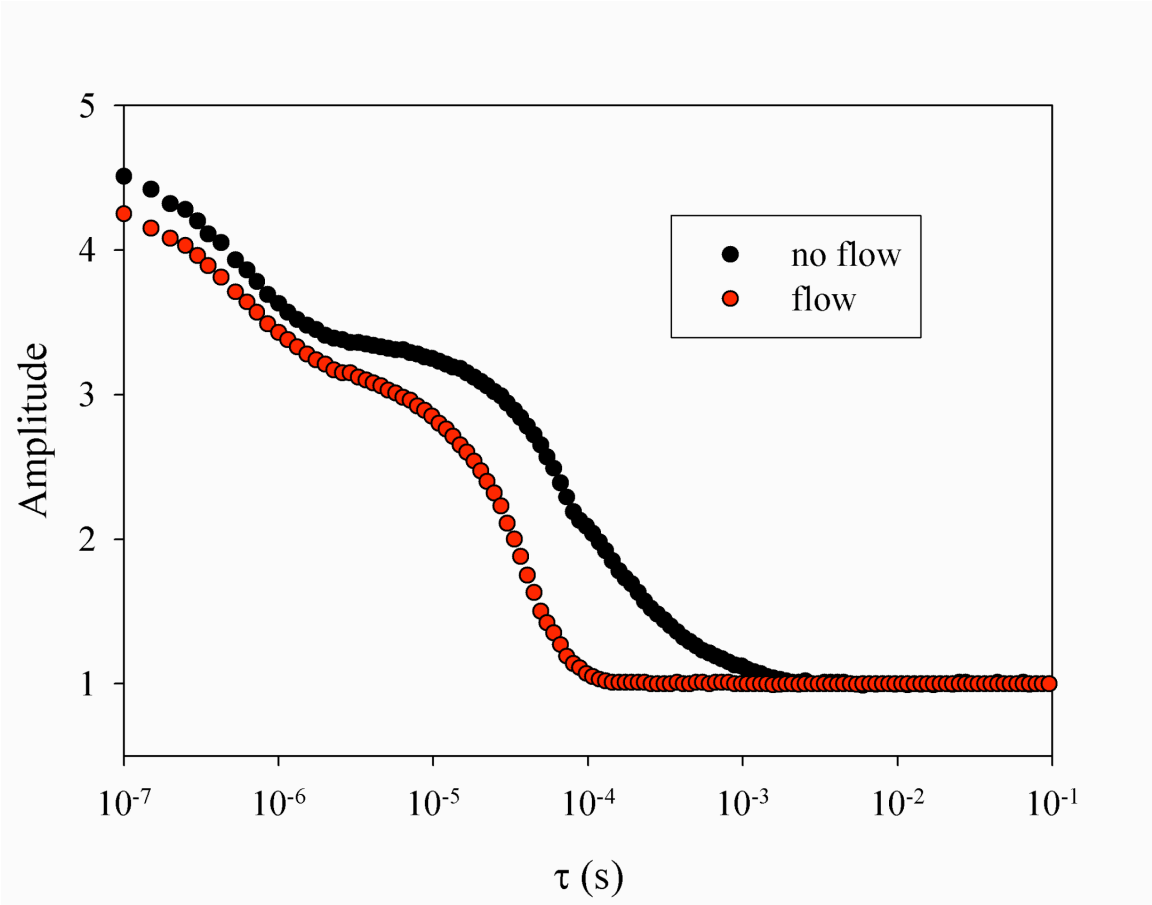


Figure 3.3: The effect of flow on normalized autocorrelation function.

count rate of the fluorescent sample to that of water.

## 3.2. Polarization Anisotropy

Polarization anisotropy is another method to distinguish between different solution components. In this case, however, instead of the use of differences in translational diffusion, changes in rotational motion can be observed. For linearly polarized excitation, the steady state fluorescence anisotropy, $r$, is defined as [11]

$$r = \frac{I_{\parallel} - I_{\perp}}{I_{\parallel} + 2I_{\perp}}, \tag{3.14}$$

with $I_{\parallel}$, and $I_{\perp}$, the collected fluorescence with polarization parallel, and perpendicular to the excitation polarization, respectively. Note that the denominator in Eqn. 3.14 is the total fluorescence irradiance, which is given by $I_{\parallel} + 2I_{\perp}$, and not simply $I_{\parallel} + I_{\perp}$. This is due to the fact that the total irradiance, $I_{total}$, is actually given by

$$I_{total} = I_x + I_y + I_z, \tag{3.15}$$

where $I_x$, $I_y$, and $I_z$ are the irradiances seen through a polarizer with its axis oriented along the x-, y-, and z-axis, respectively[11, pp 301-302]. For vertically polarized light, i.e. polarized along the z-axis, $I_x = I_y = I_{\perp}$, and $I_z = I_{\parallel}$, so Eqn. 3.15 is equivalent to

$$I_{total} = I_{\parallel} + 2I_{\perp}. \tag{3.16}$$

In the absence of rotational diffusion the fluorescence polarization anisotropy would be constant for a given molecule. With rotational diffusion the anisotropy is described by the Perrin Equation:

$$r = \frac{r_0}{1 + (\tau/\theta)}, \tag{3.17}$$

where $r_0$ is the anisotropy without rotational diffusion, $\tau$ is the fluorescence lifetime, and $\theta$ is the rotational correlation time. The rotational correlation time is related to the rotational diffusion coefficient, $D_{rot}$, and is dependent on the solvent viscosity, $\eta$, the volume, $V$, of the molecule, and the temperature, $T$,

$$\theta = \frac{1}{6D_{rot}} = \frac{\eta V}{RT}, \tag{3.18}$$

where $R$ is the gas constant.

## 3.3. Photon Counting Histogram

The remaining data reduction methods described in this chapter use fluorescence intensity fluctuations to distinguish solution components, the first of which is the Photon Counting Histogram (PCH). Experimentally, photon counts are still measured for PCH, therefore in order to obtain statistics of fluorescence intensities, the number of photon counts in a given sampling time is taken, and the resultant probability distribution is plotted. This section is meant to serve only as an introduction to this method, and for a more detailed description of PCH, the reader is directed to Refs [64,65].

The PCH distribution, $p^{(1)}(k;\ V_0,\ \varepsilon)$, for a single particle in a fixed volume, $V_0$, gives the probability of $k$ photons being detected in the specified time interval, and is defined as [65]

$$p^{(1)}(k;V_0,\varepsilon) = \frac{1}{V_0}\frac{\pi\omega_0^2 z_0}{k!}\int_0^\infty \gamma(k,\varepsilon e^{-2x^2})\mathrm{d}x. \tag{3.19}$$

Here $\varepsilon$ is the molecular brightness, measured in counts per second per molecule. This equation involves the incomplete gamma function, $\gamma$, and can be solved numerically.

Here, the excitation volume is approximated as a three-dimensional Gaussian given by Eqn. 3.1. Convolution is then used to give the PCH for $N$ particles from Eqn. 3.19,

$$p^{(N)}(k;V_0,\varepsilon) = \underbrace{(p^{(1)} * \cdots * p^{(1)})}_{N-terms}(k;V_0,\varepsilon). \tag{3.20}$$

So far, these equations assume that the system is closed, which means that particles are not free to move in and out of the probe volume. When extended to an open system, the number of particles in the excitation volume would have a Poisson distribution with mean, $\overline{N}$, which is related to the molar concentration, $C$, by $\overline{N} = CV_0N_A$, where $N_A$ is Avogadro's number. The PCH distribution for $N$ particles of a single species in an open system is then defined as

$$\Pi(k;\overline{N},\varepsilon) = \sum_{N=0}^{\infty} p^{(N)}(k;V_0,\varepsilon)e^{-\overline{N}}\left[\frac{\overline{N}^N}{N!}\right]. \tag{3.21}$$

This equation describes a super-Poissonian distribution, which means that the width is greater than the mean, and allows two parameters to be recovered, namely the molecular brightness, $\varepsilon$, and the average number of particles, $\overline{N}$. If the distribution were a simple Poissonian, in which the width equaled the mean, only a single parameter ($\overline{N}$) could be extracted.

PCH can be extended for use with multiple species, and thus has the capability to distinguish between different solution components. This is accomplished by a convolution of the distributions for the two (or more) individual species [66],

$$\Pi(k;\overline{N}_1,\overline{N}_2,\varepsilon_1,\varepsilon_2) = \Pi(k;\overline{N}_1,\varepsilon_1) * \Pi(k;\overline{N}_2,\varepsilon_2), \tag{3.22}$$

Therefore, two parameters for each species (the mean number of molecules, and the molecular brightness) can be extracted by use of this two-species model.

This technique has been used in the literature [66,67] to determine the molar fraction of two fluorophores in a mixture. More importantly, it has been demonstrated that PCH is a viable method for the distinction of labeled proteins that are bound to labeled ligands and those that are not, which demonstrates the usefulness of intensity-fluctuation analysis in the area of pharmaceutical drug discovery.

## 3.4. Fluorescence Intensity Distribution Analysis

FIDA is very similar to PCH described above. FIDA, like PCH, is used to analyze the amplitude of fluorescence bursts, which occur from chromophores traversing the excitation volume, by the integration of the photon counts over a given sampling time, or bin width [68]. The major difference between FIDA and PCH are the assumptions made about the probe volume shape.

Instead of assuming a three-dimension Gaussian laser irradiance profile as done with PCH, the probe volume for FIDA is divided into zones that have the same brightness. The bin width is chosen to be shorter than the time it takes for a molecule to diffuse from one zone to another. The probability distribution for $k$ photons being detected from the $i$th zone is a double Poissonian,

$$P_i(k;C,\varepsilon) = \sum_{m=0}^{\infty} \frac{(CdV_i)^m}{m!} e^{-cdV_i} \frac{(m\varepsilon B_i T)^k}{k!} e^{-m\varepsilon B_i T}. \tag{3.23}$$

Here $B_i$ and $dV_i$ are the brightness and the volume of the $i$th zone, respectively, and $T$ is the bin time. As defined with PCH, $C$ and $\varepsilon$ are the molar concentration and molecular brightness. A histogram of the number of photons per bin that is fit with Eqn. 3.23 will

extract the concentration and molecular brightness, much like PCH. FIDA can also be extended for multiple species, again like PCH, by convolution

$$P_i(k;C_1,C_2,\varepsilon_1,\varepsilon_2) = P_i(k;C_1,\varepsilon_1) \ * \ P_i(k;C_2,\varepsilon_2). \tag{3.24}$$

Another extension to FIDA has been to perform the histogram in two-dimensions (known as 2D-FIDA), with the use of a second detector [69]. The two detectors are usually used to collect different polarizations, but other aspects of the light can be used as well, such as wavelength. 2D-FIDA for polarization is one of the most frequently used diagnostics in the high-throughput screening platform of Evotech, which is a German company that has been a leader in the development and implementation of such technology. This technique is also useful for examination of Förster resonance energy transfer (FRET) [11, pp 367-394], because it allows the coincidence of two fluorophores to be visually determined.

There are some shortcomings related to FIDA. These are mostly due to the relationship of the bin times, and the diffusion of molecules. The fact that the bin time must be kept small with respect to the diffusion time, along with the necessity of the bin time being long enough to acquire sufficient photon statistics requires that the laser be focused less sharply for fast moving molecules. For slowly diffusing molecules, a tightly focused laser may be used. As with PCH, the fitting function involves numerical integrations and convolutions and is numerically intensive and slow to calculate.

## 3.5. Successive Photon Intensity Distribution Analysis

Successive photon intensity distribution analysis (SPIDA), or photon arrival-time interval distribution (PAID) is another technique used to obtain information about the fluorescence intensity distribution. Instead of the use of fixed bin times for the photons, however, SPIDA creates a two-dimensional histogram of times between different numbers of consecutive photons. While this technique also has the potential to assay species with different fluorescence brightness values, the theoretically derived fitting function for the experimentally collected histogram is also complicated and involves Monte Carlo integration [70].

## 3.6. Scanning Fluorescence Fluctuation Spectroscopy

With the use of active transport of molecules through the probe volume, differences that may exist in the species' diffusion coefficients become undetectable, as the mean residence time for each species is dictated by the flow velocity rather than diffusion. Therefore, FCS can no longer be used to find the relative abundance of sample constituents, and fluorescence brightness assays must be used.

Due to the complexities of the other methods discussed thus far and their limitations to situations without flow, it was desired to develop a new technique that uses a more empirical, and simpler fitting function. This new method, which is called scanning fluorescence fluctuation spectroscopy (S-FFS), begins by digital filtering of the photon stream with a weighted sliding sum filter where the weights are Gaussian in shape, with a width equal to the mean transit time due to flow, to accentuate the photon bursts caused

by traversing molecules [71]. The mean transit time is first obtained by the use of the curve-fit of the normalized ACF by use of Eqn. 3.13. A histogram of amplitudes of the digitally-filtered photon burts is then produced. The tail of this histogram is observed to be well approximated by an exponential. A threshold is applied to eliminate bursts that are caused by background sources. Because the statistics in the tail of the histogram are sparse, maximum-likelihood methods are used to find the decay rate of the tail, which is taken as a measure of the mean single-molecule fluorescence brightness.

A Monte Carlo simulation [62] was used to test the effectiveness of this method to determine the relative abundance of bound and free fluorescently labeled species. A simulated titration was conducted that was intended to model a competitive binding assay, similar to that shown in Figure 1.2b. In this case the three components include a fluorescently labeled protein, *T*, a fluorescently labeled ligand, *L*, and an unlabeled compound, *D*. The simulated titration is started with a mixture of the labeled protein and labeled ligand that bind with an assumed dissociation constant, $k_D = [T][L] / [TL] = 5$ nM, where [ ] represents the molar concentration of the particular species. Both *T* and *L* have a total concentration of 1nM with equal volumes of 100 μL. From this, the ratio of single-labeled species to double-labeled species was calculated to be 5.85. Next, the addition of 10 μL aliquots of the unlabeled compound, *D*, at a concentration of 1 μM was simulated, and the change in the ratio of single-labeled species to double-labeled species was determined from the cubic equation that results from the solution of the two simultaneous equations for $k_D$ that correspond to the two competing reactions

$$T + L \rightarrow TL, \tag{3.25}$$

and

$$T + D \rightarrow TD. \tag{3.26}$$

The unlabeled compound is assumed to bind to the protein with a dissociation constant of 1nM.

The Monte Carlo simulation was then run at each point of the titration by varying the ratio of single-, and double-labeled species. The simulated photon streams were then analyzed using the S-FFS algorithm, the results of which are shown in Figure 3.4. The theoretical value of the mean single-molecule brightness, obtained using the known concentrations of single- and double-labeled species, is also shown as a solid line. Note that although the mean molecular brightness changes during the titration (as the concentrations of double and single labeled species change) the net fluorescence signal remains constant. The simulations demonstrate the potential effectiveness of S-FFS, and provide a guide for the experiments reported in Section 7.2.

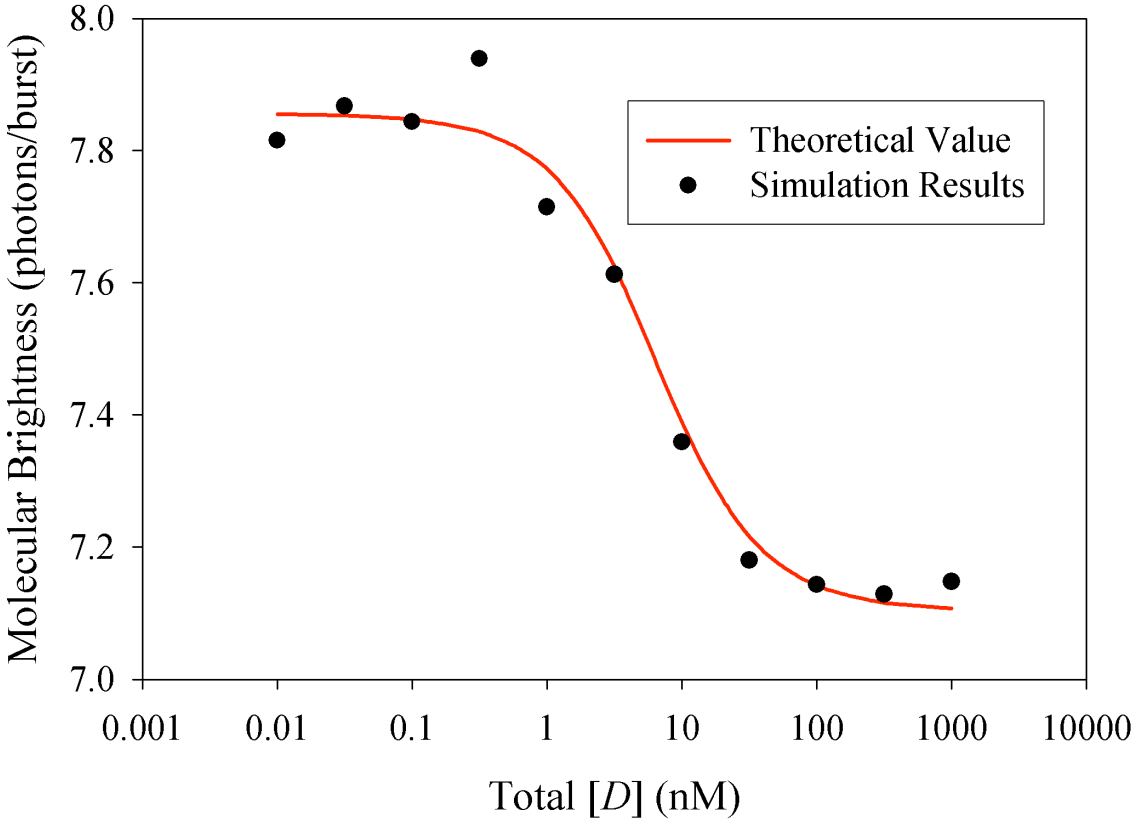


Figure 3.4: Molecular brightness calculated with S-FFS. Results are obtained from the simulated titration in which the concentration of drug-like compound, *D*, increases.

# Chapter 4

# Flow System

In a typical confocal microscope used for SMD and FCS, such as the commercial Zeiss Confocor 2, the volume of sample needed for a measurement is typically only ~100 μL. The reagent costs in pharmaceutical drug discovery are such that it is desirable to perform assays on samples of ≤ 100 μL. Therefore it is necessary to induce a flow in a very small volume sample, which can be achieved either by the use of micron-sized capillaries, or, alternatively, by microfluidic Lab-on-a-chip devices. The system chosen for this dissertation uses pressure-driven flow by use of a micron-sized capillary. This system, along with the method used for alignment, is described in Section 4.1. A discussion of the advantages and difficulties, and comparison with other possible methods, is presented in Section 4.2. Section 4.3 provides an approximate calculation of the minimum flow velocity that can be expected with a capillary of a given diameter.

## 4.1. Description of Flow System and Alignment Procedure

The flow system, which is shown in Figure 4.1, consists of a small borosilicate glass capillary, drawn to a tip with diameter of 5 or 10 μm (World Precision Instruments TIP5TW1LS01) aligned along the optical axis of the confocal microscope, as shown


Figure 4.1: Photograph of flow system.

schematically in Figure 4.2. The capillary is coupled to a manometer by a Luer connection and a three-way stopcock, which allows the flow to be turned on and off. The three-way stopcock also permits the attachment of a syringe to initially suck water up to the capillary from the manometer's reservoir. When the flow is turned on, the water in the manometer tries to fall back to the manometer, and a negative pressure-difference is created, the result of which is that the sample is drawn vertically upward into the capillary tip. Control of the observed flow speed is achieved by either the adjustment of the water height in the manometer, or by the alteration of the distance between the capillary opening and the laser focus.

The capillary is mounted on a precision xyz translation stage with submicron adjustability (Newport Corp., 462-XYZ-DM13). Alignment is done visually by the direction of collected light to either a microscope eyepiece or an intensified CCD camera (Princeton Instruments, I-Max). While the capillary is illuminated from above with white light, the eyepiece's wide field of view is used to get the tip approximately into focus, and to avoid the capillary tip hitting the coverslip. Then, the optical collection path is switched to the CCD, and the white light is turned off. The sensitivity of the CCD, along with the lack of any optical filters in this path, allows the laser light that is reflected from the tip to be used to bring the capillary more precisely into focus, and position it so that the focused laser beam is in the center. The capillary is finally translated vertically upward to the desired height above the laser focus, and the optical collection path is switched to the SPAD for data collection. An image of the capillary during the alignment procedure is shown in Figure 4.3. In this image the focused laser is seen as the bright spot near the center of the circular capillary, which has a 10 μm diameter.

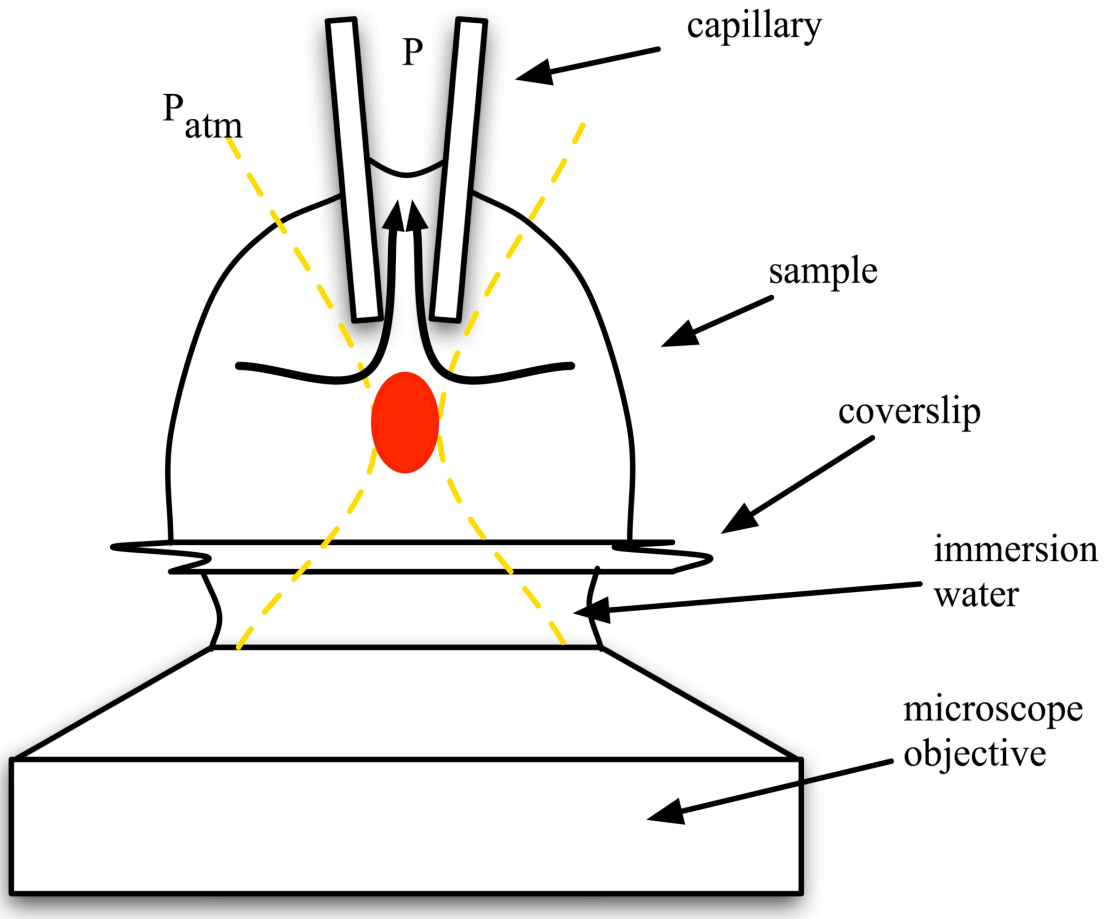


Figure 4.2: Schematic representation of the capillary used for inducing a flow in the sample. The capillary is aligned along the optical axis of the microscope.

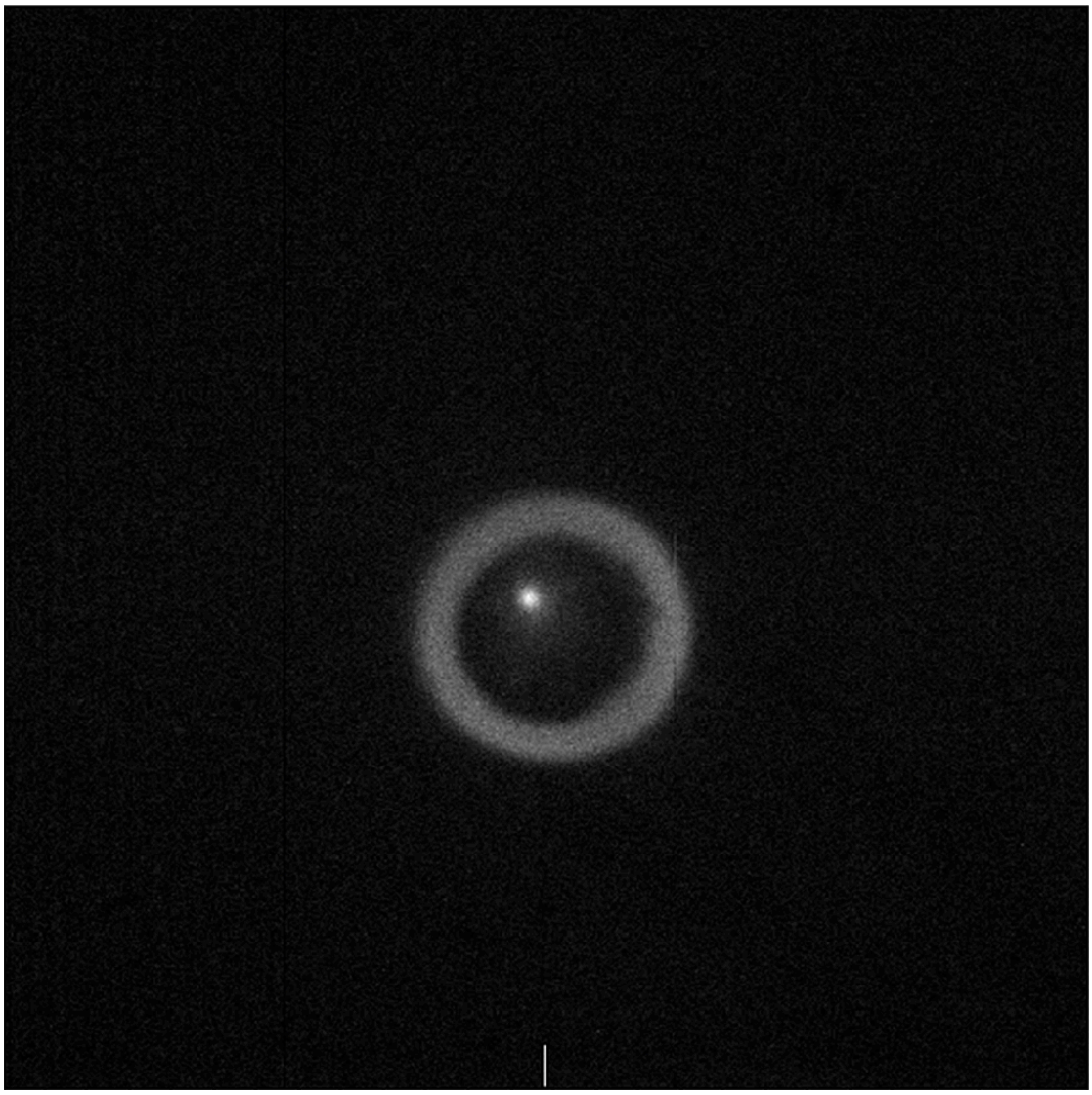

Figure 4.3: CCD image of 10 μm capillary during alignment procedure.

## 4.2. Comparison of Techniques for Inducing Flow

The use of capillaries was chosen as the method for introducing flow for the work described here, rather than microfluidic devices, because of several key advantages. Drawbacks of microfluidic devices include availability, cost of interface hardware, and potential problems with loading samples that can adsorb inside the walls of the device. Glass capillaries are low cost, and may be replaced for each new sample. The capillary also offers the flexibility of inducing flow along the optical axis of the laser beam, but outside of the capillary, while microfluidics are generally planar and can provide flow only transverse to the optical axis.

Some of the issues that needed to be considered for the design of the flow system include capillary size, and material, orientation with respect to the optical axis of the microscope, the type of flow to use, either pressure-driven or electrokinetic, and how to maintain a steady flow rate. Here, these concerns are illustrated along with some other problems that occurred and how they were solved.

There is a trade-off that must be considered for the diameter of the capillary opening. If the opening is too large, then fluorophores will not necessarily pass through the focused laser, and the sample will be consumed too quickly. On the other hand, if the opening is too small, the flow velocity may be insufficient to dominate diffusion, there is a greater probability that the capillary will become blocked, and there may be additional background due to autofluorescence of the tip.

Autofluorescence is typically only present for glass capillaries, and so could be eliminated by use of a different material, such as fused silica. However, these capillaries

are much more expensive than those made of glass, and there is another option for the reduction of this autofluorescence background. With the use of a confocal microscope for detection, if the tip is moved sufficiently away from the laser focus, the microscope spatial filter should block the autofluorescence. As discussed below, movement of the tip away from the focus reduces the observed flow velocity of the fluorophores, but an increase in the pressure can compensate for this.

In the experiments discussed here, glass capillaries were used which had an opening of 10 μm, and measurements were executed with the tip of the capillary positioned between 25 and 50 μm above the laser-beam waist. These conditions provide sufficient flow velocity to dominate diffusional motion, while almost all background due to glass autofluorescence is eliminated.

The orientation of the flow was also something that needed to be considered. Previous work by others concentrated on the use of flow to direct molecules through the probe volume, in an effort to increase the net efficiency of SMD [14,15,20]. In these studies, volumes on the order of picoliters were used. In the latter, time-gating was also used to further eliminate background caused by Raman scattering. The probe volume has since been reduced to the order of a fraction of a femtoliter with the incorporation of confocal microscopy [72]. Another common feature of these early studies was that the excitation and collection paths were perpendicular to each other. In the work described here, it was decided to orient the capillary along the optical axis, which allows a longer interaction time, as the probe volume in a confocal microscope is well approximated by an ellipsoidal three-dimensional Gaussian function, in which the axial diameter is typically 5-7 times that of the radial diameter [73].

In order to obtain a steady, and repeatable, pressure-driven flow velocity several methods were investigated. First, the capillary was simply attached directly to a manometer made from a small diameter (~1/4 inch) tube that was partially filled with water. Although this setup did produce an adequate flow velocity to overcome diffusion, the small surface area of the water in the manometer caused the flow velocity to change over the course of the experiment. Also, with this arrangement the capillaries being used had a threaded connection, which in practice was found to be quite difficult to properly seal, and the exchange of capillaries was also difficult.

In some experiments, a syringe was used to apply pressure to induce a flow, but this proved to be impractical due to the fact the syringe had to be held in a fixed position for the entirety of the experiment. Due to the extreme forces, this led to the breakage of one syringe. This setup also made it difficult to make fine adjustments of the flow velocity.

The design finally settled upon was another form of the manometer. Instead of the use of a U-shaped tube filled with water, in this case a large reservoir is connected to the capillary with a water-filled tube. Adjustment of the reservoir height in relation to the height of the sample can then control the pressure. The large surface area in the reservoir assures a much more consistent pressure and almost entirely eliminates the fluctuations that occurred with the other design. The method for the connection of the capillary to the tubing was also changed from the threaded connection to a Luer connection, which gives a better seal, and makes it easier to exchange capillaries.

## 4.3. Estimate of Minimum Flow Velocity

As discussed above, in order to perform single-molecule detection with flow, the residence time due to flow should dominate the diffusional residence time. Initial experiments were performed with capillaries with tip diameters of 0.5 μm, but resulted in insufficient flow velocities. Therefore, it was necessary to calculate the expected flow velocity for certain experimental arrangements, i.e. the required pressure, capillary diameter, and the distance the capillary should be from the laser focus. Because the exact dimensions of the tapered tip of the capillary could not be easily measured, an experimental approach was taken. This was accomplished by measurement of the volumetric flow rate, and the use of this to estimate the linear flow velocity at the capillary opening and at various distances away from the tip.

At the tip of the capillary, the mean linear flow velocity may be estimated to be

$$v = \mathrm{V}/(\pi r^2), \tag{4.1}$$

where V is the measured volumetric flow rate and $r$ is the capillary tip radius. At a distance $d > r$ away from the capillary tip, the linear flow velocity is at least

$$v = \mathrm{V}/(4\pi d^2). \tag{4.2}$$

This expression underestimates the flow velocity, as it assumes that the flow is uniform over an entire sphere of radius $d$, which is not the case, as the sample droplet and capillary each have finite size and the flow lines are not spherically symmetric, but will be similar to those depicted in Figure 4.1.

For the active transport to dominate diffusion, the flow velocity should be such that

$$\tau_F^{(z)} = \frac{z_0}{v} << \tau_D . \tag{4.3}$$

With typical values of 100 μs for $\tau_D$, and 5μm for $z_0$, and a measured volumetric flow of 0.5 μL $s^{-1}$ with use of a capillary with a radius of 5 μm, the capillary tip should be positioned ~30 μm from the laser focus for the flow to dominate diffusion. The measured volumetric flow rate also indicates that a sample volume of 100 μL would be completely consumed after ~200 s.

# Chapter 5

# Experimental Setup

For most SMD investigations, whether by use of one- or two-photon excitation, a confocal epi-illumination setup is used. This chapter gives an overview of the system used for the single-molecule studies that are discussed herein. Our setup consists of a custom-built confocal microscope that can be used with several different lasers, and a photo-detector that is connected to a data acquisition card in a PC. In this chapter each of these parts will be described in detail starting with the confocal microscope in Section 5.1. The available laser systems will be outlined in Section 5.2, and the hardware and software used for data acquisition and analysis will be discussed in Section 5.3.

## 5.1. Confocal Epi-Illumination

Although there are commercially available confocal microscopes, such as the Zeiss ConfoCor 2, these systems cost half a million dollars or more, and do not have the flexibility of a custom-built microscope. For example, the ConfoCor 2 presently does not permit polarization-resolved fluorescence measurements. Therefore it was decided to build a custom apparatus to perform the single-molecule studies that are shown here. This system needed to have the capability to be used with all of the different available lasers

with minimal changes to the optical configuration. It was also decided to use an inverted layout for the microscope, i.e., the sample is placed on top of a coverslip, which is held over the objective lens, and the sample is excited by epi-illumination. Another desirable feature was the ability to change between confocal, or point detection, and wide-field imaging.

Figure 5.1 shows a photograph of the version of the custom-built microscope that was used for the work reported here, and the schematic is given in Figure 5.2. Any of the five available lasers can be steered into the system, which allows great flexibility in the fluorophores that are examined. The horizontally polarized laser beam is brought to the sample by reflection of the s-polarized beam from an uncoated fused-silica beam-sampler (Newport Corp., 10Q20NC.1). Whereas most confocal microscopes use a dichroic filter to introduce a specific excitation wavelength, the beam-sampler allows the use of different laser excitation wavelengths without the need for realignment, and gives ~10% Fresnel reflection, while the remaining 90% of the beam is dumped.

The beam is focused into the solution with a water-immersion objective (Olympus, UPLAPO660XW, 60×, 1.2 N.A.). Emitted fluorescence is then collected with the same objective lens, passes through the beam-sampler, is focused by lens 1 with a focal length of 250 mm. This differs from the usually used 180 mm focal length tube lens, and hence the magnification is 83.3. Collected light then passes through a spatial filter, typically either 75 or 150 μm in diameter, which correspond to 0.9 and 1.8 μm in object space, respectively. The purpose of the pinhole is to reject fluorescence coming from molecules that are out of focus. This is unnecessary for TPE, where the fluorescence

Figure 5.1: Photograph of the custom-built fluorescence microscope.

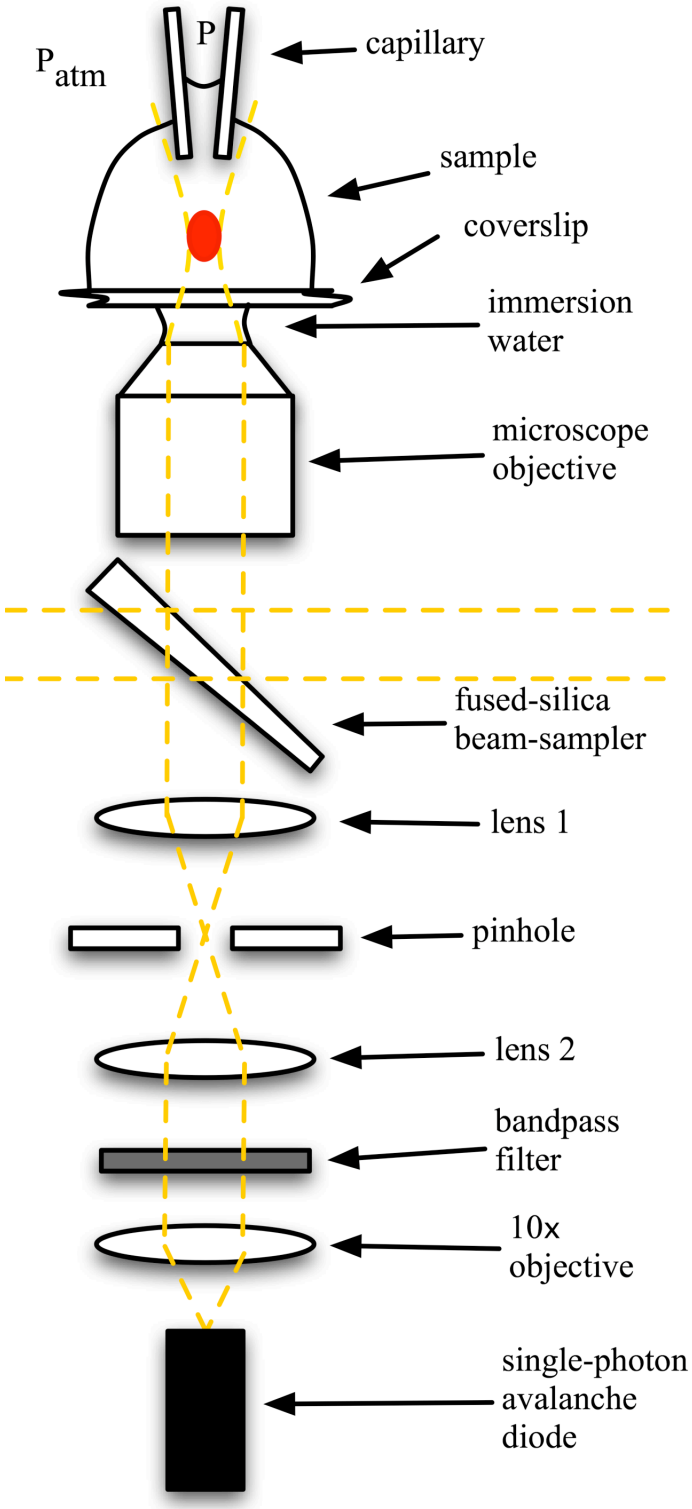


Figure 5.2: Schematic diagram of the custom-built fluorescence microscope.

emission is proportional to the square of the laser irradiance, and therefore the spatial filter is typically replaced with a larger pinhole for this configuration. After recollimation, the collected light passes through a bandpass filter to eliminate any Rayleigh scatter from the solvent molecules. The choice of filter depends on the fluorophore being observed and the excitation source. For example, with Alexa Fluor 594 excited with a wavelength of 585 nm, the chosen filter is centered at 617 nm, with a bandwidth of 45 nm (Omega Optical Inc., 617DF45), while for Alexa Fluor 647 excited with 630 nm, a filter with a center wavelength of 675 nm, and a bandwidth of 50 nm (Omega Optical, Inc., 3RD650-700) is used. The light transmitted through the filter is then focused onto a photo-detector (Perkin-Elmer SPCM-AQR15). The detector and the data-acquisition cards that it can be connected to are discussed in Section 5.3.

As mentioned above, the microscope could also perform wide-field detection by use of a CCD camera. This is realized by the addition of a mirror between the fused-silica beam-sampler and lens 1 of Figure 5.2 to direct the imaged fluorescence onto the camera. The use of the camera also aids in the alignment of the capillary for active transport experiments.

## 5.2. Laser Systems

There were five lasers available for the experiments described here, which allow the use of many different fluorescent dyes. The lasers, shown in Figure 5.3, include a Neodymium-Yttrium Aluminum Garnet (Nd-YAG) (Spectra-Physics Vanguard), two dye lasers (Coherent 700), an Argon Ion (Spectra-Physics BeamLok), and a Titanium-

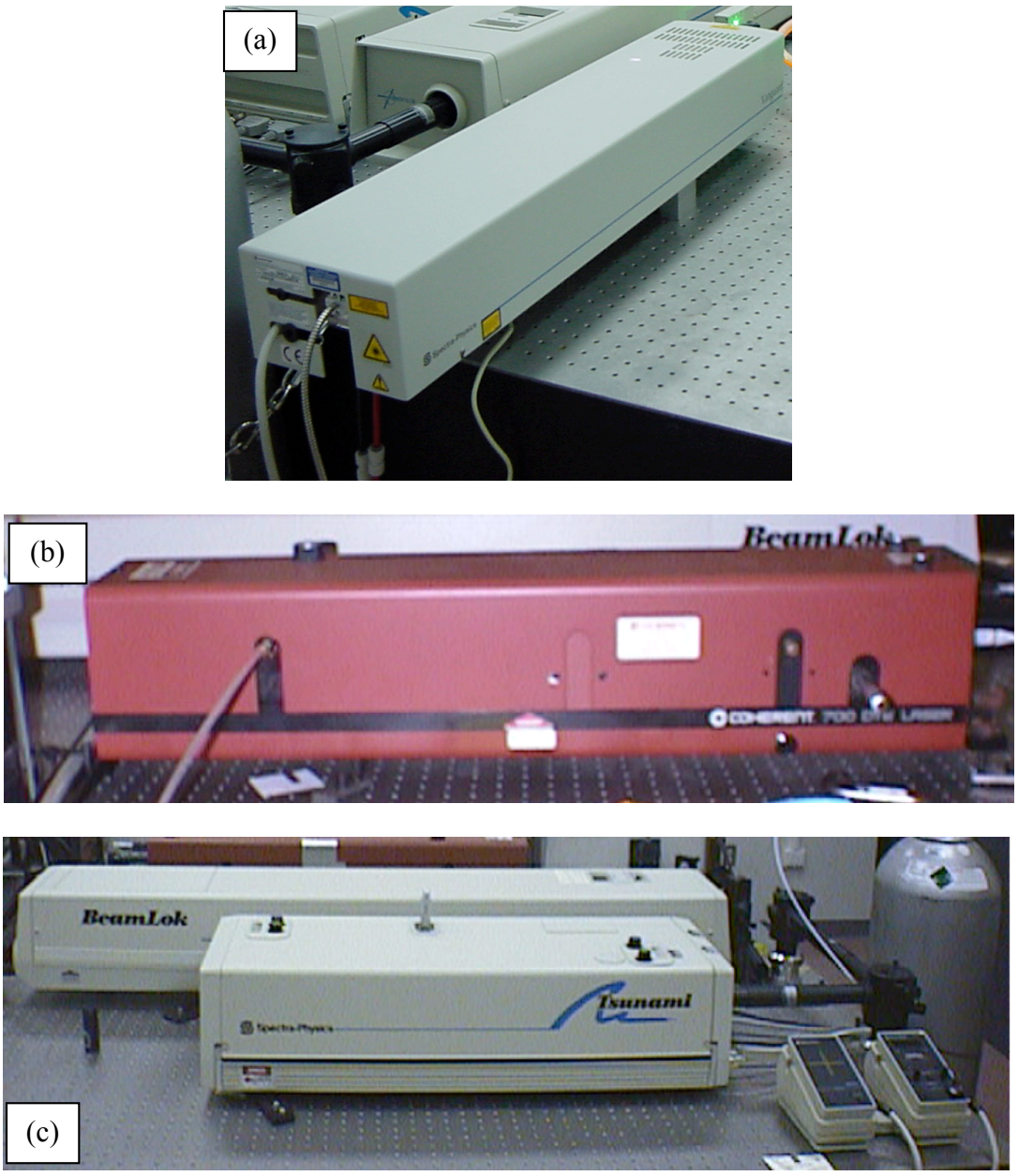


Figure 5.3: Available laser systems. (a) Spectra-Physics Vanguard Nd:YAG, (b) Coherent 700 Dye laser, (c) Spectra-Physics BeamLok Argon ion (background), and Tsunami Ti-Sapphire (foreground).

Sapphire (Spectra-Physics Tsunami). The different systems also allow for the investigation of differences between pulsed- and cw-excitation as described in Section 2.1.

In the initial stages of this research, the Nd-YAG laser was a Coherent Antares 76-S. Much effort was made to keep the Antares working as long as possible, but it was no longer supported by Coherent, and therefore to continue its operation another used Antares was purchased for spare parts. When all spare parts for the power supply were exhausted, the Spectra-Physics Vanguard was chosen as a replacement. The Vanguard is pumped by a fiber-coupled diode laser, and is frequency-doubled, which gives an output wavelength of 532 nm. It is passively mode-locked to produce 12 ps pulses at a repetition rate of 76 MHz. The time-averaged power is factory-set at 2 W, which gives a peak power of ~2 kW.

The two available dye lasers contain different fluorescent dyes and optics, which allow a wide tuning range. One is run with Rhodamine 6G, which is tunable from 560-605 nm, while the other contains DCM Special, tunable from 605-675 nm. Both are synchronously pumped by the frequency-doubled Nd-YAG laser. The average output power from both dye lasers varies slightly with wavelength, but is on the order of 100 mW, with a peak power on the order of ~100 W. Although the dye laser containing Rhodamine 6G has been in continuous operation for a number of years, the other dye laser was brought into operation as part of the research for this dissertation and parallel research efforts.

Also available is the Argon ion laser, which produces cw radiation, and includes two high-reflector optics: a broadband high-reflector, for all-lines operation, when it is

used to pump the Titanium-Sapphire laser, and a prism assembly that allows single-line operation at the Argon-ion wavelengths, typically 488 nm and 514.5 nm. The all-lines specified power of the Argon-ion laser is 10 W.

The final laser is the Titanium-Sapphire, which is used for all TPE experiments. The Titanium-Sapphire laser is tunable in the near IR from 720-850 nm with the standard optics set; this set can be changed to allow tuning from 800-980 nm. It produces ~60 fs pulses with a repetition rate of 76 MHz. The time-averaged power is approximately 500 mW, which gives a peak power of ~100 MW.

The Tsunami was also used for a collaborative project with Prof. K. H. Lee from Kongju National University, in which the photoluminescent properties of porous silicon were investigated [74]. For these experiments, the Titanium-Sapphire beam was frequency-doubled to 410 nm by use of a $\beta$-$BaB_2O_4$ (BBO) crystal. The fluorescence lifetime was measured at numerous points for several porous silicon wafers, each of which had anodized for a different amount of etching time.

There are also several tools that were used throughout this research for laser diagnostics, which include an autocorrelator (Femtochrome Research, Model FR-103), and a spectrometer (Thermo Jarrell Ash Corp. MonoSpec 27) used in conjunction with an optical multichannel analyzer (OMA) (EG&G, PARC, Model 1460). The autocorrelator is used to measure the output temporal pulse-width of the lasers, with a resolution of 50 fs, while the OMA is utilized to measure the emission spectrum and monitor the mode-locking of the Tsunami.

## 5.3. Data Acquisition and Analysis

The data acquisition is accomplished with the use of the aforementioned SPAD, along with one of two PCI cards, and both commercial and custom software. The PCI card that is used depends on the type of information that is desired. For fluorescence lifetime measurements, a TimeHarp 200 card (PicoQuant) is used while for SMD and FCS a National Instruments PCI-6602 is used.

The National Instruments PCI-6602 is typically used for FCS and SMD investigations, because it has zero dead time, whereas the TimeHaro 200 has a 300 ns dead time, which results in a loss of photons during photon bursts, where photons are closely spaced in time. Also, the PCI-6602 has a faster 80 MHz on-board clock, compared to the 10 MHz clock on the TimeHarp 200 card. The PCI-6602 board has 10, 32-bit, counter-timers, but only 3 direct memory access (DMA) channels for rapid transfer of data to the PC. The counter source is connected to the 80 MHz clock, and the SPAD TTL pulses are directed to the gate-input of the counter, so that each time a photon is detected, the counter is read, which yields the photon time-of-arrival (TOA) with a resolution of 12.5 ns. Custom LabView software developed by L. Davis then calculates the normalized ACF and the photon bursts, as shown in Figure 5.4, directly from the stream of photon TOAs [62].

The TimeHarp 200 card is utilized for time-correlated single-photon counting (TCSPC) to determine the time difference between the TTL pulses from the detector and the laser pulse. The TimeHarp 200 operates in the reverse start-stop mode, which indicates that the pulse from the detector is used as the start signal while the laser pulse is

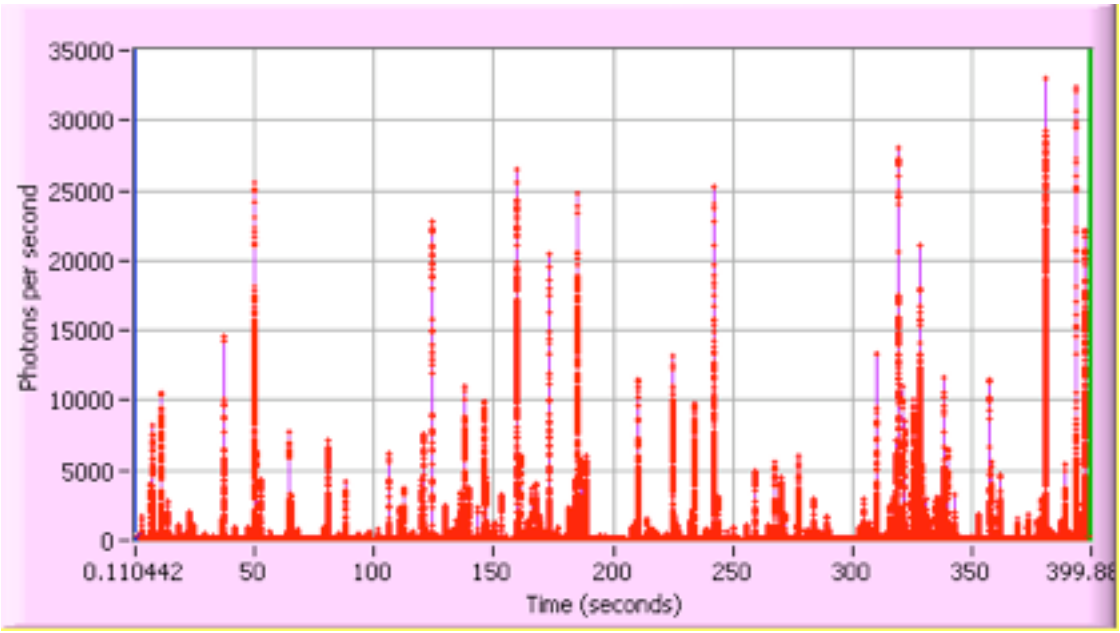


Figure 5.4: Photon burst graph from the LabView data collection program.

used as the stop signal. This mode of operation is much more efficient than the opposite case in which the laser pulse is used to start, and the detector pulse is used to stop the counter as there would be many laser pulses that were not followed by a detector pulse and would result in excessive electronics dead time. Actually, the use of laser pulses as the start signal would not be possible with the TimeHarp 200 and the 76 MHz repetition rate of the pulsed lasers used here, as the 300 ns dead time is greater than the time between laser pulses.

The start signal consists of TTL pulses produced by the detector, which are passed through a constant fraction discriminator (CFD) on the TimeHarp 200. The CFD would provide precise timing information from detector pulses with varying amplitude, such as photomultiplier tube pulses. The CFD is unnecessary when SPADs are used, as the output pulses always have an amplitude of 5 V. A leading edge discriminator is used for the well-defined laser pulses. These two signals are then used as the start and stop signals for the time to digital converter (TDC) of the TimeHarp 200, which has a base resolution of 34 ps, 300 ns dead time, and a maximum conversion rate of 3 MHz. The TDC provides the digital timing value to the histogrammer, which has 4096 channels. The histogram memory is then made available for data readout, and displayed by use of the software that is included with the PCI board. The TimeHarp 200 also has an optional router (PicoQuant, PRT400), which allows up to four detectors to be used simultaneously.

The TimeHarp software also has a time-tagged time-resolved (TTTR) mode, in which the start-stop timing of each photon event is recorded along with a time-tag from an independent 10 MHz clock. The resulting 32-bit records are then queued in a first in first out (FIFO) buffer, the output of which is continuously sent to the PC. One advantage

of using this mode with the TimeHarp 200 over the National Instruments PCI-6602 card is that the fluorescence lifetime can be simultaneously collected with the photon TOAs.

# Chapter 6

# Prototype Four-Channel Photon Detector

In this chapter the evaluation of a prototype four-channel SPAD (Perkin-Elmer, SPCM-AQ4C) is discussed. The use of several detection channels allows for more information to be obtained, which would aid in the determination of the fraction of free and bound fluorophores in pharmaceutical drug discovery. The incorporation of four detectors that collect at two wavelengths and two polarizations would make it possible to perform FCS, 2D-FIDA, and fluorescence polarization measurements simultaneously. The four-channel SPAD offers a more cost-effective solution for multi-channel detection than four single-channel modules. The prototype was loaned from Perkin-Elmer Optoelectronics division (Vaudreuil, Canada) for the purpose of its evaluation.

The experimental setup used for the evaluation is described in Section 6.1. A comparison of the four-channel SPAD with a Perkin-Elmer single-channel SPAD is discussed in Section 6.2, and Section 6.3 details one problem that occurs with the four-channel SPAD. A summary of the evaluation is given in Section 6.4.

## 6.1. Experimental Setup for Evaluation

A photograph of the four-channel detector is presented in Figure 6.1. Initial measurements were taken with each of the four channels of the SPCM-AQ4C individually to characterize the afterpulsing probability and dark count rate from each channel for comparison with the single-channel detector. The results of these comparisons are described in Section 6.2 below.

Next, the system was set up to evaluate the performance in a multichannel optical configuration. A schematic of the experimental setup for this evaluation of the four-channel module is shown in Figure 6.2. This setup is the same as that described above for single-channel measurements, except that the collected light passes through a polarizing beam splitter (Newport Corp., 05FC16PB.5). Both of the resulting beams are then directed to a dichroic filter (Omega Optical, Inc., 650DRLP), which reflects wavelengths less than 650 nm, and transmits long wavelengths. Each of the four beams are then filtered by use of bandpass filters, which results in two polarization channels, each with two wavelength bands. In order to couple the light to the detectors in a cost-effective and low-loss manner, a fiber collimation package (Thorlabs, F260FC-B) which is anti-reflection coated for use with 600-1050 nm light was selected and used with 1 m fiber optics (Oz Optics, N.A. 0.29, 100 μm core/140 μm cladding). The signals from the four detectors were then directed to the TimeHarp 200 card via the PRT400 router for time-resolved single-photon counting.

To test the SPCM-AQ4C's usefulness in determining the relative abundance of free and bound species, experiments were conducted with mixtures of Biocytin labeled

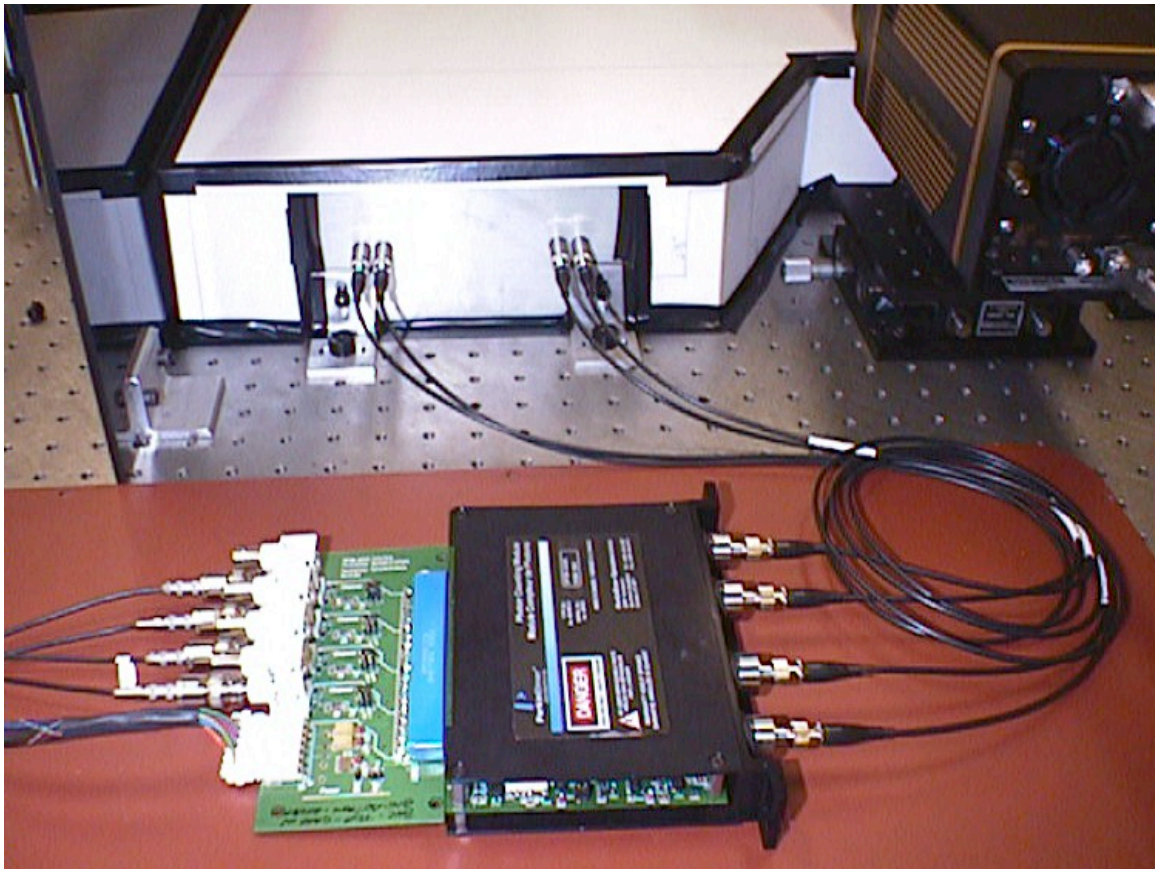

Figure 6.1: Photograph of the Perkin-Elmer SPCM-AQ4C.

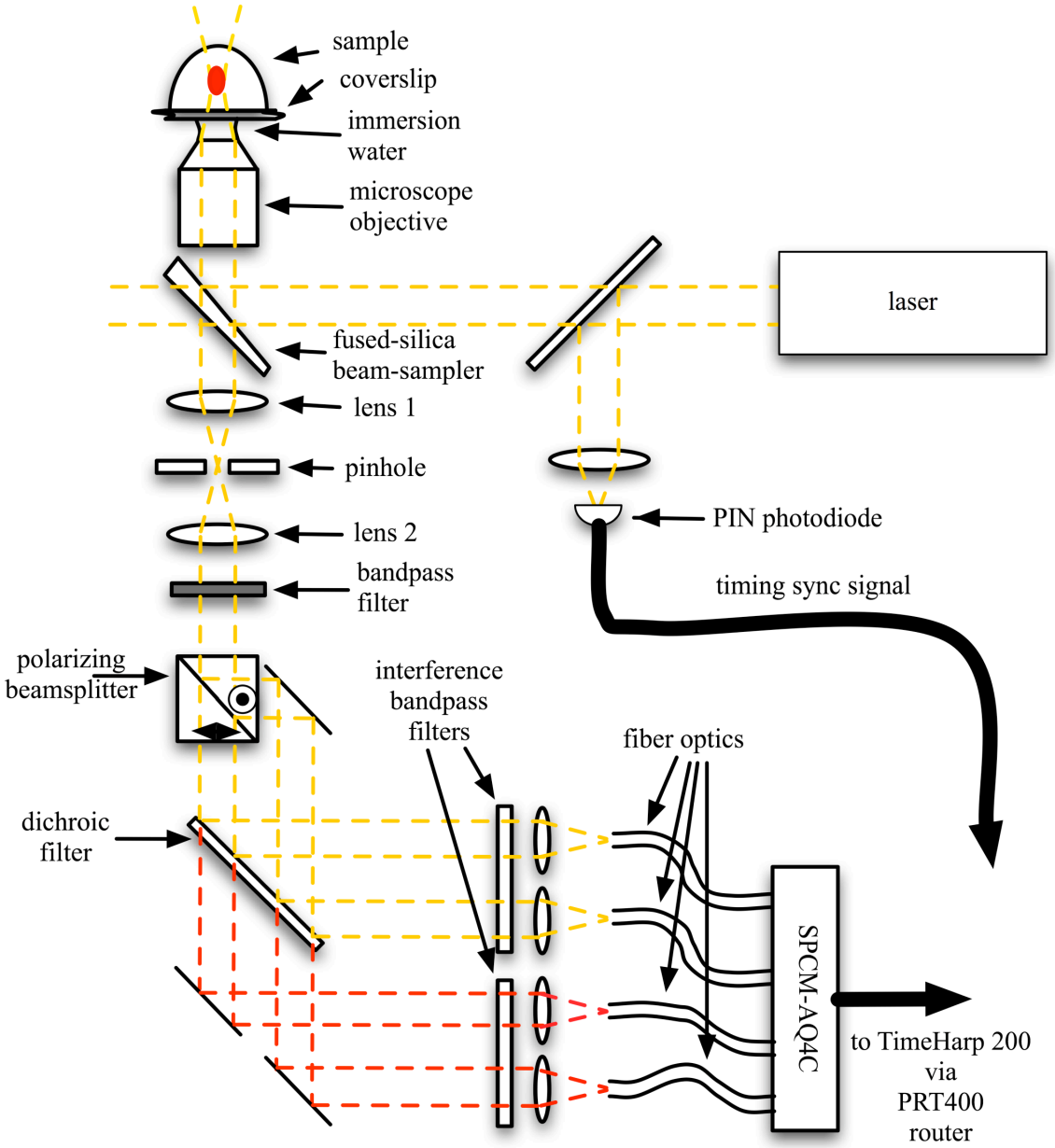


Figure 6.2: Schematic diagram of the setup used for testing of the Perkin-Elmer SPCM-AQ4C.

with Alexa Fluor 594 (Invitrogen, A-12922) and Anti-biocytin labeled with Alexa Fluor 647 (Invitrogen, A-31625), which are known to bind with a dissociation constant of 1 nM [75]. Example data obtained with the prototype four-channel detector, and these two solution components excited with a picosecond pulsed laser wavelength of 585 nm are shown in Figure 6.3. Figure 6.3c shows the fluorescence lifetime with a constant concentration of Alexa Fluor 594-labeled Biocytin and increasing concentration of Alexa Fluor 647-labeled Anti-biotin as measured on channel 0 of the four-channel module. It can be seen that the apparent fluorescence lifetime decreases with increasing concentration of Alexa Fluor 647-labeled Anti-biocytin, which could be caused by FRET due to Biocytin-Antibody binding, but is also partially due to direct excitation of the Alexa Fluor 647.

## 6.2. Comparison with Single Channel Detector

The Perkin-Elmer single-photon counting module (SPCM) uses a SPAD that is fabricated from super low K (SLIK) silicon, where K is the fraction of the effective ionization coefficient of electrons to that of holes [17]. The SLIK SPAD enables high quantum efficiency single-photon detection, which makes it ideal for ultra-sensitive fluorescence detection. The first SPCMs that were commercially available had a passive quenching circuit, which had a long dead-time of 200-800 ns, which resulted in limited photon count rates, but enabled time-resolved single-photon detection with a prompt full-width at half maximum (FWHM) of ~135 ps. Current modules have an active quenching circuit and TTL pulse output, which reduce the dead-time to ~35 ns, but broaden the prompt FWHM

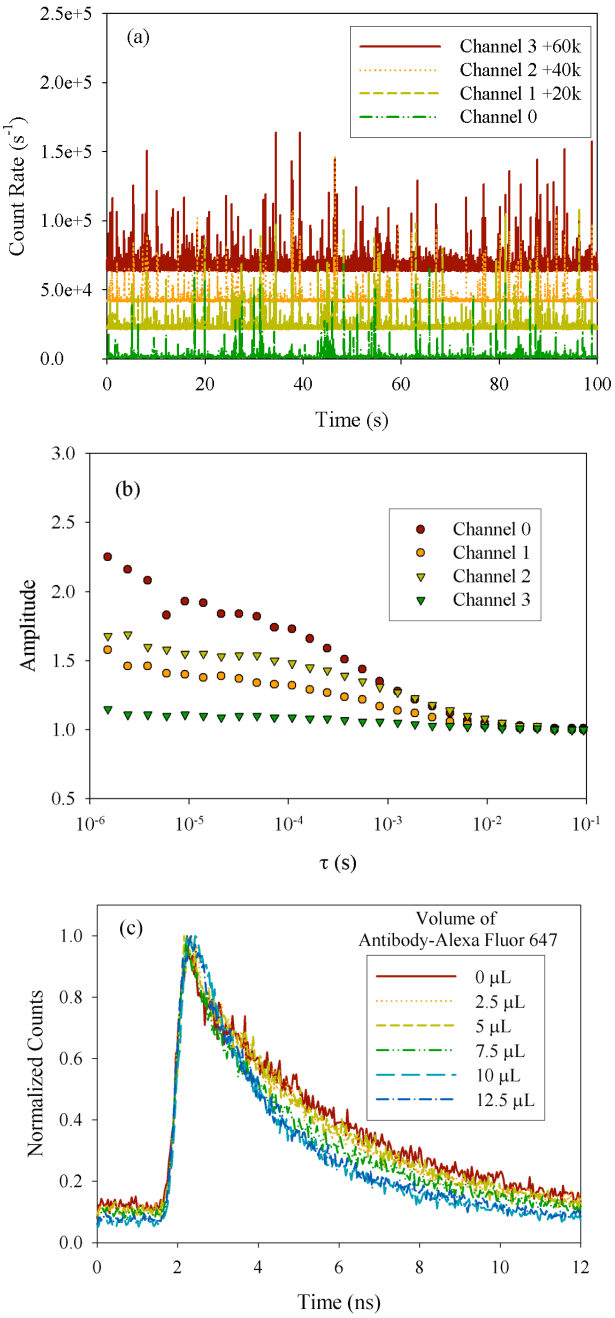


Figure 6.3: Example data from the Perkin-Elmer SPCM-AQ4C. (a) Count rate vs. time, (b) normalized ACF, and (c) fluorescence lifetime obtained with mixtures of Biocytin-Alexa Fluor 594 and Antibody-Alexa Fluor 647 excited with l = 585 nm, and laser power = 30 mW.

to ~300 ps [18]. The four-channel unit uses the active quenching circuitry, but there are some differences between the two types of modules.

One major difference between the single-channel and four-channel module is the method used to deliver light to them. For the single-channel unit, light is focused to a 10 μm spot at the center of the 150 μm active area of the SPAD with an objective lens, although fiber-optically coupled single-channel SPADs are also available. However, for the four-channel module, fiber optic coupling is the only option to deliver light to each individual detector. Although this method does allow greater flexibility in the position of the SPAD inputs, it also slightly reduces the coupling efficiency due to reflections from the fiber ends, and may degrade the timing performance.

The four-channel unit also has redesigned circuitry to protect against catastrophic failure, but which also results in slightly longer dead-times of ~50 ns. However, for the evaluation of this device, the TimeHarp 200 with a dead time of 300 ns was used, so the change in detector dead-time is insignificant.

The maximum photon count rate that the four-channel module can handle is also lower than that of the single-channel unit. Each of the four SPADs can handle $2 \times 10^6$ photons/s, down from $10^7$ photons/s for the single-channel module. This is usually not a problem, as the count rate is usually well below $10^5$ photons/s for the typical SMD or FCS experiment.

An improvement over the single-channel SPAD is the four-channel module's specified detector afterpulsing probability. This is decreased from 0.5% for the single-channel to 0.2% for the four-channel module. The detector afterpulsing can be observed by collection of an ACF with clean water, such as shown in Figure 6.4. Detector

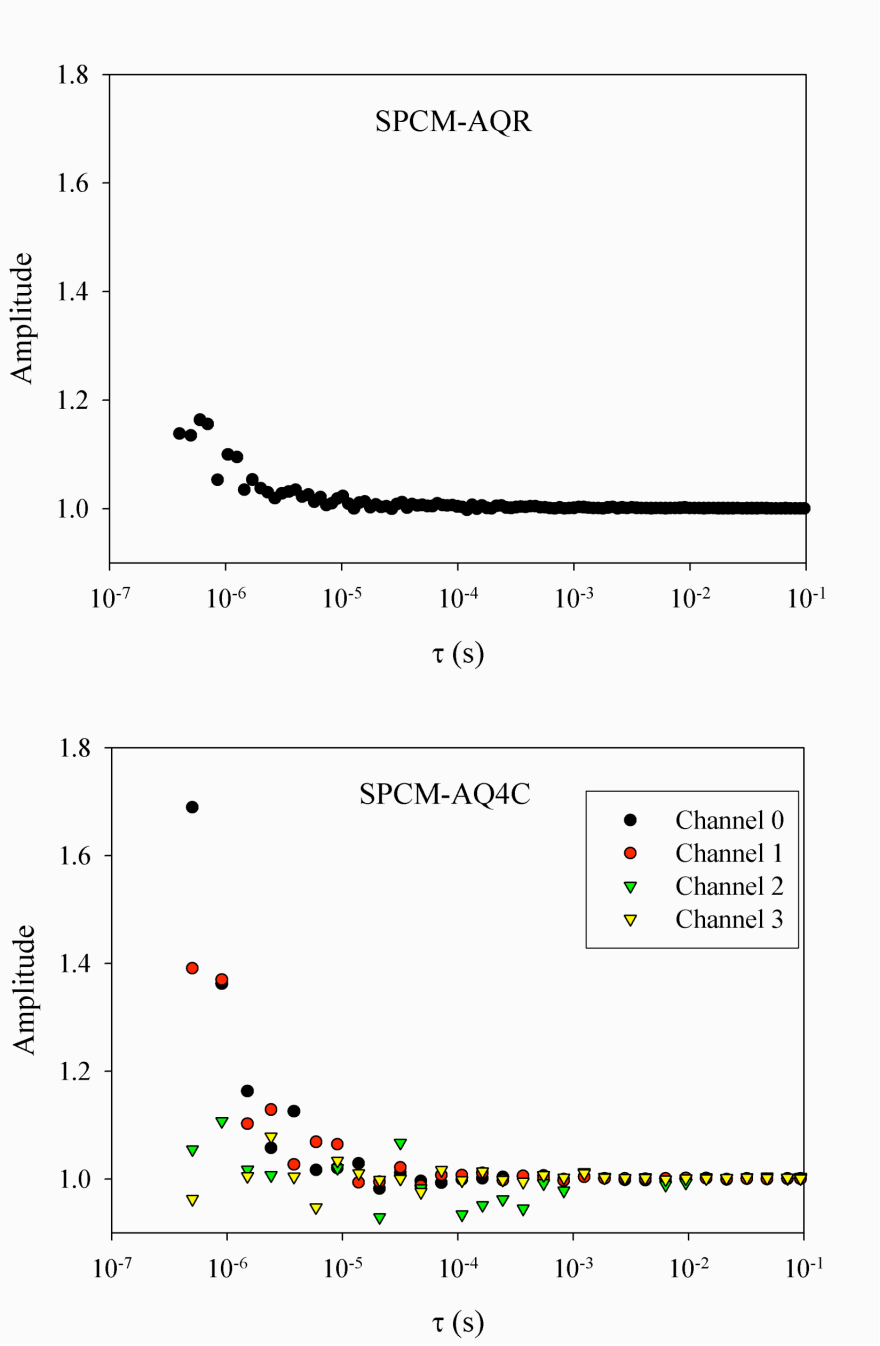


Figure 6.4: Normalized ACF of water. The data was collected with (a) a single-channel SPAD, and (b) the prototype 4-channel SPAD. The peak observed at ~0.5 μs is due to detector afterpulsing.

afterpulsing causes a peak to appear at short times (< 1 μs), the area of which indicates the probability of afterpulsing. In two of the channels of the prototype device the afterpulsing was actually higher than that of the single-channel model. A summary of the specifications for each module is presented in Table 6.1.

As seen in Table 6.1, the dark count rate, i.e. the count rate that occurs with no light incident on the detector, for the four-channel module is at the upper extreme of the range of dark count rates for the single-channel module. The single-channel unit can be purchased with a specified dark count rate, from 25 to 500 counts/s with lower rates more expensive, while the four-channel module is currently only available with a dark count rate of 500 counts/s. The mean dark count rate for three of the four channels of the prototype module were <400 counts / s, while for the fourth channel the mean dark count rate was ~600 counts / s. Although background signal, which includes dark noise, can be corrected for in FCS, this can cause problems in SMD experiments.

## 6.3. Timing Shift with Increasing Count Rate

Figures 6.5 and 6.6 show the time spectra obtained with the TimeHarp 200 card for two of the four-channels with various fluorescence-count rates. From these it can be seen that with increasing count rate the four-channel module exhibits a timing shift on the order of hundreds of picoseconds. This timing shift can cause problems, especially with application of time-gating to eliminate promptly scattered light.

Table 6.1: Comparison of the manufacturers specifications for the 4-channel SPAD (SPCM-AQ4C) and single channel SPAD (SPCM-AQR).

| | **SPCM-AQ4C** | **SPCM-AQR** |
|---|---|---|
| **Dead Time** | **50 ns** | **35 ns** |
| **Afterpulsing Probability** | **0.2 %** | **0.5 %** |
| **Maximum Count Rate** | **$2 \times 10^6$ $s^{-1}$** | **$10^7$ $s^{-1}$** |
| **Dark Count Rate** | **500 $s^{-1}$** | **25-500 $s^{-1}$** |

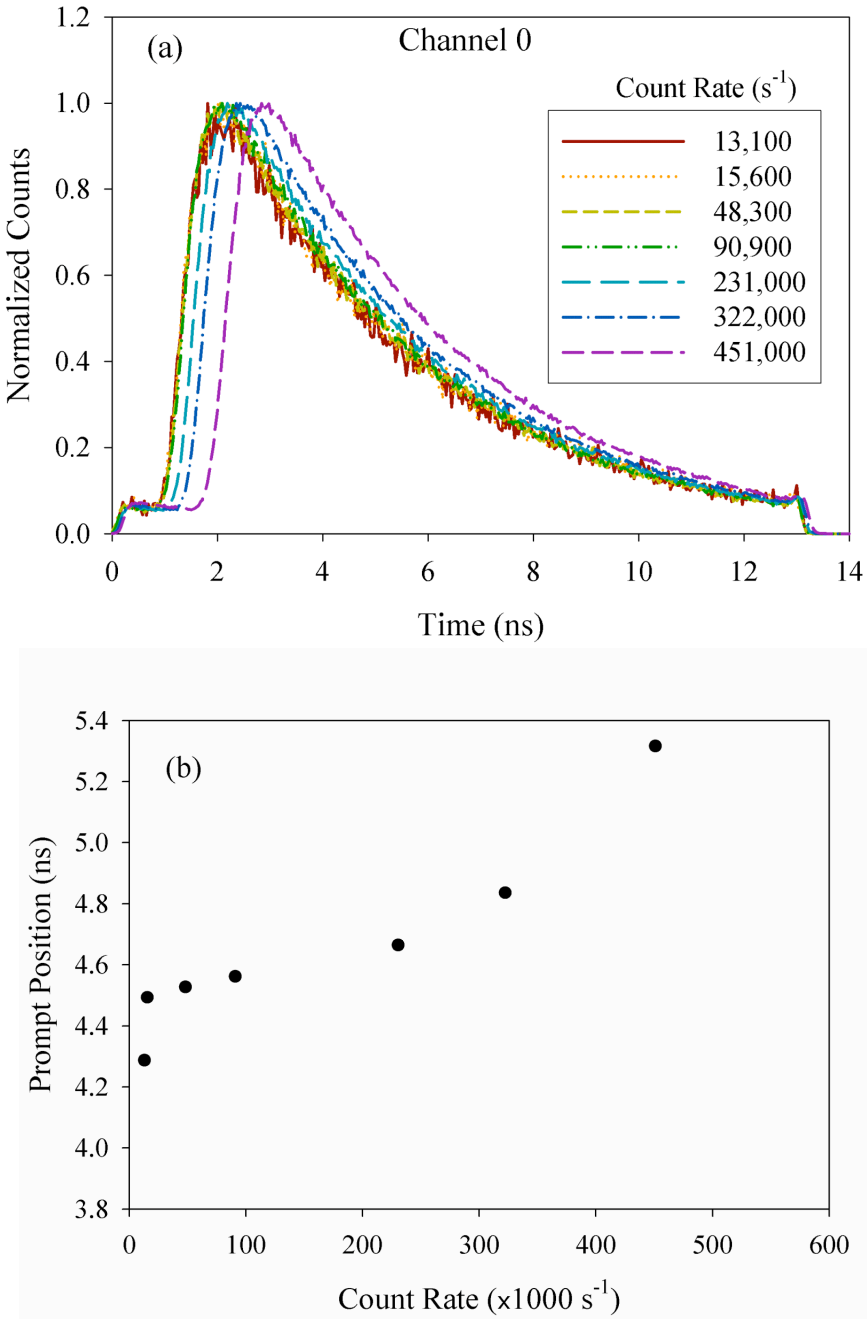


Figure 6.5: Fluorescence lifetime measurement for Channel 0 with increasing count rate. (a) Time-resolved count rate, (b) prompt peak position vs. count rate from (a) which demonstrate the timing shift that occurs.

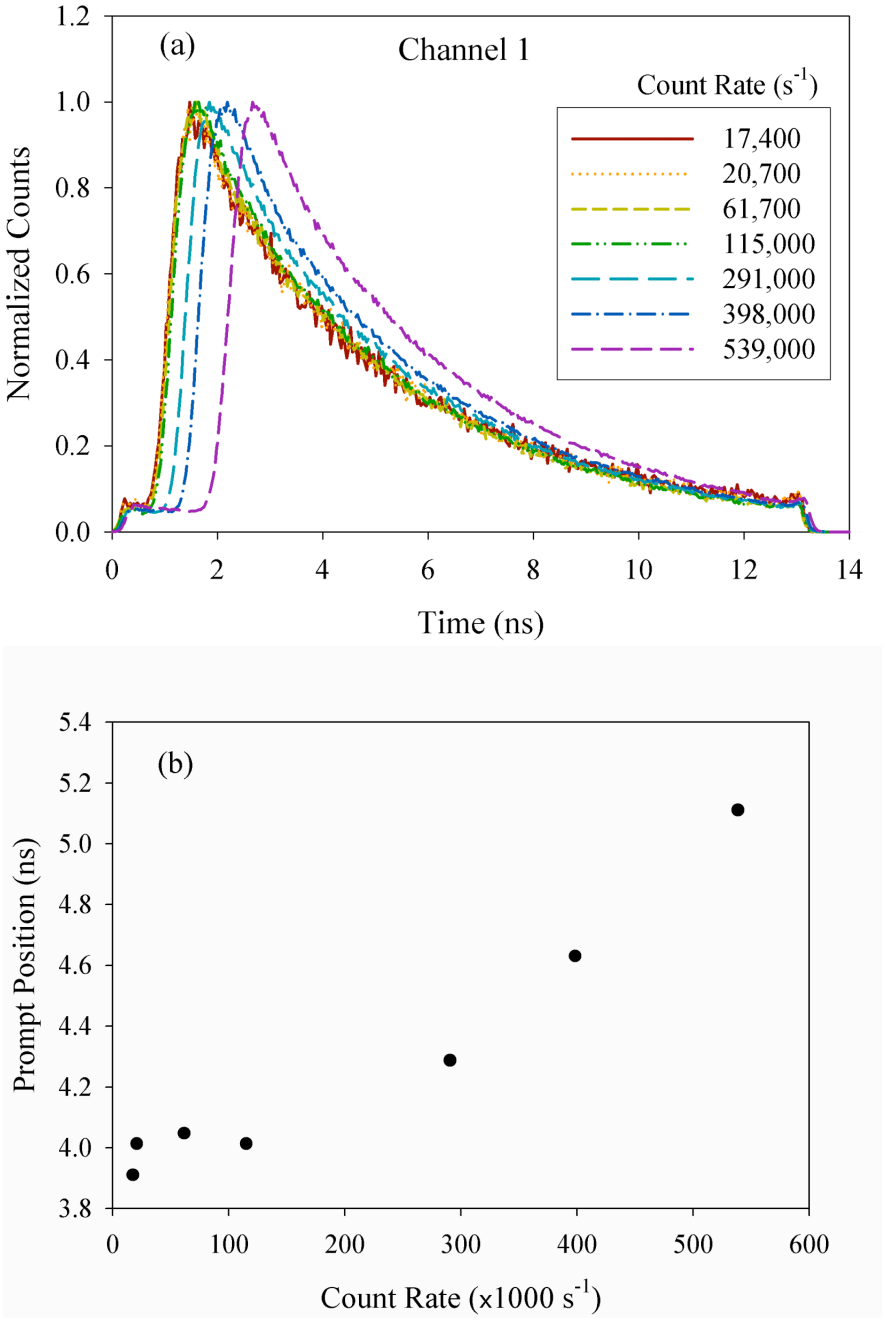


Figure 6.6: Fluorescence lifetime measurement for Channel 1 with increasing count rate. (a) Time-resolved count rate, (b) prompt peak position vs. count rate from (a) which demonstrate the timing shift that occurs.

## 6.4. Summary of Characteristics

The Perkin-Elmer SPCM-AQ4C, used in conjunction with the PicoQuant TimeHarp 200, provides a cost-effective solution for multi-channel time-resolved single-photon fluorescence detection. However, the prototype detector exhibited several shortcomings compared to its single-channel counterpart. For one, the dark count rate for the four channels is higher that of selected one-channel SPCMs. This high dark noise may be unacceptable for SMD investigations. The detector afterpulsing for two of the four channels was also problematic, even though afterpulsing probability for the SPCM-AQ4C is specified to be lower than that of the SPCM-AQR. The four-channel module also exhibits a timing shift of hundreds of picoseconds with increasing count rates.

Despite these problems, by calibration of the system prior to measurements, and by use of data correction techniques, the SPCM-AQ4C should prove to be useful for four-channel confocal time-resolved fluorescence detection, and enable simultaneous measurement of diagnostics, such as FCS, fluorescence polarization, and fluorescence lifetime.

# Chapter 7

# Results of Single-Molecule Detection with Flow

Experiments were conducted with and without flow by use of both OPE and TPE with the experimental setup described in Chapter 5. The fluorescent samples were chosen based on their absorption and emission spectra for compatibility with the available spectral filters and laser sources, and included Alexa Fluor 594, and Alexa Fluor 610 for OPE studies, and Rhodamine B, and Quantum Dots for TPE investigations.

The experiments included studies to determine the sources of background (Section 7.1), investigations to determine the best species for use with TPE (Section 7.3.1), characterizations of the flow system with both OPE (Section 7.2) and TPE (Section 7.3.2), and an attempt to distinguish different solution components by means of fluorescence fluctuation spectroscopies other than FCS (Section 7.2). Conclusions are drawn in Section 7.4, and suggestions for further experiments are outlined in Section 7.5.

## 7.1. Background Characterization

Initial experiments were conducted to characterize the background and reduce it as much as possible. One potential cause of background is the autofluorescence of the glass

capillaries. To study the extent to which the spatial filter of the confocal microscope can discriminate autofluorescence background originating from the tip of the capillary, the count rate was observed as a function of distance between the tip and the center of the probe volume, with only water as a sample. Results for the total count rate with a 5 μm capillary and a 150 μm confocal pinhole are shown in Figure 7.1a, while the total count rate results with a 10 μm capillary and a 75 μm confocal pinhole are shown in Figure 7.1b.

Time-resolved measurements were also performed with water and the capillary tip located at various distances from the laser focus, as shown in Figure 7.2, in order to determine the relative background contributions from autofluorescence and specular scatter from the tip that gets through the interference filter. Glass autofluorescence is identified in Figure 7.2 as the slowly decaying component that diminishes with increasing distance between the tip and the laser focus, while the scattered light causes the peak at ~1.5 ns, and remains constant regardless of the separation between the tip and the laser focus. In order to reduce this background contribution in Figure 7.2, which is attributed to scattered light from the capillary tip, the laser beam was reflected from a Raman notch filter (Kaiser Optical Systems, Inc., HNPF-585-1.0) before it entered the microscope. The Raman notch filter was angle-tuned in order to filter the broadband fluorescence from the laser dye. For both a 5 μm capillary with a 150 μm pinhole, and a 10 μm capillary with a 75 μm pinhole, almost all of the autofluorescence contribution to the background can be eliminated by the spatial filter when the probe volume is 50 μm from the capillary tip.

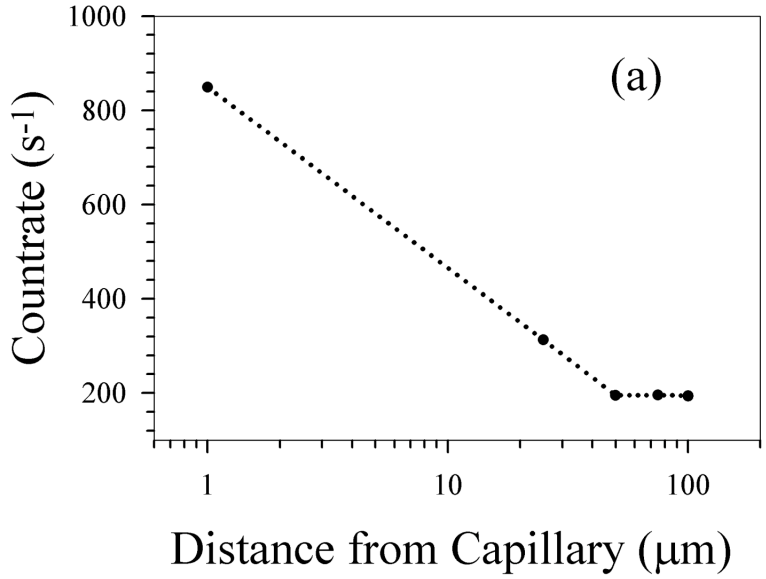


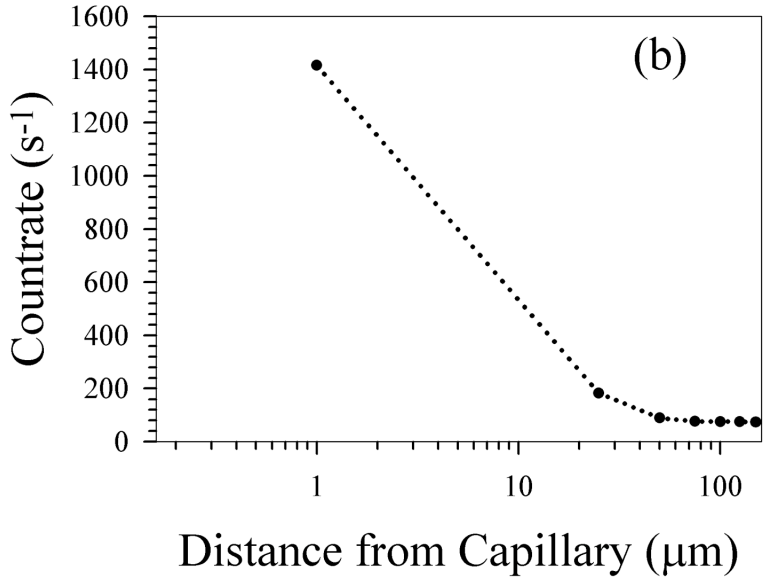


Figure 7.1: Background signal from water at various distances from the capillary. The measurements were performed with (a) a 5 μm capillary, with a 150 μm pinhole, laser power = 30 μW, λ = 585 nm, and (b) 10 μm capillary, with a 75 μm pinhole, laser power = 30 μW, λ = 585 nm.

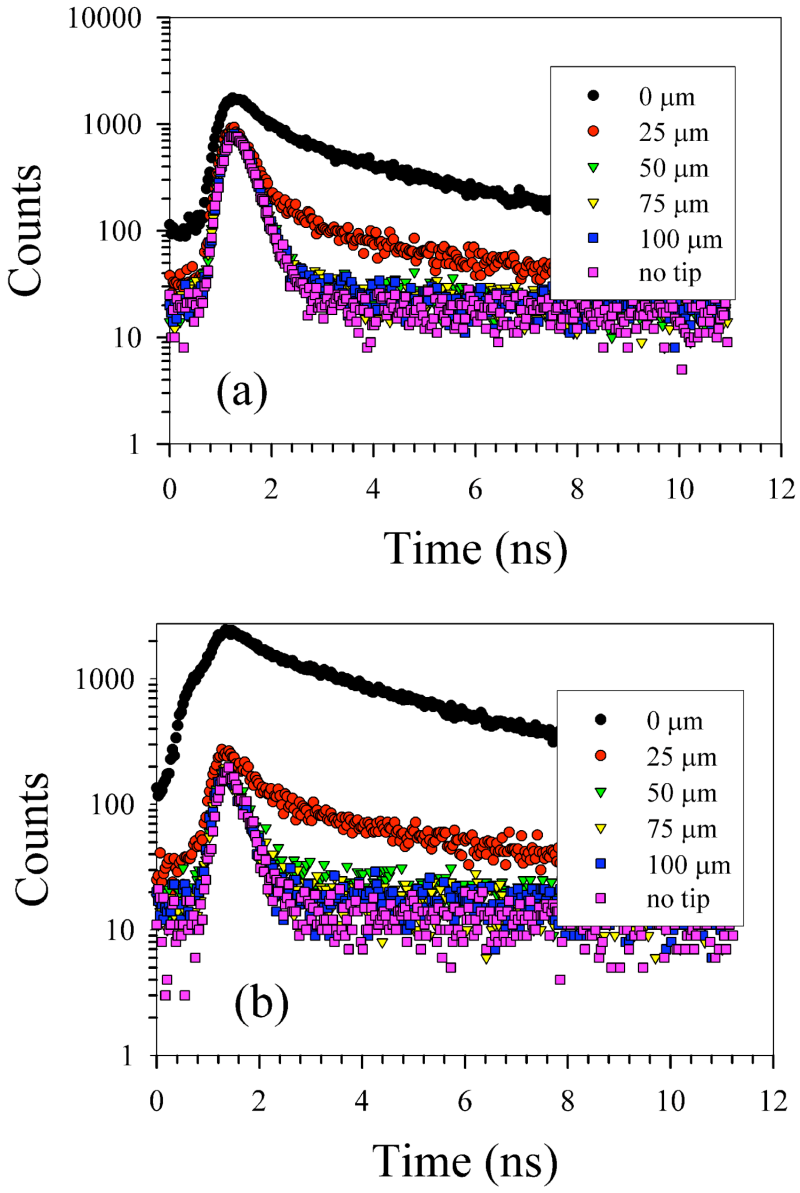


Figure 7.2: Time-resolved count rate with water and capillary at various distances. The measurements were performed with (a) a 5 μm capillary, with a 150 μm pinhole, laser power = 30 μW, λ = 585 nm, and (b) 10 μm capillary, with a 75 μm pinhole, laser power = 30 μW, λ = 585 nm.

Investigations with fused-silica capillaries were also conducted. The specular scatter from the capillary tip was still present with the fused-silica capillaries, but unlike the glass capillaries, fused silica exhibited no discernible autofluorescence even when positioned at the laser focus, which resulted in a lower background. However, the production of micron-sized fused silica capillaries requires the use of a $CO_2$ laser, which results in a cost increase of a factor of ~5 compared to glass capillaries.

## 7.2. One-Photon Excitation with Flow

Figure 7.3a shows the normalized ACF of Alexa Fluor 594 carboxylic acid, succinimidyl ester (Invitrogen, A-20004) (molecular weight = 819.9) as a function of capillary distance from the laser focus. Also shown is the ACF obtained with only diffusional transport, which is used to find the confocal parameter $\chi$ (0.021) and mean diffusional residence time $\tau_D$ (2.1 ms), for the given configuration. By use of Eqn. 3.13 to obtain a least squares fit of this data, it is seen that the flow times increase with increasing distance from the tip. From Eqn. 3.4, it can be seen that the lower amplitude of the ACF obtained with the tip at the laser focus is caused by the higher background signal, which is attributed to glass autofluorescence.

In order to determine the flow velocity from the flow time, the probe volume must first be characterized by use of a standard fluorescent dye that has a known diffusion coefficient. The Alexa Fluor 594 used here has a measured diffusion coefficient of 6.5 $\times 10^{-7}$ $cm^2/s$ [76]. This diffusion coefficient, and the fitted parameters of the mean diffusional residence time, $\tau_D$, and confocal parameter, were used to calculate the radius

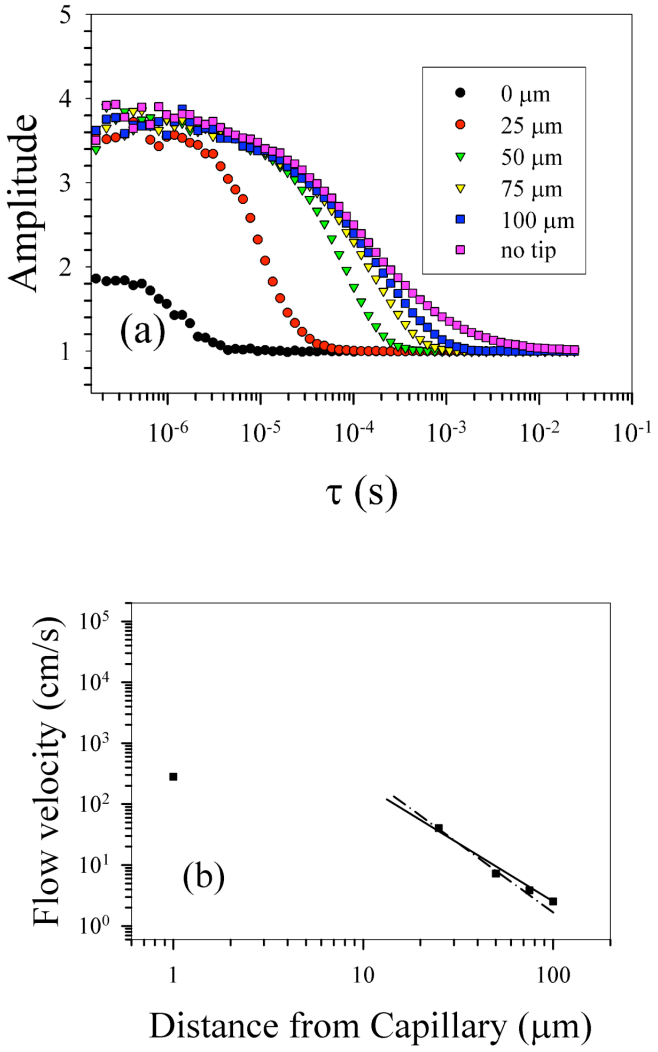


Figure 7.3: Characterization of the flow with FCS by use of OPE. (a) Normalized ACF for 50 pM Alexa Fluor 594 in 0.1 % Tween 20 at various distances from the 5 µm capillary, with a 150 µm pinhole, P = 30 µW, λ = 585 nm. (b) The calculated flow velocities at these distances by use of the parameters obtained with Eqn. 3.13, along with the fit to the last 4 points (solid line). A slope of 2 is also shown for comparison (dashed line).

of the confocal volume in the *x*-*y* plane, $\omega_0 = 0.738 \pm 0.03$ μm, and the radius in the *z*-direction, $z_0 = 5.05 \pm 0.52$ μm. The errors are estimated by adjustment of $\omega_0$ to fit the curve after the confocal parameter is forced to take on sub-optimal values. The flow speed, $v_F$, can then be determined by the curve-fit of the ACFs with flow by use of Eqns. 3.11 and 3.12. The plot of flow velocity versus distance from the tip is shown in Figure 7.3b. This is expected to decrease approximately quadratically with increasing distance, and in fact, the least-square fit with the first point excluded has a slope of -2.32 in the log-log plot. For visual reference, a slope of -2 is also plotted in the figure.

The main reason flow is desired is to increase the rate, *M*, at which molecules pass through the probe volume which can be calculated from the parameters extracted from the curve-fit of the ACF. For the case without flow this is given by $M_{diffusion}=N / 2\tau_D$, and is measured to be 85 molecules/second. On the other hand, with flow, $M_{flow} = N / 2\tau_F$, and works out to be 2626 molecules/second with the capillary 50 μm from the laser focus.

The axial flow causes the molecules to traverse the major axis of the 3D Gaussian ellipsoid, which results in more collected photons per molecule than would occur if the same flow speed transverse to the optical axis were used. Also, the mean count rate was measured, and divided by the mean number of molecules in the probe volume obtained from the ACF, which results in a mean count rate per molecule of 18,274 and 18,184 counts · molecule$^{-1}$ · second$^{-1}$, for the cases with and without flow, respectively. This means that although the rate of molecules passing through the probe volume is greater with flow than without, the mean rate of photons during each photon burst remains essentially the same, within the error of the measurement. The count rate versus time is

plotted in Figure 7.4 for the case where the capillary is 50 μm above the laser focus. Each burst corresponds to an individual chromophore, but as each dye molecule travels through a different part of the radial laser profile, the burst amplitudes vary.

One problem that was encountered was the adsorption of fluorophores to the glass surface of the capillary. This resulted in the background signal increasing over time, but can be alleviated with the addition of detergents, such as Tween 20 [22], which is often used in high-throughput screening assays. Figure 7.5 illustrates the difference the detergent makes with the amplitude of the normalized ACF when the capillary is positioned at the laser focus.

## 7.3. Two-component Fluorescence Brightness Assay with Flow

When transport is dominated by flow, FCS can no longer distinguish molecules with differing translational diffusion. Therefore, other methods based on fluorescence brightness must be used discriminate between the solution components. Here, experiments are described that attempt to differentiate compounds based on fluorescence brightness by use of the S-FFS technique described in Section 3.6.

Two different sets of fluorescently-labeled species were used for this investigation. The first used Biocytin and Streptavidin, both labeled with Alexa Fluor 594 (Invitrogen, A-12922 and S-32356, respectively), which are known to bind together very strongly with a dissociation constant, $k_D$, of $10^{-14}$ M [77]. These were chosen because the strong binding between Biocytin and Streptavidin makes it possible to easily prepare

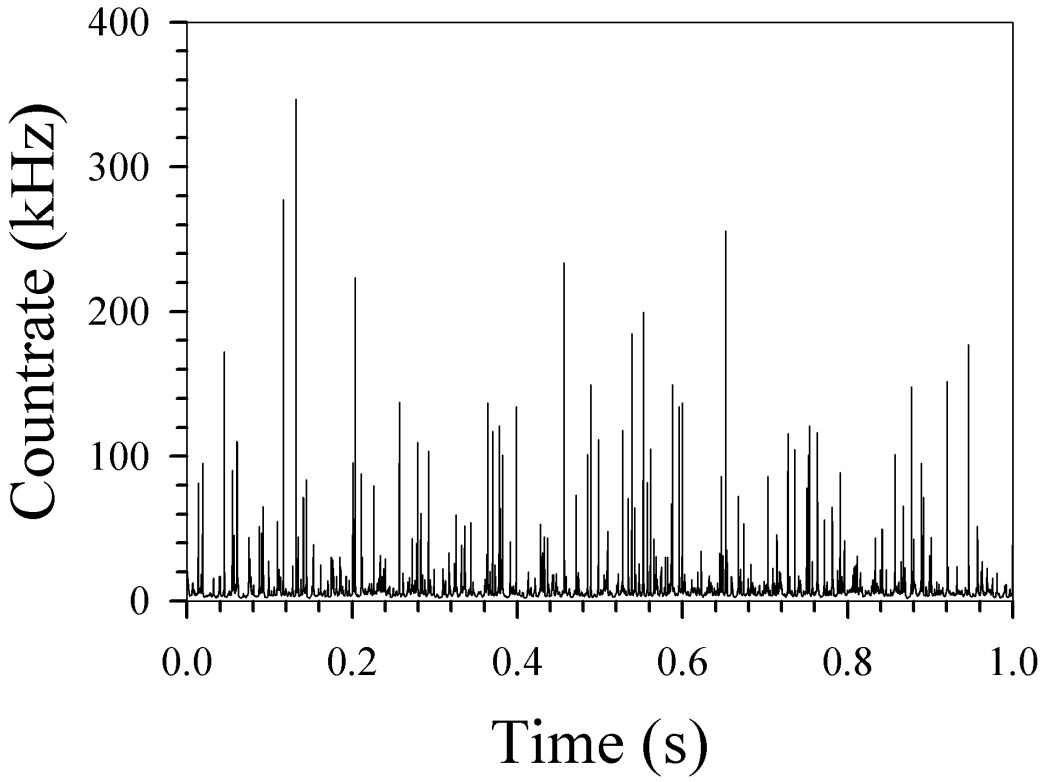


Figure 7.4: Plot of count rate vs. time with flow. The data was obtained with Alexa Fluor 594 at a concentration of 50 pM, with the 5 μm capillary 50 μm from the laser focus, a 150 μm pinhole, laser power = 30 μW, and λ = 585 nm.

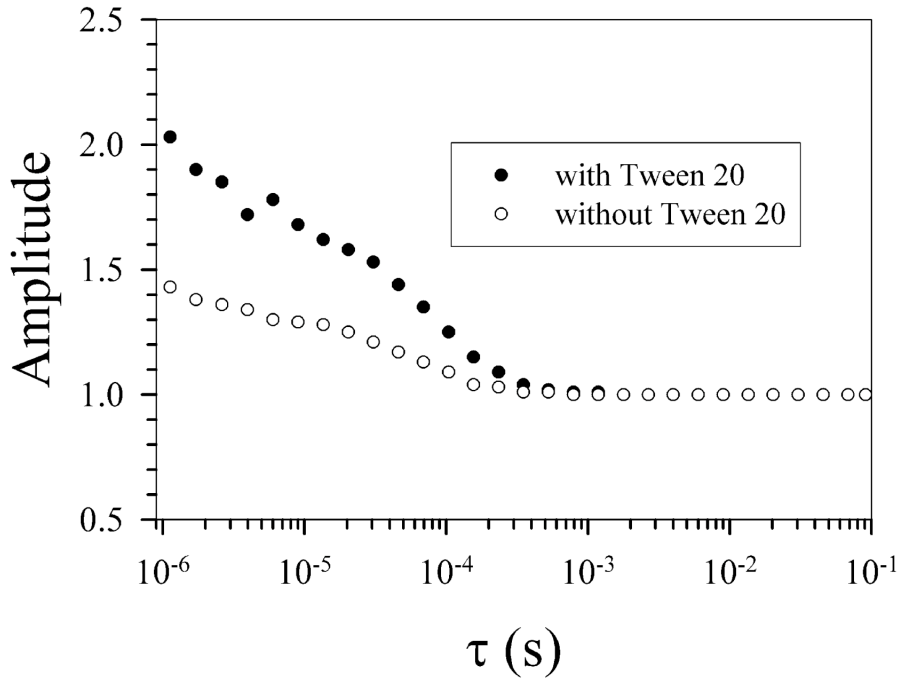


Figure 7.5: Effect of detergent on the ACF amplitude. The lower amplitude without Tween 20 is the result of molecular adsorption to the glass capillary, which causes a higher background, as seen with Eqn. 3.4.

samples with known concentrations of single- and double-labeled biomolecules. Hence they serve as a model system to study binding titrations of unknown proteins, in which the net fluorescence signal does not change with binding, but the number of photon bursts and the mean number of photons per burst do change.

The titration was conducted in an 8-chambered coverglass (Nagle Nunc, 155411) to avoid the need to change slides. The capillary was realigned before each measurement with the use of the camera, as described in Section 4.1, to ensure that the tip was 50 μm from the laser focus. The first point in the titration was obtained with 200 μL of Alexa Fluor 594-Streptavidin conjugate at a concentration of 1 nM. For the second point, 175 μL of Alexa Fluor 594-Streptavidin conjugate at 1 nM was mixed with 25 μL of Alexa Fluor 594-Biocytin conjugate at 1 nM in a new well. Subsequent points were then attained by decreasing the volume of Alexa Fluor 594-Streptavidin by 25 μL, and increasing the volume of Alexa Fluor 594-Biocytin by the same amount. The flow was established by use of a 10 μm capillary positioned 50 μm from the laser focus.

The results of the S-FFS analysis for the mean number of photons per burst with a threshold of 10 for the above-described titration is shown in Figure 7.6a with data collection times of 30 seconds. The expected behavior is shown in Figure 7.6b. The rate of bursts is shown in Figure 7.7a, and the expected trend in Figure 7.7b.

The unexpected results are believed to be caused by several factors. The 10 μm capillary is larger than the diameter of the probe volume in the radial direction by a factor of ~10, and the tip is positioned 50 μm above the laser focus. This configuration results

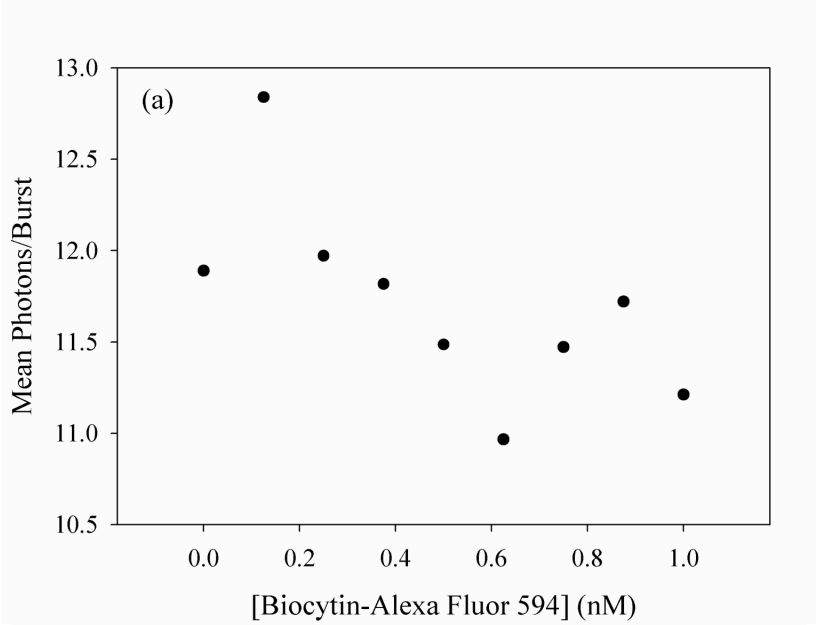


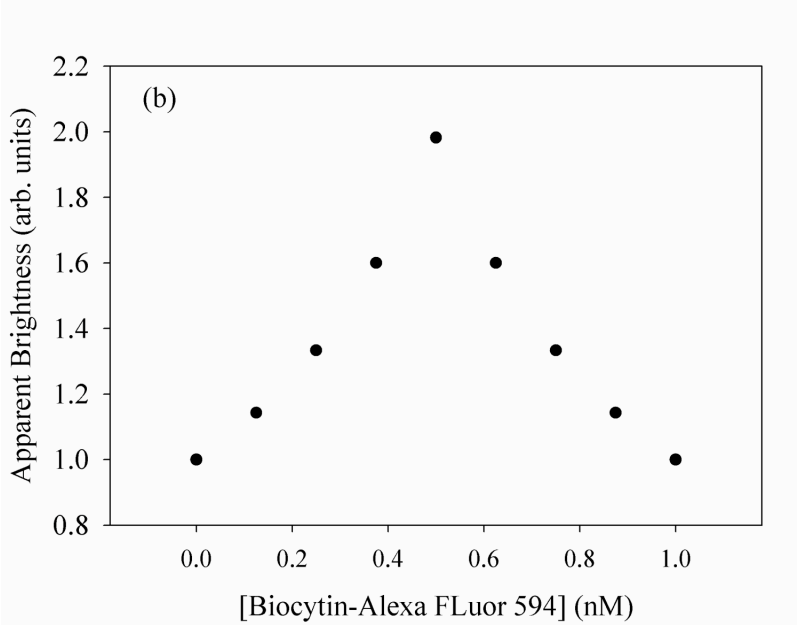


Figure 7.6: S-FFS mean burst amplitude data for OPE. (a) Experimental, and (b) expected for a titration of 1 nM Biocytin-Alexa Fluor 594 conjugate into 1 nM Streptavidin-Alexa Fluor 594 conjugate with $\lambda$ = 585 nm, laser power = 30 μW, and the 10 μm capillary positioned 50 μm from the laser focus.

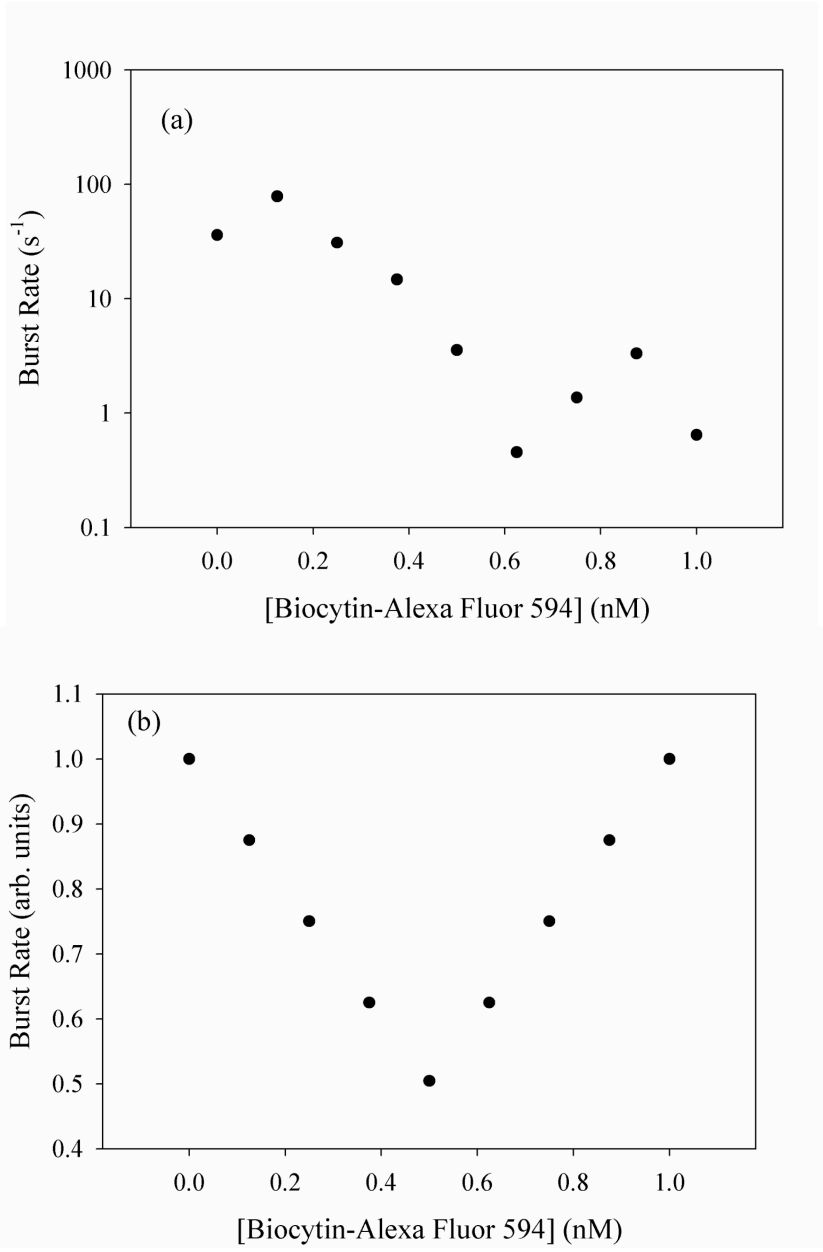


Figure 7.7: S-FFS rate of photon bursts data for OPE. (a) Experimental, and (b) expected for a titration of 1 nM Biocytin-Alexa Fluor 594 conjugate into 1 nM Streptavidin-Alexa Fluor 594 conjugate with $\lambda$ = 585 nm, laser power = 30 μW, and the 10 μm capillary positioned 50 μm from the laser focus.

in fluorescently labeled molecules traversing different regions of the laser profile, and therefore the number of photons per burst fluctuates for each species. The lack of stability of the laser is also a problem. The repositioning of the capillary between the titration measurements could have resulted in changes in flow velocity.

The second attempt that is reported was with a mixture of two fluorophores with different brightness. Before these experiments could be carried out, first it was necessary to find two suitable fluorophores that could each be detected at the single-molecule level and that had count rate per molecule values that differ by a factor of ~2. This was determined first by comparison of the excitation and emission spectra of several fluorescent species, which are shown in Figure 7.8. Possible candidates were then examined further with preliminary FCS experiments performed without flow to determine the mean number of photons per molecule. As is usually done in FCS, this was found by the division of the total experimental photon-counts by the mean number of molecules in the probe volume, which was extracted from the curve-fit of the normalized ACF.

From these investigations, Alexa Fluor 594 and Alexa Fluor 610 were chosen, as the ratio of their count rate per molecule was 1.67 when excited with a wavelength of 585 nm, and observed through the emission filter centered at 617 nm, with a bandwidth if 45 nm (Omega Optical, 617DF45). Plots of the instantaneous count rates for these two molecules are shown in Figure 7.9, which also demonstrates the difference in molecular brightness.

Titrations were then conducted with an applied flow by use of a 10 μm capillary positioned 50 μm above the laser focus. The titration was started by use of 200 μL of

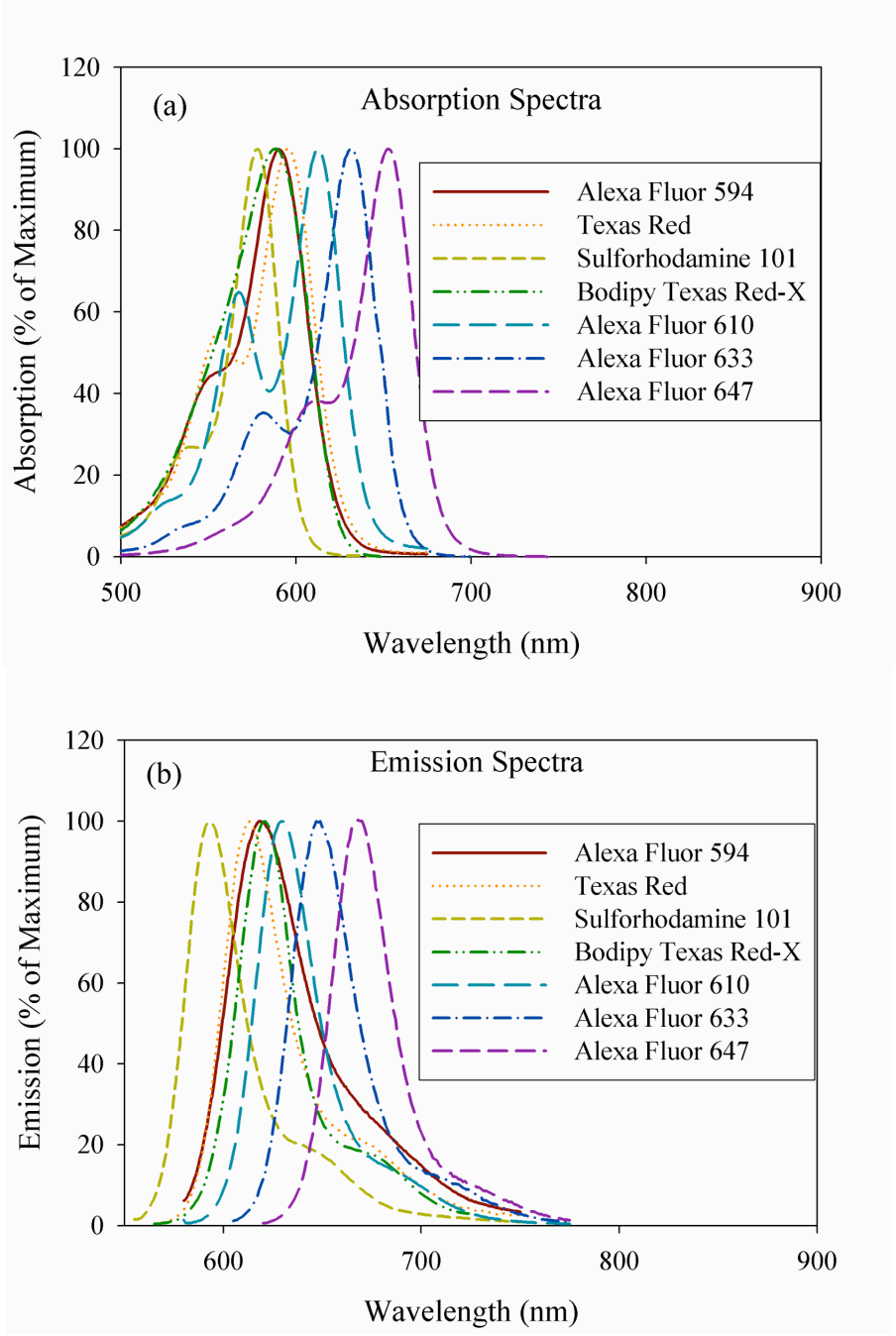


Figure 7.8: Spectra of several organic dyes. (a) Absorption and (b) emission spectra used to initially determine possible candidates for distinguishing fluorophores based on fluorescence brightness.

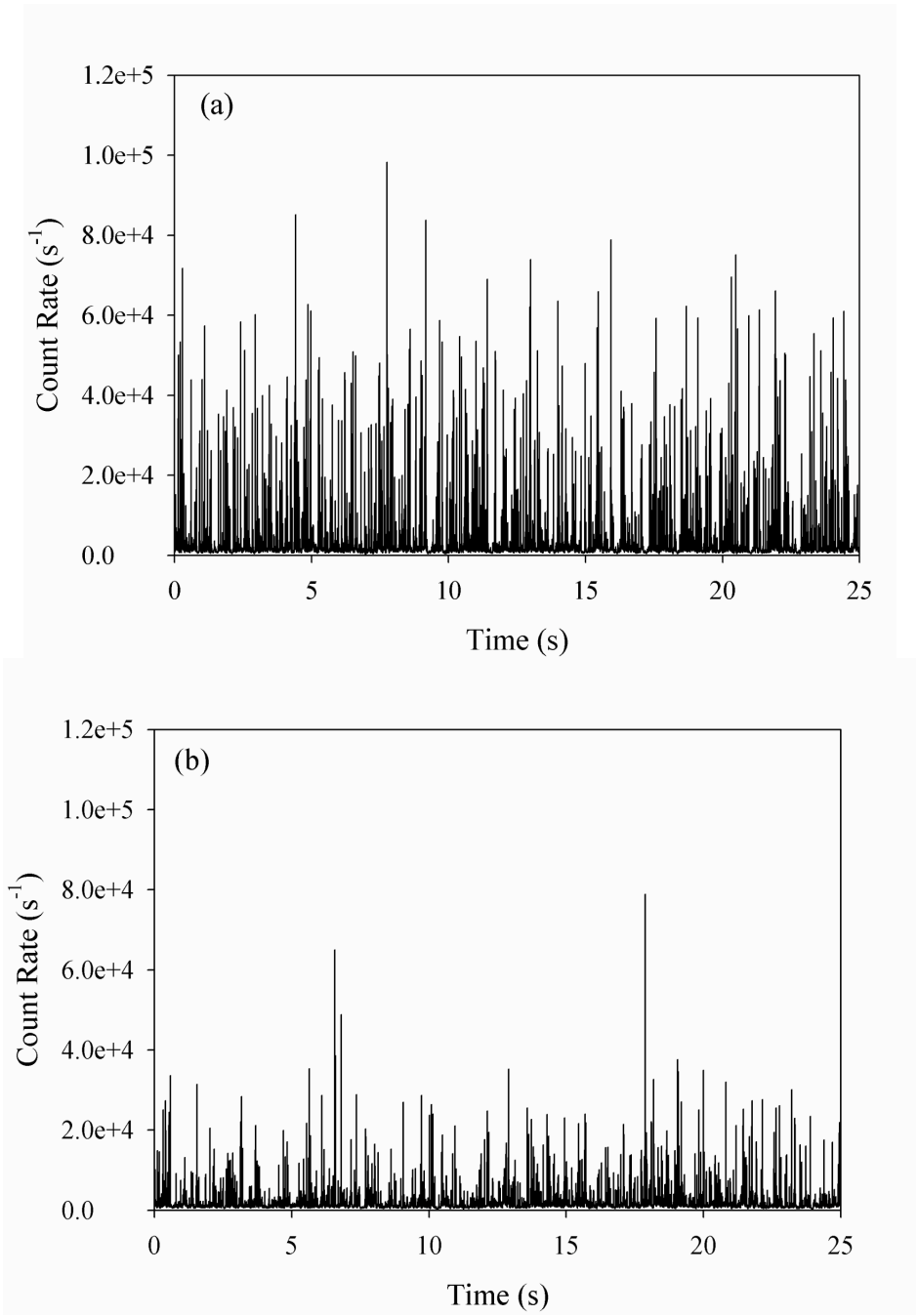


Figure 7.9: Comparison of burst heights without flow. (a) Alexa Fluor 594, and (b) Alexa Fluor 610 excited with a $\lambda$ = 585 nm, and a power of 150 μW.

Alexa Fluor 594 diluted to a concentration of 1nM in water with 0.1% Tween 20 by volume to reduce fluorophore adsorption to the capillary. Aliquots of 50 μL of Alexa Fluor 610, also at 1nM in 0.1% Tween 20, were then added until the total volume was 600 μL. The capillary was not repositioned before each measurement so that the flow velocity should be more consistent than the previous titration. Data were collected at each titration point, and analyzed by use of the technique described in Section 3.6 with a threshold of 16. Results of the data analysis are presented in Figure 7.10 as plots of mean photons per burst and total number of bursts, both versus concentration of the added species.

For both of the described titrations, neither the rate of bursts, nor the mean number of photons per burst behaves as expected. For example, as more Alexa Fluor 610 is added to the solution, the number of photons per burst should monotonically decrease, but in reality this value fluctuates, and does not appear to follow any trend. Both of these results are most likely caused by a ratio of fluorescence brightness that is too low, which causes any possible trend to be lost in the noise. Another problem is again the fact that molecules traverse through different regions of the laser, which causes the count rate per molecule to vary by more than the difference between the two fluorophores. The laser stability may have also caused fluctuations in the mean number of photons per burst.

## 7.4. Two-Photon Excitation

Experiments with TPE were also conducted with several fluorescent species. The initial experiments were to verify that TPE was viable with the previously described system,

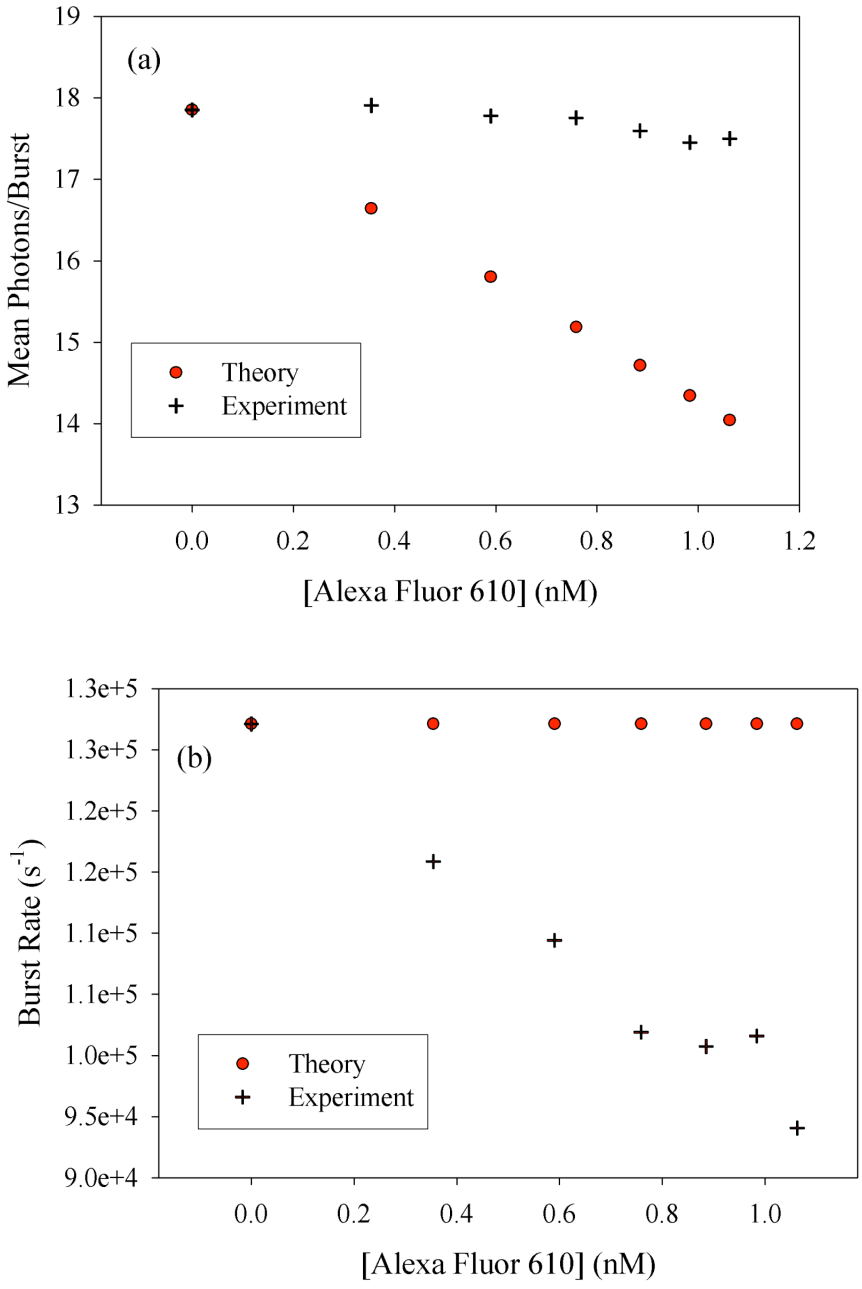


Figure 7.10: S-FFS data for a titration of fluorophores with different brightness. (a) Mean burst amplitude, and (b) burst rate obtained with S-FFS for a titration of 1 nM Alexa Fluor 610 into 1 nM Alexa Fluor 594 with $\lambda$ = 585 nm, laser power = 75 µW, and a 10 µm capillary positioned 50 µm from the laser focus.

and to find a suitable sample for the later studies with flow. The initial experiments without flow will be described in Section 7.4.1, and the characterization of the flow system with the use of TPE is discussed in Section 7.4.2.

### 7.4.1. TPE without Flow

The first fluorescent species that was used to test the system for use with TPE was Rhodamine B, which has a large TPE absorption cross-section with a maximum of 2.1 $\times 10^{-48}$ $cm^4s$/photon at 840 nm [78]. Figure 7.11 presents the experimentally obtained instantaneous count rate versus time, and the normalized ACF for Rhodamine B excited at 840 nm. By inspection of Figure 7.11, it is apparent that the signal to background ratio is rather poor, and that Rhodamine B would not be a good candidate for the experiments with active transport. Rhodamine B did prove useful for the characterization of the probe volume, as it has a known diffusion coefficient of $3.6 \times 10^{-6}$ $cm^2/s$ [79]. This was used along with curve fitting by use of Eqn. 3.4 to extract the radii of the confocal volume in the *x*-*y* plane, and the *z*-direction, which were 0.468 μm and 2.98 μm, respectively.

The next species investigated was a solution of Qdot 585 nanocrystals conjugated with streptavidin (Invitrogen, Q10121MP) (~20 nm in size), which has a broad TPE spectrum [80], and has a higher fluorescence quantum yield compared to organic dyes. The instantaneous count rate versus time, and the normalized ACF for the Qdot 585-streptavidin conjugate are shown in Figure 7.12, which both demonstrate the much improved signal to noise ratio compared to Rhodamine B. Another advantage of the use of the Qdot 585-streptavidin conjugate is that these large structures have slow diffusion

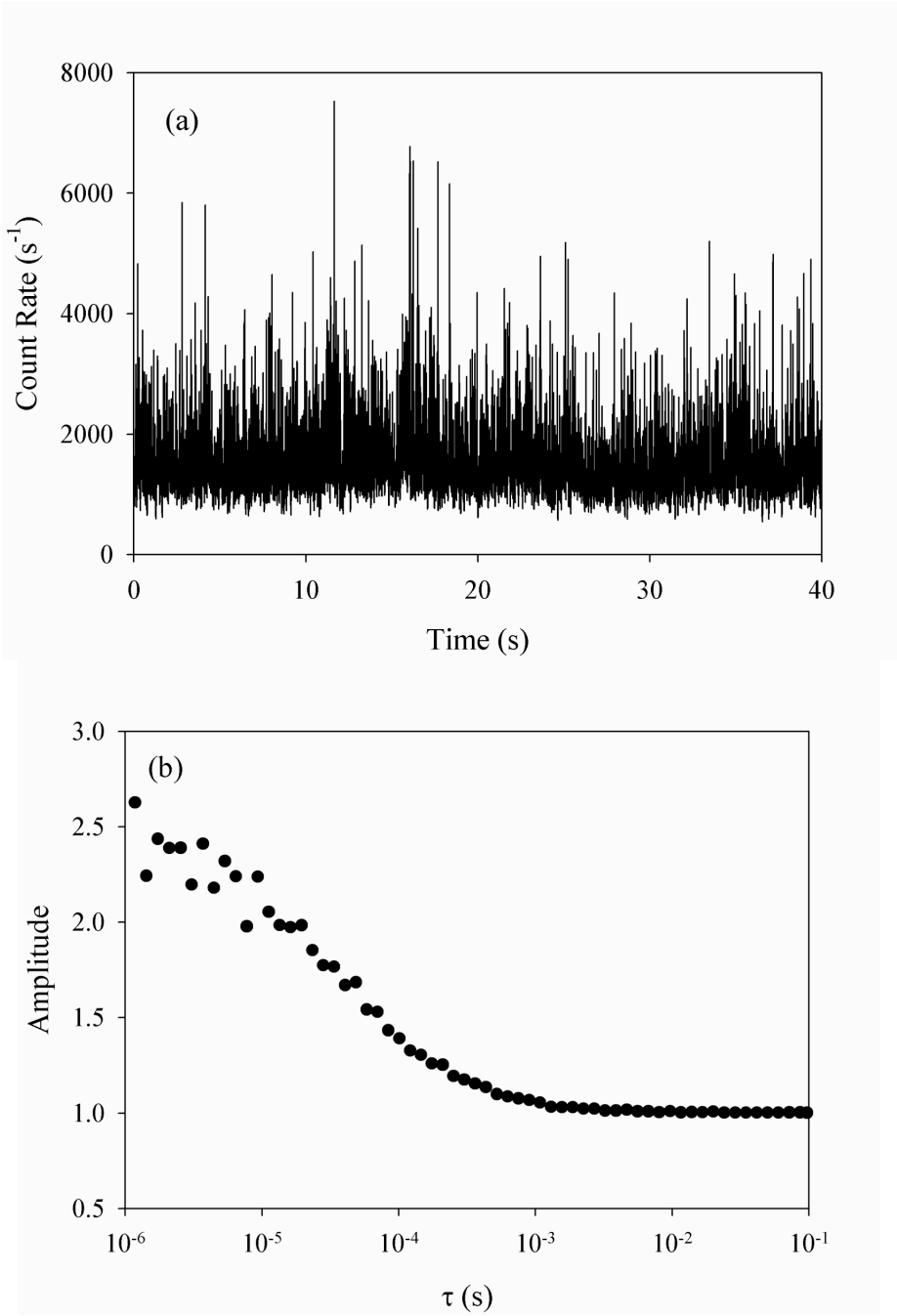


Figure 7.11: Results of preliminary studies of Rhodamine B by use of TPE. (a) Count rate vs. time, and (b) normalized ACF when excited at 840 nm, laser power = 1mW.

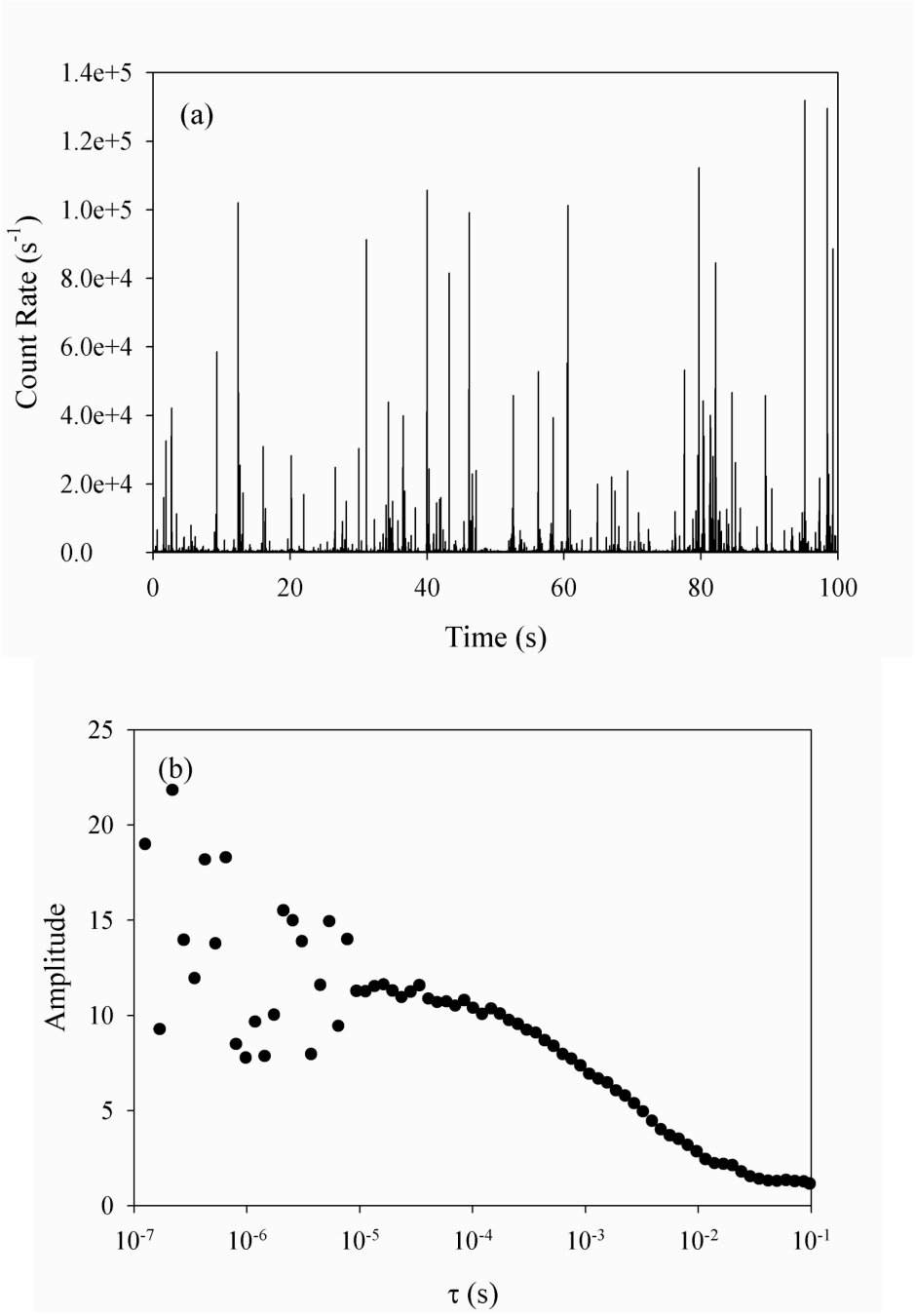


Figure 7.12: Results of preliminary studies of Qdot 585-Streptavidin conjugate by use of TPE. (a) Count rate versus time, and (b) normalized ACF when excited at 790 nm, laser power = 3mW.

coefficients, which means that the flow velocity that is necessary to dominate diffusion is reduced. With the use of the fitting parameters determined with Rhodamine B, the diffusion coefficient of the Qdot 585-streptavidin conjugate was found to be $3.2\times10^{-8}$ $cm^2/s$.

### 7.4.2. TPE with Flow

After the Qdot 585-streptavidin conjugate was chosen as the fluorescent species for the investigation of TPE with an applied flow, the next step was to examine the background due to glass autofluorescence under experimental conditions. This was once again accomplished by measurement of the time-resolved count rate with water with and without the capillary, the results of which are shown in Figure 7.13. The dip near the origin in Figure 7.13 is an artifact from the time-resolved photon detection system. Unlike with OPE, the background due to autofluorescence is not seen with TPE with the capillary at the laser focus.

The normalized ACF with the capillary at various distances from the laser focus is shown in Figure 7.14. These were then curve fit by use of Eqn. 3.13 in order to find the residence times due to flow, and in turn the flow velocities, which are plotted in Figure 7.15. The least-squares fit with an adjustable exponent, and a line that is the square of the capillary distance is also plotted in Figure 7.15. There was again an improvement in the rate of passage of molecules, with an increase from 1.80 molecules/second without the applied flow to 220 molecules/second with flow and the capillary positioned 50 μm from the laser focus. The count rate per molecule also behaved similarly to that observed with

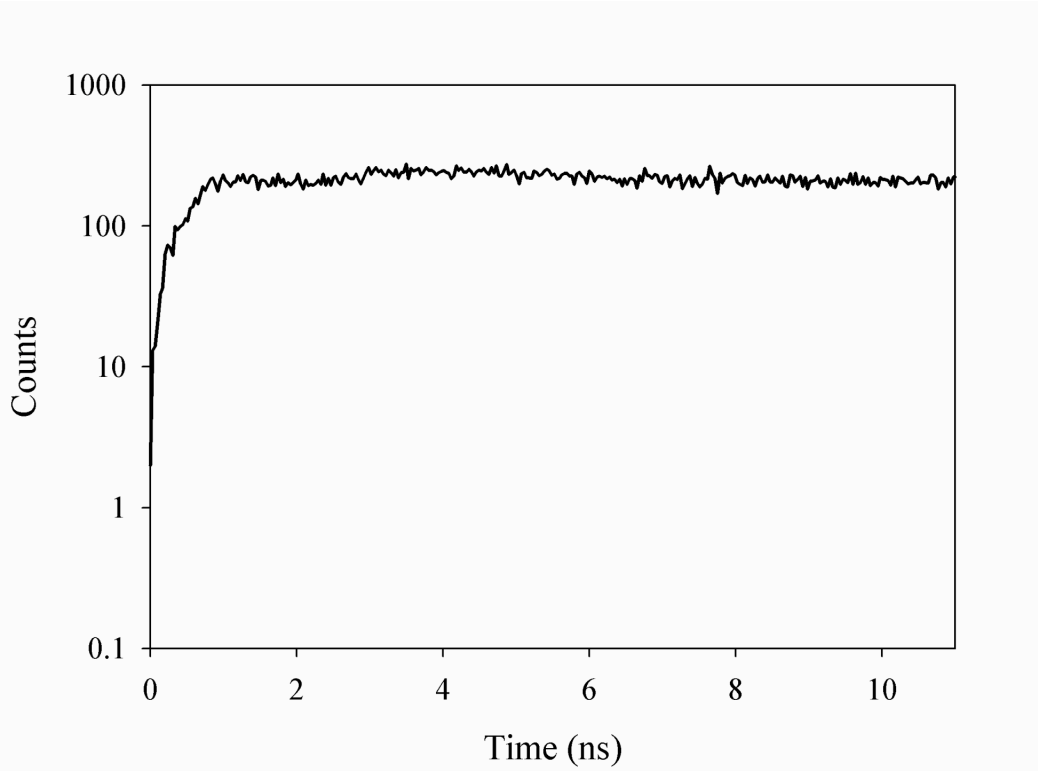


Figure 7.13: Time-resolved count rate with TPE. The measurement was performed with water and a 10 μm capillary positioned at the laser focus with laser power = 3 mW, and λ = 790 nm.

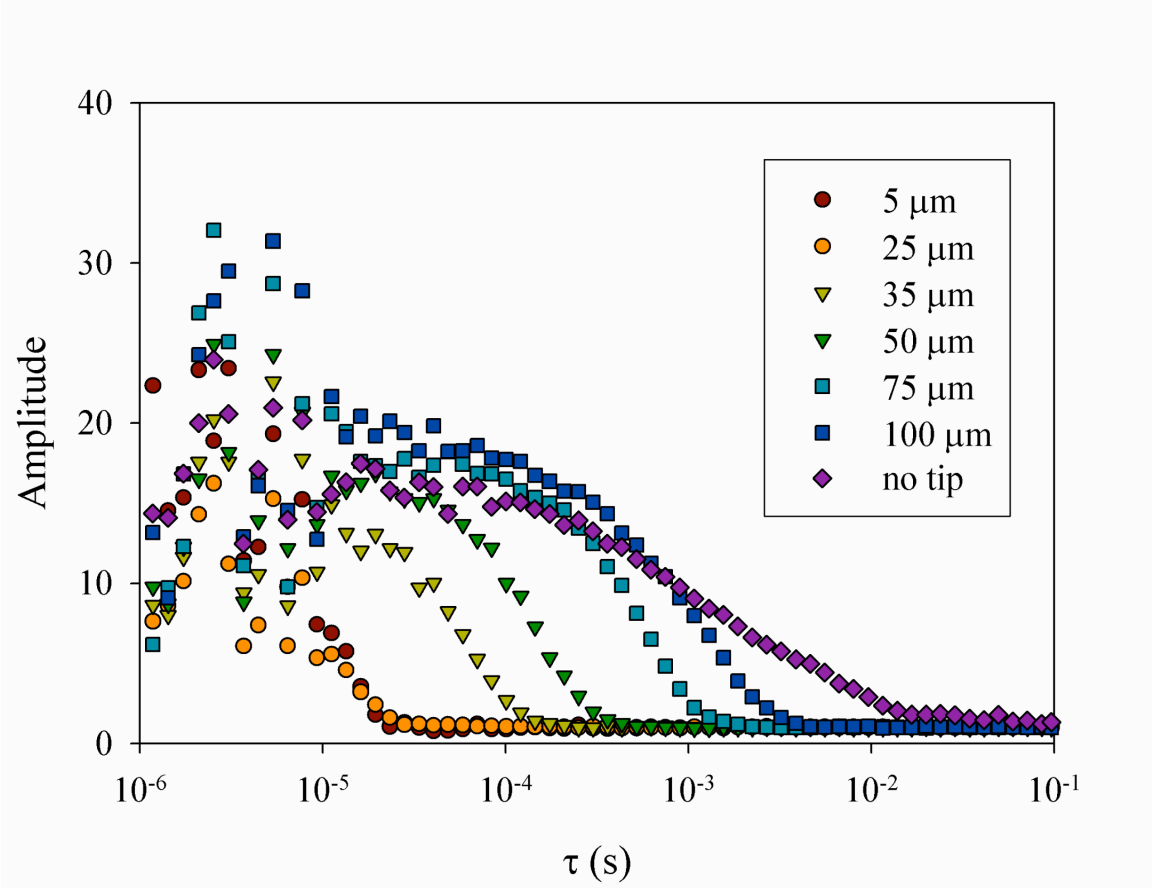


Figure 7.14: Characterization of flow with FCS by use of TPE. Normalized ACF for 2 nM Qdot 585-Streptavidin conjugate at various distances from the 10 µm capillary, with a 150 µm pinhole, laser power = 3 mW, and λ = 790 nm.

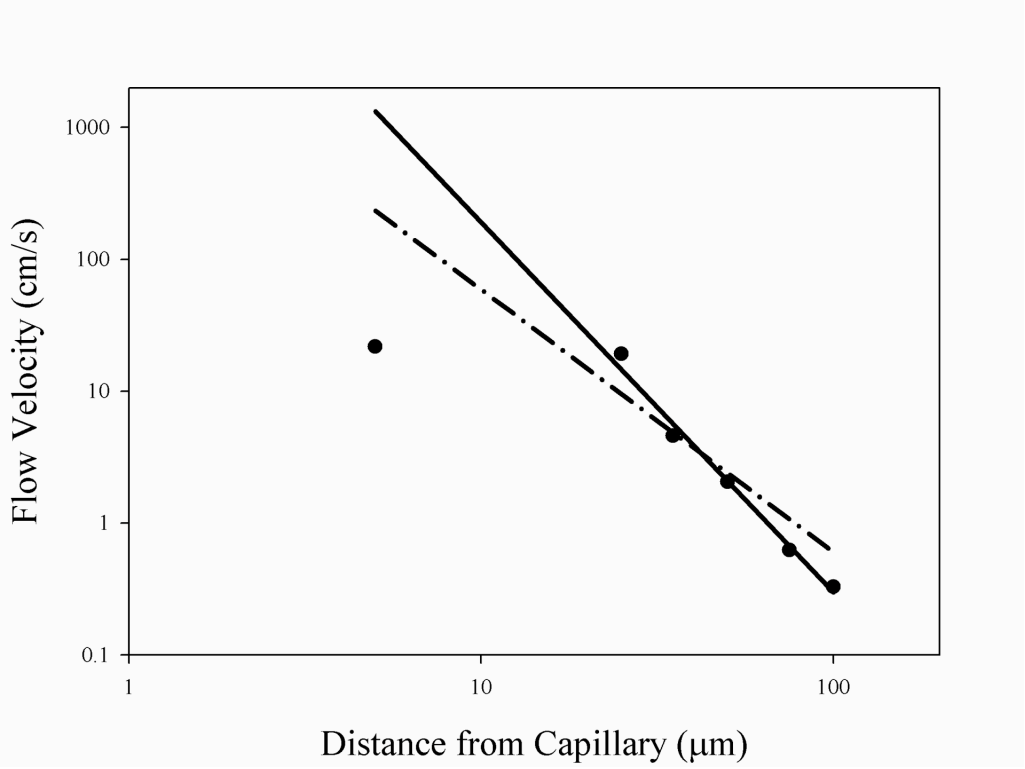


Figure 7.15: Calculated flow velocities at the distances shown in Figure 7.14. Values are calculated by the use of the parameters obtained with Eqn. 3.13, along with fit to the last 4 points (solid line). A slope of 2 is also shown for comparison (dashed line).

OPE, which remained relatively constant with values of 4917 and 5122 counts · molecule$^{-1}$ · s$^{-1}$, without and with active transport, respectively.

## 7.5. Conclusions

The use of pressure-driven flow in SMD experiments is of interest in applications such as pharmaceutical drug discovery, where it is desired to more rapidly process large, slowly diffusing bio-molecules. The use of FFS techniques to distinguish different species based on fluorescence brightness with the use of a single detector proved difficult. However, with the use of multi-channel FFS, it should be possible to determine binding affinities of labeled protein-ligand complexes.

Axial flow has the advantage of the molecules being transported along the major axis of the 3D-Gaussian ellipsoid, which results in more collected photons compared to transverse flow. Here, the count rate per molecule with flow was comparable to the case without flow, which were both measured to be ~18,000 molecule$^{-1}$ · s$^{-1}$, while the rate of molecules passing through the probe volume increased by a factor of ~100 for slowly diffusing proteins .

In this work, fluorophores are sucked through the probe volume by the application of a negative pressure to either a 5 or 10 μm capillary that is oriented along the optical axis. FCS with both OPE and TPE was used to characterize the flow with this new geometry. The flow velocity was shown to decrease approximately quadratically with increasing distance from the capillary opening. A maximum measured flow velocity of ~3 m/s was achieved with the 5 μm capillary located at the laser focus and a manometer head of ~110 cm of water.

For OPE, there is a tradeoff with this configuration between the background autofluorescence of glass near the tip and the decrease in flow velocity as the distance increases. However, when the tip is positioned >50 μm from the laser focus, the background can be spatially filtered while the flow speed is adequate to dominate Brownian diffusion. There was also the problem with fluorophore adsorption to the glass, but much like previous work, this was alleviated with the use of detergents.

The glass autofluorescence is not present for measurements with TPE. However, conventional organic dye molecules are not easily detected with this form of excitation, because of the small number of photons per molecule. There are alternatives, which include Qdot conjugates, which have a much larger brightness, and these make SMD by use of TPE with active transport easily possible.

## 7.6. Suggestions for Future Work

SMD with active transport should prove to be an important tool for biological studies, such as pharmaceutical drug discovery. Both OPE and TPE have been shown to be simple to set up, and effective at increasing the rate of passage of molecules through the probe volume. However, there are some parts of this study that could be extended in future investigations.

The work described here was limited to the use of a single detector, which restricted the techniques that could be used to determine the fraction of free and bound fluorophores. By extension to multiple detectors, more techniques would be available to improve the ability to distinguish between free and bound species. For example, with a

second detector the fluorescence polarization anisotropy could be measured, which would allow changes in rotational diffusion that result from binding.

The use of TPE also holds promise because of the absence of any background, most noticeably that caused by glass autofluorescence. This would allow a much smaller capillary to be used, and positioned at the laser focus. If the capillary opening were smaller than the radial beam waist, of the order of 1 μm in diameter, the fluorescent species would be more uniformly illuminated as they pass through the probe volume. Then, to test the data analysis techniques described in Section 3.6, two species such as Biocytin and Streptavidin labeled with Qdot 585 could be used.

Finally, the use of microfluidic Lab-on-a-chip devices should also be investigated for drug-binding assays with flow in pharmaceutical drug discovery. The small sample volumes used with these devices would allow the cost of reagents to be kept low.

# References

# References

[1] Y. Ishii and T. Yanagida, "Single molecule detection in life science," *Single Mol.*, **1**, 5-16 (2000).

[2] N. L. Thompson, "Fluorescence correlation spectroscopy," in *Topics in Fluorescence Spectroscopy, Vol. 1: Techniques* J. R. Lakowicz, ed., (Plenum Press, New York 2001), pp. 337-378.

[3] M. Kinjo and R. Rigler, "Ultrasensitive hybridization analysis using fluorescence correlation spectroscopy," *Nuc. Acids Res.*, **23**, 1795-1799 (1995)

[4] X. Michalet, S. Weiss, and M. Jäger, "Single-molecule fluorescence studies of protein folding and conformational dynamics," *Chem. Rev.*, **106**, 1785-1813 (2006).

[5] T. Funatsu, Y. Harada, M. Tokunaga, K. Saito, and T. Yanagida, "Imaging of single fluorescent molecules and individual ATP turnovers by single myosin molecules in aqueous solution," *Nature*, **374**, 555-559 (1995).

[6] H. Noji, R. Yasuda, M. Yoshida, and K. Kinosita Jr., "Direct observation of the rotation of $F_1$-ATPase," *Nature*, **386**, 299-302 (1997).

[7] L.M. Davis, F.R. Fairfield, J.H. Hahn, C.A. Harger, J.H. Jett, R.A. Keller, L.A. Krakowski, B.A. Marrone, J.C. Martin, H.L. Nutter, R.L. Ratliff, E.B. Shera, D.J. Simpson, and S.A. Soper, "Rapid DNA sequencing based upon single molecule detection," *Genetic Analysis: Techniques and Applications*, **8**, 1-7 (1991).

[8] J. G. K. Williams, "Heterogeneous assay for pyrophosphate detection," *United States Patent #6,232,075* (2001).

[9] K. M. Swift and E. D. Matayoshi, "Applications of FCS to protein-ligand interactions: Comparison to fluorescence polarization," in *Fluorescence Correlation Spectroscopy: Theory and Applications*, R. Rigler and E. S. Elson, eds., (Springer-Verlag, Berlin, Germany, 2001), pp. 84-100.

[10] J. Mertz, C. Xu, and W. W. Webb," Single-molecule detection by two-photon-excited fluorescence," *Opt. Lett.*, **20**, 2532-2534 (1995).

[11] J. R. Lakowicz, **Principles of Fluorescence Spectroscopy**, **2nd Ed.** Kluwer Academic/Plenum Publishers, New York (1999).

[12] M. Mizuno and T. Tahara, "Picosecond time-resolved resonance Raman study of the solvated electron in water," *J. Phys. Chem. A*, **107**, 2411-2421 (2003).

[13] T. Hirschfeld, "Optical microscopic observation of single small molecules," *Appl. Opt.*, **15**, 2965-2966 (1976).

[14] N. J. Dovichi, J. C. Martin, J. H. Jett, M. Trkula, and R. A. Keller, "Laser-induced fluorescence of flowing samples as an approach to single molecule detection in liquids," *Anal. Chem.*, **56**, 348-354 (1984).

[15] D. C. Nquyen, R. A. Keller, and M. Trkula, "Ultrasensitive laser-induced fluorescence detection in hydrodynamically focused flows," *J. Opt. Soc. Am. B*, **4**, 138-143 (1987).

[16] E. B. Shera, N. K. Seitzinger, L. M. Davis, R. A. Keller, and S. A. Soper, "Detection of single fluorescent molecules," *Chem. Phys. Lett.*, **174**, 553-557 (1990).

[17] L.-Q., Li and L. M. Davis, "Single photon avalanche diode for single molecule detection," *Rev. Sci. Instrum.*, **64**, 1524-1529 (1993).

[18] A. Spinelli, L. M. Davis, and H. Dautet, "Actively quenched single-photon avalanche diode for high repetition rate time-gated photon counting," *Rev. Sci. Instrum.*, **67**, 55-61 (1996).

[19] Y. H. Lee, R. G. Maus, B. W. Smith, and J. D. Winefordner, " Laser-induced fluorescence detection of a single molecule in a capillary," *Anal. Chem.*, **66**, 4142-4149 (1994).

[20] L. Q. Li and L. M. Davis, "Rapid and efficient detection of single chromophore molecules in aqueous solution," *Appl. Opt.*, **34**, 3208-3217 (1995).

[21] J. C. Fister III, S. C. Jacobson, L. M. Davis, and J. M. Ramsey, "Counting single chromophore molecules for ultrasensitive analysis and separations on microchip devices," *Anal. Chem.*, **70**, 431-437 (1998).

[22] C. Zander, K. H. Drexhage, K. -T. Han, J. Wolfrum, and M. Sauer, "Single-molecule counting and identification in a microcapillary," *Chem. Phys. Lett.*, **286**, 457-465 (1998).

[23] W. Becker, H. Hickl, C. Zander, K. H. Drexhage, M. Sauer, S. Siebert, and J. Wolfrum, "Time-resolved detection and identification of single analyte molecules in microcapillaries by time-correlated single-photon counting (TCSPC)," *Rev. Sci. Instrum.*, **70**, 1835-1841 (1999).

[24] B. B. Haab and R. A. Mathies, "Single-molecule detection of DNA separations in microfabricated capillary electrophoresis chips employing focused molecular streams," *Anal. Chem.*, **71**, 5137-5145 (1999).

[25] J. J. Zheng and E. S. Yeung, "Counting single DNA molecules in a capillary with radial focusing," *Aust. J. Chem.*, **56**, 149-153 (2003).

[26] M. B. Wabuyele, S. M. Ford, J. Barrow, and S. A. Soper, "Single molecule detection of double-stranded DNA in poly(methylmethacrylate) and polycarbonate microfluidic devices," *Electrophoresis*, **22**, 3939-3948 (2001).

[27] A. Lundqvist, D. T. Chiu, and O. Orwar, "Electrophoretic separation and confocal laser-induced fluorescence detection at ultralow concentrations in constricted fused-silica capillaries," *Electrophoresis*, **24**, 1737-1744 (2003).

[28] S. M. Stavis, J. B. Edel, K. T. Samiee, and H. G. Craighead, "Single molecule studies of quantum dot conjugates in a submicrometer fluidic channel," *Lab on a Chip*, **5**, 337-343 (2005).

[29] J. M. Song, T. Inoue, H. Kawazumi, and T. Ogama, "Single molecule detection by laser two-photon excited fluorescence in a capillary flowing cell," *Anal. Sci.*, **14**, 913-916 (1998).

[30] A. Van Orden, H. Cai, P. M. Goodwin, and R. A. Keller, "Efficient detection of single DNA fragments in flowing sample streams by two photon fluorescence excitation," *Anal. Chem.*, **71**, 2108-2116 (1999).

[31] P. S. Dittrich and P. Schwille, "An integrated microfluidic system for reaction, high-sensitivity detection, and sorting of fluorescent cells and particles," *Anal Chem.*, **75**, 5767-5774 (2003).

[32] B. H. Kunst, A. Schots, and A. J. W. G. Visser, "Design of a confocal microfluidic particle sorter using fluorescent photon burst detection," *Rev. Sci. Instrum.* **75**, 2892-2898 (2004).

[33] P. S. Dittrich and A. Manz, "Single-molecule fluorescence detection in microfluidic channels-the Holy Grail in μTAS," *Ana. Bioanal. Chem.*, **382**, 1771-1782 (2005).

[34] J. Melin, H. Johansson, O. Soderberg, F. Nikolajeff, U. Landegren, M. Nilsson, and J. Jarvius, "Thermoplastic microfluidic platform for single-molecule detection, cell culture, and actuation," *Anal. Chem.*, **77**, 7122-7130 (2005).

[35] A. J. Skulan, L. M. Barrett, A. K. Singh, E. B. Cummings, and G. J. Flechtner, "Fabrication and analysis of spatially uniform field electrokinetic flow devices: theory and experiment," *Anal. Chem.*, **77**, 6790-6797 (2005).

[36] J. C. Roulet, R. Völkel, H. P. Herzig, E. Verpoorte, N. F. de Rooij, and R. Dändliker, "Fabrication of multilayer systems combining microfluidic and microoptical elements for fluorescence detection," *J. Microelctromech. Syst.*, **10**, 482-491 (2001).

[37] K. Dörre, J. Stephan, M. Lapczyna, M. Stuke, H. Dunkel, and M. Eigen, "Highly efficient single molecule detection in microstructures," *J. Biotech.*, **86**, 225-236 (2001).

[38] B. H. Kunst, A. Schots, and A. J. W. G. Visser, "Detection of flowing fluorescent particles in a microcapillary using fluorescence correlation spectroscopy," *Anal. Chem.* **74**, 5350-5357 (2002).

[39] J. P. Shelby and D. T. Chiu, "Mapping fast flows over micrometer-length scales using flow-tagging velocimetry and single-molecule detection," *Anal. Chem.*, **75**, 1387-1392 (2003).

[40] M. E. Johnson and J. P. Landers, "Fundamentals and practice for ultrasensitive laser-induced fluorescence detection in microanalytical systems," *Electrophoresis*, **25**, 3513-3527 (2004).

[41] L. Tao and R. T. Kennedy, "Laser-induced fluorescence detection in microcolumn separations," *Trends Anal. Chem.*, **17**, 484-491 (1998).

[42] D. A. Ball, "Single molecule imaging with a custom-built fluorescence microscope,**"** MS thesis**,** University of Tennessee, Knoxville (2002).

[43] L. M. Davis, W. C. Parker, D. A. Ball, J. G. K. Williams, G. R. Bashford, P. Sheaff, R. Eckles, D. T. Lamb, and L. R. Middendorf, "Imaging of single- chromophore molecules in aqueous solution near a fused-silica interface," in *Multiphoton Microscopy in the Biomedical Sciences*, A. Periasamy, P. T. C. So, eds, Proc. SPIE, **4262**, 301-311 (2001);

[44] L. M. Davis, W. C. Parker, D. A. Ball, J. G. K. Williams, G. Bashford, D. L. Grone, R. D. Eckles, and L. R. Middendorf, "Imaging single molecules in solution near a fused-silica interface," presented at the 45th Annual Meeting of the Biophysical Society, Boston, MA, 17-21 Feb. 2001.

[45] L. M. Davis, P. E. Williams, H. M. Cain, D. A. Ball, C. G. Parigger, E. D. Matayoshi, and K. M. Swift, "Comparison of fluorescence correlation spectroscopy and other single-molecule data analysis methods for assay of protein-ligand interactions," presented at the 46th Annual Meeting of the Biophysical Society, San Francisco, CA, 23-27 Feb. 2002.

[46] L. M. Davis, D. A. Ball, P. E. Williams, K.M. Swift, and E. D. Matayoshi, "Data reduction methods for application of FCS to high-throughput pharmaceutical drug

screening," presented at the 6th International Carl Zeiss Workshop on Fluorescence Correlation Spectroscopy & Related Methods, St. Louis, MO, 21-22 May 2002.

[47] L. M. Davis, D. A. Ball, P. E. Williams, K. M. Swift, and E. D. Matayoshi, "Fluorescence correlation spectroscopy data reduction and application to peptide binding studies with BCL-xL," presented at the 5th International Weber Symposium on Innovative Fluorescence Methodologies in Biochemistry and Medicine, Lihue, HI., 25-29 June 2002.

[48] L. M. Davis, D. A. Ball, P. E. Williams, E. D. Matayoshi, and K. M. Swift, "Dealing with reduced data acquisition times in fluorescence correlation spectroscopy for HTS applications," in *Microarrays and Combinatorial Technologies for Biomedical Applications*, D. V. Nicolau and R. Raghavachari, eds., Proc. SPIE **4966**, 117-128 (2003).

[49] L. M. Davis, D. A. Ball, P. E. Williams, K. M. Swift, and E. D. Matayoshi, "Comparison of various data analysis methods for 2-color high-throughput drug-binding measurements," presented at the PicoQuant 9th International Workshop on Single Molecule Detection and Ultra Sensitive Analysis in the Life Sciences, Berlin, Germany 24-26 Sept. 2003.

[50] L. M. Davis, G. Shen, and D. A. Ball, K. M. Swift, and E. D. Matayoshi, "Accounting for saturation and triplet effects in FCS measurements," presented at the 6th International Weber Symposium on Innovative Fluorescence Methodologies in Biochemistry and Medicine, Kauai, HI, 22-28 July 2005.

[51] A. Diaspro and C. J. R. Sheppard, "Two-photon excitation fluorescence microscopy," in *Confocal and Two-Photon Microscopy: Foundations, Applications, and Advances*, A. Diaspro, ed. (Wiley-Liss, New York, NY, 2002), pp. 39-73.

[52] W. Kaiser and C. G. B. Garrett, "Two-photon excitation in $CaF^2 : Eu^{2+}$," *Phys. Rev. Lett.*, **7**, 229-231 (1961).

[53] W. Denk, J. H. Strickler, and W. W. Webb, "Two-photon laser scanning fluorescence microscopy," *Science*, **248**, 73-76 (1990).

[54] W. Denk and K. Svoboda, "Photon upmanship: why multiphoton imaging is more than a gimmick," *Neuron*, **18**, 351-357 (1997).

[55] S. W. Hell, M. Booth, S. Wilms, C. M. Schnetter, A. K. Kirsch, D. J. Arndt-Jovin, and T. M. Jovin, "Two-photon near- and far-field fluorescence microscopy with continuous-wave excitation," *Opt. Lett.*, **23**, 1238-1240 (1998).

[56] P. Schwille, U. Haupts, S. Maiti, and W. W. Webb, "Molecular dynamics in living cells observed by FCS with one- and two- photon excitation," *Biophys. J.*, **77**, 2251-2265 (1999).

[57] R. M. Williams, D. W. Piston, and W. W. Webb, "Two-photon molecular excitation provides intrinsic 3-dimensional resolution for laser-based microscopy and microphotochemistry," *FASEB J.*, **8**, 804-813 (1994).

[58] L. M. Davis, G. Shen, and D. A. Ball, "Saturation effects in fluorescence correlation spectroscopy," in *Multiphoton Microscopy in the Biomedical Sciences V*, A. Periasamy, P. T. C. So, eds., Proc. SPIE **5700**, 128-137 (2005).

[59] S. R. Aragón and R. Pecora, "Fluorescence correlation spectroscopy as a probe of molecular dynamics," *J. Chem. Phys.*, **64**, 1791-1803 (1976).

[60] R. Rigler, J. Widengren, and U. Mets, "Interactions and kinetics of single molecules as observed by fluorescence correlation spectroscopy," in *Fluorescence Spectroscopy: New Methods and Applications*, Otto S. Wolfbeis, ed. (Springer-Verlag, Berlin, 1992),

pp. 13-24.

[61] J. Widengren, Ü. Mets, and R. Rigler, "Fluorescence correlation spectroscopy of triplet states in solution: a theoretical and experimental study,"*J. Phys. Chem.*, **99**, 13368-13379 (1995).

[62] L. M. Davis, P. E. Williams, D. A. Ball, E. D. Matayoshi, and K. M. Swift, "Data reduction methods for application of fluorescence correlation spectroscopy to pharmaceutical drug discovery," *Curr. Pharm. Biotech.* **4**, 451—462 (2003); **5**, 481—481 (2004).

[63] M. Zhao, L. Jin, B. Chen, Y. Ding, H. Ma, and D. Chen, "Afterpulsing and its correction in fluorescence correlation spectroscopy experiments," *Appl. Opt.*, **42**, 4031-4036 (2003).

[64] J. D. Müller, Y. Chen, and E. Gratton, "Photon counting histogram statistics," in *Fluorescence Correlation Spectroscopy: Theory and Applications*, R. Rigler and E. S. Elson, eds., (Springer-Verlag, Berlin, Germany, 2001), pp. 410-437.

[65] Y. Chen, J. D. Müller, P. T. C. So, and E. Gratton, "The photon counting histogram in fluorescence fluctuation spectroscopy," *Biophys. J.*, **77**, 553-567 (1999).

[66] J. D. Müller, Y. Chen, and E. Gratton, "Resolving heterogeneity on the single molecular level with the photon-counting histogram," *Biophys. J.*, **78**, 474-486 (2000).

[67] B. Huang, T. D. Perroud, R. N. Zare, "Photon counting histogram: One photon excitation," *ChemPhysChem.*, **5**, 1523-1531 (2004).

[68] P. Kask, K. Palo, D. Ullmann, and K. Gall, "Fluorescence-intensity distribution analysis and its application in biomolecular detection technology," *Proc. Natl. Acad. Sci. USA*, **96**, 13756-13761 (1999).

[69] P. Kask, K. Palo, N. Fay, L. Brand, U. Mets, D. Ullmann, J. Jungmann, J. Pschorr, and K. Gall, "Two-dimensional fluorescence intensity distribution analysis: Theory and applications," *Biophys. J.*, **78**, 1703-1713 (2000).

[70] T. A. Laurence, A. N. Kapanidis, X. Kong, D. S. Chemla, and S. Weiss, "Photon arrival-time interval distribution (PAID): A novel tool for analyzing molecular interactions," *J. Phys. Chem. B*, **108**, 3051-3067 (2004).

[71] L. M. Davis, G. Shen, and D. A. Ball, "Scanning confocal fluorescence spectroscopy for molecular brightness assays," presented at the 49th Annual Meeting of the Biophysical Society, Long Beach, CA, 12-16 Feb. 2005.

[72] U. Mets and R. Rigler, "Submillisecond detection of single rhodamine molecules in water," *J. Fluoresc.*, **4**, 259-264 (1994).

[73] H. Qian and E. L. Elson, "Analysis of confocal laser optics for 3-D fluorescence correlation spectroscopy," *Appl. Opt.*, **30**, 1185-1195 (1991).

[74] K. H. Lee, K. S. Jeon, D. A. Ball, G. Shen, and L. M. Davis, "Dynamic properties of photoluminescence from porous silicon," presented at the 96th Annual Meeting of the Korean Chemical Society, Yonsei University (Wonju Campus), 21-22 Oct. 2005.

[75] H. Bagçi, F. Kohen, U. Kusçuoglu, E. A. Bayer, and M. Wilchek, "Monoclonal anti-biotin antibodies simulate avidin in the recognition of biotin," *FEBS Letters*, **322**, 47-50 (1993).

[76] M. A. Holden, S. Kumar, E. T. Castellana, A. Beskok, and P. S. Cremer, "Generating fixed concentration arrays in a microfluidic device," *Sensors and Actuators B*, **92**, 199-207 (2003).

[77] S. Miyamoto and P. A. Kollman, "What determines the strength of noncovalent association of ligands to proteins in aqueous solution?" *Proc. Natl. Acad. Sci. USA*, **90**, 8402-8406 (1993).

[78] C. Xu, and W. W. Webb, "Measurement of two-photon excitation cross sections of molecular fluorophores with data from 690 to 1050 nm," *J. Opt. Soc. Am. B.*, **13**, 481-491 (1996).

[79] S. A. Rani, B. Pitts, and P. S. Stewart, "Rapid diffusion of fluorescent traces into *Staphylococcus epidermis* biofilms visualized by time lapse microscopy," *Antimicrob. Agents Chemother.*, **49**, 728-732 (2005).

[80] D. R. Larson, W. R. Zipfel, R. M. Williams, S. W. Clark, M. P. Bruchez, F. W. Wise, and W. W. Webb, "Water-soluble quantum dots for multiphoton fluorescence imaging in vivo," *Science*, **300**, 1434-1436 (2003).

# Appendices

# Appendix A

# Fluorescence and Competing Processes

LIF is the result of laser light used to repeatedly excite an organic dye molecule from its ground state to an excited singlet state. Once in this upper state, the molecule may return to the ground state by one of several mechanisms. Figure A.1 shows a Jablonski diagram for a typical organic dye molecule, which displays the possible transitions between the excited singlet state and the ground state.

One possibility is that the molecule undergoes an electronic dipole transition to the ground state with the emission of a fluorescence photon. The molecule may also return to the ground state by other, non-fluorescent means, which are discussed below. The fluorescence quantum yield, $\Phi_F$, and fluorescence lifetime, $\tau_F$, are defined in terms of the fluorescent decay rate, $K_F$, and non-fluorescent decay rates, $K_{NF}$,

$$\Phi_F = \frac{K_F}{K_F + K_{NF}}, \tag{A.1}$$

$$\tau_F = \left(K_F + K_{NF}\right)^{-1}. \tag{A.2}$$

The fluorescence lifetime is an average measure of the time between the absorption of a photon and emission of fluorescence, and is on the order of several nanoseconds for a typical organic dye.

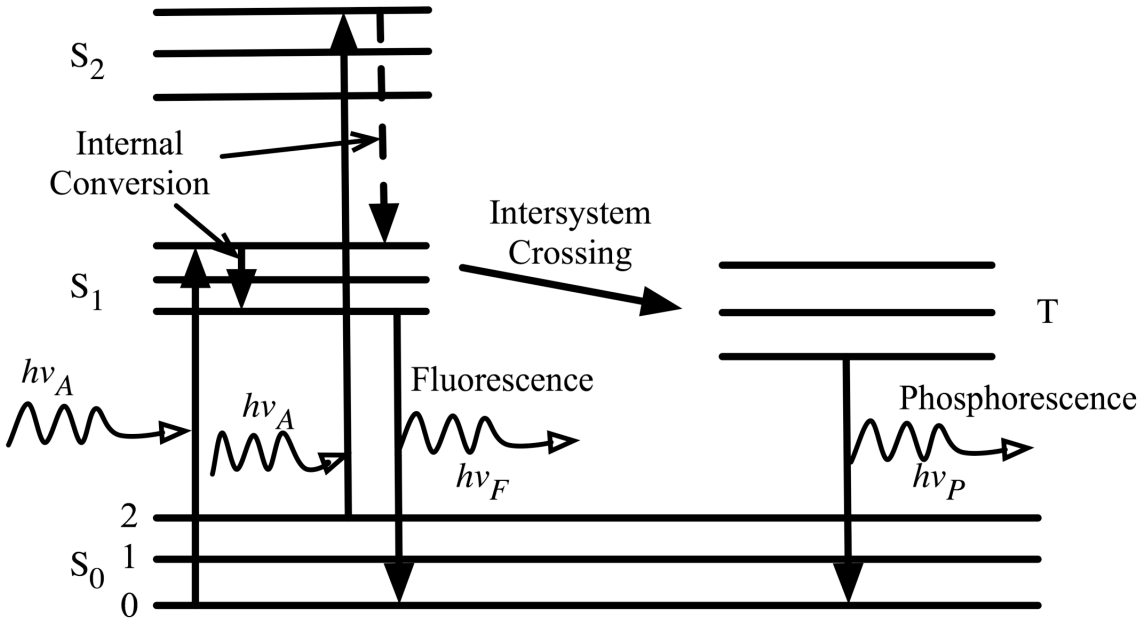


Figure A.1: Jablonski diagram for an organic dye molecule.

Fluorescence also exhibits an energy loss between excitation and emission, resulting in a shift in emission towards longer wavelengths [11]. This Stokes' shift is caused by the rapid decay (~1 ps) of the fluorophore to the lowest vibrational level of the first excited manifold.

As mentioned above an excited molecule can decay to the ground state by non-radiative means, resulting in lower fluorescence quantum yield and shorter lifetimes as shown in Eqns. 1.1 and 1.2. There is also a possibility that the molecule passes to an excited triplet state without emitting a photon. From the triplet state, the molecule can also decay with or without photon emission. This process takes place on a much longer timescale than fluorescence, and if a photon is emitted, it is known as phosphorescence. While in the more reactive excited state, the molecule may be chemically altered. This change in the dye results in its inability to produce further fluorescence, and is known as photobleaching.

# Appendix B

# Simplified Treatment of Two-Photon Excitation

TPE can be understood as the absorption of two photons simultaneously (within ~$10^{-16}$ s), which causes the molecule to be excited by means of a virtual intermediate state. For the OPE process, the energy of each photon must be equal to the energy difference of the ground state and first excited state, $\Delta E$, and is given by,

$$\Delta E = h\nu = \frac{hc}{\lambda}. \tag{B.1}$$

Here $h$ is Planck's constant, and $c$ the speed of light in vacuum. For the two-photon process the sum of the photon energies must be this same difference, and typically a single wavelength is used so that

$$\lambda_{2PE} = 2\lambda_{1PE}. \tag{B.2}$$

Due to different selection rules, the TPE absorption spectrum is not obtained by rescaling the wavelength in the OPE spectrum. However, in a simplified treatment, the TPE cross-section may be expressed as

$$\sigma_{2PE} = \sigma_{0K}\sigma_{K1}\tau_K, \tag{B.3}$$

where $\sigma_{0K}$ represents the one-photon absorption cross-section between the ground state and a virtual state $K$, $\sigma_{K1}$ is the absorption cross-section between the virtual state and the excited state, and $\tau_K$ is the lifetime of the virtual state. A level diagram for TPE is shown in Figure B.1. The unit of measure for the two-photon absorption cross-section is defined as the Göppert-Mayer (1 GM ≡ $10^{-50}$ $cm^4$ s). For typical values of $\sigma_{0K} = \sigma_{K1} \approx 10^{-16} - 10^{-17}$ $cm^2$ and $\tau_K \approx 10^{-16}$ s, the estimated absorption cross-section for TPE is approximately 10 GM.

After an estimate the two-photon absorption cross-section is achieved, it is necessary to determine the probability of two photons being in the volume occupied by the molecule at any given time. If we consider a cube with sides of length $a$, then the energy inside this box is related to the number of photons, $n$, and the laser wavelength, $\lambda$,

$$E_n = \frac{nhc}{\lambda}. \tag{B.4}$$

Then, because the area of one side of the box is $a^2$, and the time that a photon needs to cross the cube is $c/a$, the irradiance, $I$, is given by

$$I = \frac{E_n}{a^2 \cdot a/c} = \frac{nhc^2}{a^3 \lambda}. \tag{B.5}$$

If the cube is then made to enclose a single molecule, the volume $V = a^3$ would then be the volume of the molecule, i.e.

$$V = \frac{V_m}{N_A}, \tag{B.6}$$

with $V_m$ the molar volume, and $N_A$ Avogadro's number ($N_A = 6.022 \times 10^{23}$ $mol^{-1}$). The mean number of photons in this volume is then

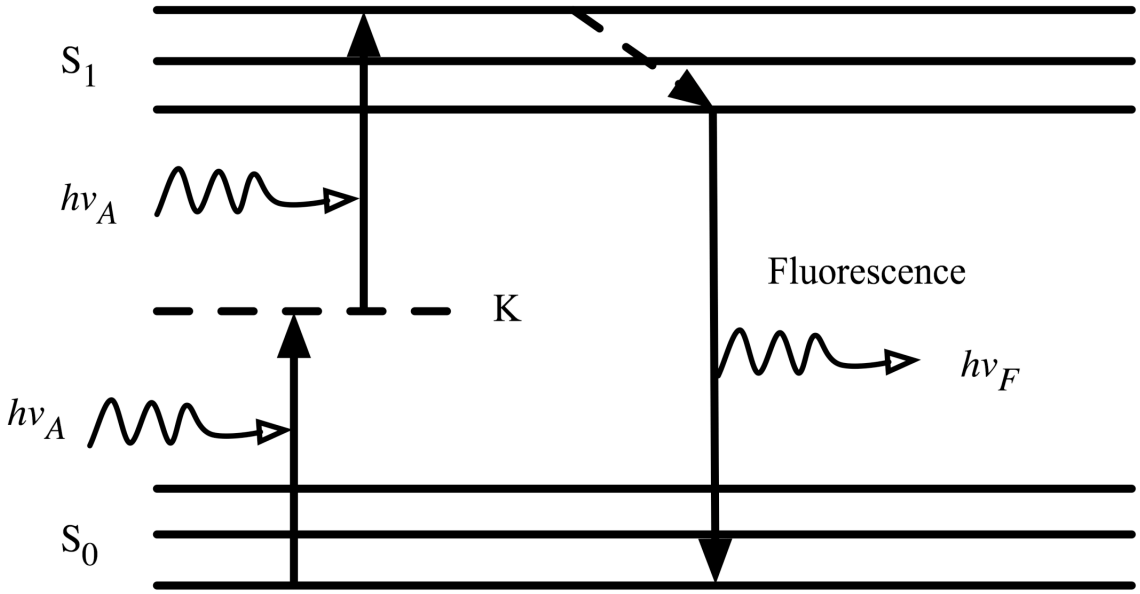


Figure B.1: Simplified level diagram illustrating TPE. The state K is virtual, and has a very short (~$10^{-16}$ s) lifetime.

$$n = \frac{IV_m \lambda}{N_A hc^2}. \tag{B.7}$$

The probability of *m* photons being in this volume element simultaneously, is then given by the Poisson distribution

$$P(m) = \frac{n^m}{m!} e^{-n}. \tag{B.8}$$

The exponential term in this expression can be approximated as unity. This is justified if we examine *n* for typical experimental parameters. If we consider 100 fs pulsed laser beam with an average power of 1 mW and a repetition rate of 76 MHz focused to a spot with a radius of 1 μm, then the peak irradiance is ~4 GW/cm$^2$. With $\lambda$ = 800 nm and a fluorophore with a molar volume of ~100 cm$^3$/mol, then $n \approx 8.8 \times 10^{-5}$. Therefore, with *m* = 2, the probability is given by

$$P(2) = \frac{1}{2} n^2 = \frac{1}{2} \left( \frac{IV_m \lambda}{N_A hc^2} \right)^2, \tag{B.9}$$

and with the above conditions, the probability of two photons being within the volume of a single fluorophore is ~$4 \times 10^{-9}$. It is important to note here that this probability is proportional to the square of the laser irradiance compared to the probability for one-photon absorption, which is proportional to the irradiance. This fact leads to some of the advantages, such as the inherent optical sectioning that are discussed in Section 2.1.

Next, with the laser focused by an objective lens that has numerical aperture *NA* the fluorescence excitation rate, $k_F(t)$, is considered, which is proportional to the absorption cross-section, $\sigma_2$, and the time-varying laser irradiance, $I(t)$

$$k_F(t) \approx \sigma_{2PE}[I(t)]^2 = \sigma_{2PE}[P(t)]^2\left[\frac{(NA)^2}{2\hbar c\lambda}\right]^2, \tag{B.10}$$

where $P(t)$ is the laser power, and the term $\hbar = h/2\pi$ has been introduced.

For cw laser illumination, $P(t) = P_{avg}$, and the time-averaged fluorescence excitation in a random interval, $T$, is

$$\left\langle k_{F,cw}(t)\right\rangle \equiv \frac{1}{T}\int_0^T I_F(t)dt = \sigma_{2PE}P_{avg}^2\left[\frac{(NA)^2}{2\hbar c\lambda}\right]^2. \tag{B.11}$$

With pulsed excitation of pulse-width $\tau_p$, and repetition rate $f_p$, the time-varying power can be approximated as

$$P(t) = \begin{cases} \dfrac{P_{avg}}{\tau_p f_p} & \text{for} \quad 0 < t < \tau_p, \\ 0 & \text{for} \quad \tau_p < t < \dfrac{1}{f_p}, \end{cases} \tag{B.12}$$

and the time-averaged fluorescence excitation becomes

$$\left\langle k_{F,pulsed}(t)\right\rangle = \sigma_{2PE}\frac{P_{avg}^2}{\tau_p f_p^2}\left[\frac{(NA)^2}{2\hbar c\lambda}\right]^2. \tag{B.13}$$

From here it is evident that reduction of the pulse width and repetition rate will optimize the fluorescence intensity, and also that cw and pulsed laser excitation will have similar efficiencies if the cw laser power is higher by a factor of $(\tau_p f_p^2)^{-1/2}$.

# Vita

David A. Ball was born in Cortland, New York on May 1, 1978. He was raised in Cortland until the sixth grade, when his family moved to nearby Homer. He was always curious about how things worked, and was constantly taking things apart, and *trying* to put them back together. It wasn't until his senior year at Homer High School, however, that he was shown the fascinating world of physics by Mr. Hal Fuller. David then attended The University at Albany (NY), graduating cum laude in 2000 with a bachelor's degree in Physics. While in Albany, he worked on such projects as the restoration of the university's 16" Cassegrain telescope. In the fall of 2000, David accepted a Graduate Research Assistantship at The University of Tennessee Space Institute, where he earned a Master of Science degree in physics in July 2002, and in 2006 received a Ph. D. in physics.